A layered approach to mangrove-induced wave attenuation modelling

A 2DV OpenFOAM application

MSc Thesis

Jan van der Wijk

Delft University of Technology

TU Delft

Delft University of Technology

Master Thesis

CIEM0500

A layered approach to mangrove-induced wave attenuation modelling

Author:

Jan van der Wijk (4717228)

Chairman:	J.A. Álvarez Antolínez
Supervisor:	J.O. Colomes Gene
Supervisors Haskoning:	U.S.N. Best C. R. Veldman
University of Cantabria:	M. Maza

Haskoning
Enhancing Society Together

TU Delft

Abstract

Mangroves play a vital role in coastal ecosystems by dissipating wave energy, protecting against erosion and supporting biodiversity. Despite their importance, quantification of their attenuation capabilities remains challenging. This study explores the potential of a two-dimensional (2DV) OpenFOAM model to simulate wave attenuation through mangrove forests using a layered approach to capture the vertical variability in mangrove frontal area.

The model is first validated against flume measurements under a range of different hydrodynamic conditions to assess its capability in a controlled, well-measured environment. The goal is that by applying the Reynolds Averaged Navier Stokes equations and a layered approach, a more realistic bulk drag coefficient can be calibrated for different hydrodynamic conditions. One of the objectives is to explore whether this approach can yield a stronger correlation between the bulk drag coefficient ($\tilde{C}_\mathrm{d}$) and the Keulegan-Carpenter (KC) number.

Then, the model is applied to a real-world case study for the Mandai mangrove forest on the northwest coast of Singapore. his application demonstrates the model's ability to simulate complex coastal environments, including variable bathymetry, forest extent, and wave conditions. A sensitivity analysis is also conducted to evaluate the effect of different parameters on the modelled wave attenuation

Results confirm the model's capability to accurately represent the vertical variations in vegetation structure and their influence on wave attenuation. It showed great agreement with the measured wave attenuation of the flume after calibration. Despite its expected improvement on the $\tilde{C}_\mathrm{d}$-KC relation, it did not succeed in this, but it does reveal the impact of depth-variable drag forces and their effect on the velocity profile and wave attenuation. Furthermore, the case study showed its applicability to real-world coasts. Despite numerical dissipation standing in the way of any quantitative analysis, the runs in combination with the sensitivity analysis provided valuable insights into the model's behaviour and wave attenuation predictions.

Contents

Nomenclature

αh	Vegetation height [m]
β	Wave attenuation coefficient [1/m]
γ	Peak enhancement factor in the JONSWAP spectrum [–]
ν	Kinematic viscosity of water [m^2/s]
ρ	Water density [kg/m³]
τ_b	Bed shear stress [N/m²]
$\tilde{\beta}$	Analytically derived wave attenuation coefficient [1/m]
$\tilde{C}_\mathsf{d}$	Bulk drag coefficient [–]
ε_v	Energy dissipation per unit area [W/m²]
b_v	Frontal plant area per unit height [m²/m]
C_D	Drag coefficient [–]
c_g	Group velocity [m/s]
C_M	Inertia coefficient [–]
DBH	Diameter at Breast Height, a measure of tree trunk size [cm]
dx	Horizontal grid cell size [cm]
dz	Vertical grid cell size [cm]
E	Wave energy [J/m²]
F_D	Drag component of force [N/m³]
F_M	Inertia component of force [N/m³]
f_w	Bed friction factor [–]
F_x	Drag force in x-direction [N/m³]
g	Gravitational acceleration [m/s²]
H	Wave height [m]
h	Water depth [m]
H_0	Initial wave height [m]
H_i	Incident wave height [m]
H_s	Significant wave height [m]
$H_{\mathsf{rms},0}$	Root-mean-square wave height at the start of the mangrove zone [m]
$H_{\mathsf{rms},i}$	Root-mean-square wave height [m]
H_{m0}	zero order moment wave height [m]
k	Wave number [rad/m]
k_p	Peak wave number [rad/m]
l	Characteristic length scale [m]

N	Tree density [trees/m²]
T	Wave period [s]
T_p	Peak wave period [s]
u	Flow velocity in x-direction [m/s]
u_b	Peak near-bed orbital velocity [m/s]
1D	One-Dimensional
2DV	Two-Dimensional Vertical
3D	Three-Dimensional
CFD	Computational Fluid Dynamics
HC	Hydrodynamic Condition - prefix for the different flume simulations (1-7)
OpenFOAM	Open Field Operation and Manipulation – an open-source CFD toolbox
RANS	Reynolds-Averaged Navier-Stokes
SHD	Singapore Height Datum, horizontal reference level, mean water height
SLR	Sea Level Rise [m]
SWAN	Simulating WAves Nearshore – a spectral wave model
URANS	Unsteady Reynolds-Averaged Navier-Stokes
VOF	Volume of Fluid

1 Introduction

In the last decades, the concept of Building with Nature has gained significant traction as a sustainable approach to address coastal challenges by integrating ecological and engineering principles (Seddon et al., 2020). Coastal ecosystems such as salt marshes, dunes, and mangrove forests play a crucial role in mitigating erosion and reducing wave energy. By doing so, they lower flood risks and enhance shoreline stability (Jordan & Fröhle, 2022). However, a key challenge lies in quantifying the effects of Building with Nature on coastal dynamics to ensure accurate and efficient application. By improving predictive capabilities, particularly with respect to wave attenuation, designs can be more effective, often lowering project costs and shifting preference from traditional hard infrastructure to more nature-friendly solutions, which ultimately enhances biodiversity and reduces expenses (van Zelst et al., 2021).

Mangrove forests are especially known for their substantial capacity for wave attenuation, displayed in Figure 1.1. These salt-tolerant species thrive in tropical and subtropical coastal zones, often in intertidal regions where they are periodically submerged (Loon et al., 2016). Mangroves form dense root and canopy structures that dissipate wave energy, thereby decreasing flooding risks. Besides wave attenuation, mangroves provide many other critical ecosystem services (Getzner & Islam, 2020).

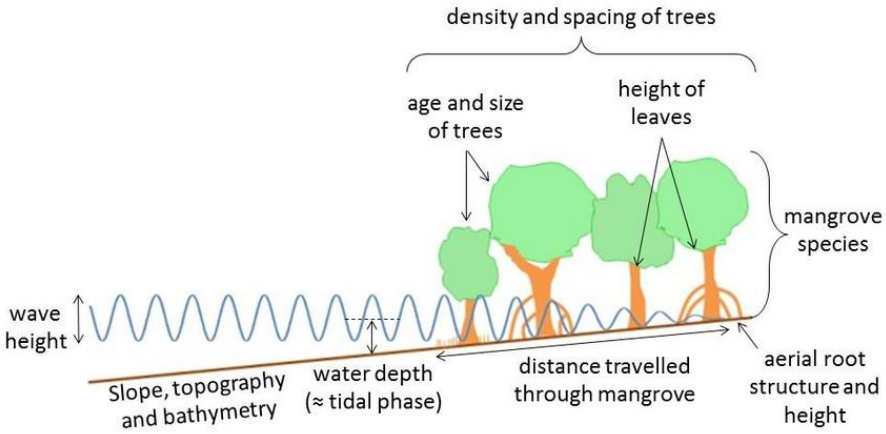

Figure 1.1: Wave attenuation due to mangroves schematised (McIvor et al., 2012)

The north-west coast of Singapore provides a compelling case study for the role of mangroves in coastal protection. Located in this region, the Mandai mangrove forest supports a diverse range of bird, fish, and plant species. The current levee design does not account for any mangrove-induced wave attenuation, resulting in higher levees. Although wave heights are relatively low, even modest reductions in wave height through vegetation-induced attenuation could lead to significant cost savings in levee design and construction.

Various approaches exist to assess the wave attenuation capacity of mangroves. Field studies can provide accurate information on local attenuation using sensors in the study area. The downside is that they often capture only mild conditions and are unreliable for extrapolating to more energetic, governing conditions. Experimental studies can also be used to provide insight into wave attenuation by mangroves. Flumes with controlled wave heights and water levels are used to understand the behaviour of mangroves under extreme conditions. However, due to the large size of mangrove forests, these

physical experiments have to be performed on a smaller scale, introducing scale effects that influence the accuracy of real-world predictions (Kalloe et al., 2024).

Numerical modelling offers a flexible and scalable alternative, enabling the simulation of wave-vegetation interactions across a wide range of conditions. Several different numerical models have been made to simulate the effects of mangroves on wave attenuation. These models range from simple 1D, mathematical models using the shallow water equations (Hoque et al., 2023) to full 3-dimensional Reynolds-Averaged Navier-Stokes (RANS) models (Wang et al., 2020). While more complex models can give very accurate results, there remains much uncertainty in the parametrisation of mangrove dimensions and behaviour under hydraulic loading.

To date, little research has been done into the capabilities of two-dimensional vertical (2DV) hydraulic models to simulate wave damping by mangroves. Since the properties of mangroves differ greatly over their height, the inclusion of these properties could provide added benefits and accuracy over 1-line models. Mangroves can generally be divided into three parts: roots, trunk and canopy. The lower parts of mangroves, at the roots, generally have the greatest energy-reducing properties due to the intricate structure and high density (Quartel et al., 2007). As the water level rises towards the trunks, the influence of these roots decreases, and the overall attenuating capabilities of the trees reduce. That is, until the water level reaches even further to the canopies. There, the dense and relatively rigid leaves, although much more flexible than the roots and trunk, provide great drag forces against the hydrodynamics, increasing attenuation (Zhang et al., 2023). The intricacies that these variations in mangrove properties over the height produce may yield more accurate model outcomes.

This study employs OpenFOAM, an open-source Computational Fluid Dynamics (CFD) toolbox, to develop a 2DV RANS-based model of wave propagation through mangrove vegetation. It uses the Reynolds-Averaged Navier-Stokes (RANS) equations to simulate complex flow.

By incorporating these height-varying changes in frontal area in a 2DV RANS model, the bulk drag coefficient $\tilde{C}_\mathrm{d}$ could be determined more accurately. Generally, this value is determined analytically by a formulation based on linear wave theory. The relation to non-dimensional hydraulic parameters such as the Reynolds (Re) and Keulegan-Carpenter (KC) number of the $\tilde{C}_\mathrm{d}$ values obtained in this manner has a great range of uncertainty. The capabilities of OpenFOAM to accurately model wave characteristics combined with varying drag forces over the height could result in more accurate relations between $\tilde{C}_\mathrm{d}$ and Re or KC. This can give more accurate predictions for other hydrodynamic conditions and decrease the uncertainty of wave attenuation predictions for mangroves.

Using local data on hydrodynamics, bathymetry and mangrove characteristics, a site-specific model of the Mandai mangrove forest in Singapore can be developed. This model enables a detailed investigation into the role of mangroves in local wave attenuation. By conducting a sensitivity analysis, where individual input parameters are varied in isolation, the model's response to key variables can be assessed, offering deeper insight into both the physical processes and the model's behaviour.

The objective of this study is to evaluate the modelling capabilities of a 2DV OpenFOAM model in simulating the attenuation capacity of mangroves, focusing both on replicating a flume experiment and a real-world coast. The research question is as follows.

To what extent can a 2DV OpenFOAM accurately represent wave attenuation due to mangrove forests for flume tests and real coasts?

To answer this question, three sub-questions must be answered

1. How can OpenFOAM be used to more accurately capture the frontal area variations over the height for mangroves in wave modelling?
2. What benefit can OpenFOAM provide in decreasing the uncertainty of the relation between the bulk drag coefficient and the Keulegan-Carpenter number?
3. To what extent can an OpenFOAM model accurately predict the wave attenuation for the North-West coast of Singapore?

To answer these questions, the report is outlined along the following structure. First, the State-of-the-Art chapter provides an overview of existing research and findings relevant to wave attenuation and

mangrove modelling. This is followed by an introduction to the flume experiment and case study, which describes both the flume experiment, on which research question two is focused, as well as the site for research question 3. The methodology chapter then outlines the model framework and model settings used for the study. Subsequently, the results section presents the key findings from the study, which are further analysed and interpreted in the discussion chapter. The report concludes with a summary of the main insights in the conclusion, followed by recommendations for future work.

2
State-of-the-art

This chapter provides a comprehensive overview of the current understanding and approaches related to mangrove-induced wave attenuation. It starts with an introduction to mangroves and their advantages. The chapter then delves into various modelling approaches and their underlying formulations. Subsequently, key considerations on different parameters and their influence on attenuation modelling for mangroves are discussed. A description of OpenFOAM and its functioning is then given, followed by a review of models and measurements similar to this study to act as a reference.

2.1. Mangroves

Mangroves are a unique group of intertidal plants uniquely adapted to surviving the saline, wave-attacked environments found along coasts and rivers. They play a key role along the coasts, aiding in biodiversity, food provision for fisheries and coastal protection amongst others. This section presents the most important information about mangroves, offering a broad overview as well as more specific insights relevant to this study..

2.1.1. Wave attenuation by mangroves

Mangroves play a crucial role in dissipating wave energy. Their dense root system, trunk and canopy provide a natural barrier, increasing flow resistance and turbulence, resulting in energy losses. Numerous field and flume studies have shown that mangrove forests can provide significant wave attenuation for coasts. The amount of attenuation depends on a large number of factors such as hydrodynamic conditions, tree density and tree characteristics (Brinkman, 2006).

2.1.2. Mangrove zonation

The most important factor for the zonation of mangroves is the inundation time. This is the duration of the soil of the mangroves being submerged. The inundation time that the trees can tolerate greatly depends on the species, with Avicennia being the most tolerant (Loon et al., 2016). This can also be seen in Figure 2.1 where Avicennia are at the outer edge, often followed by Rhizophora.

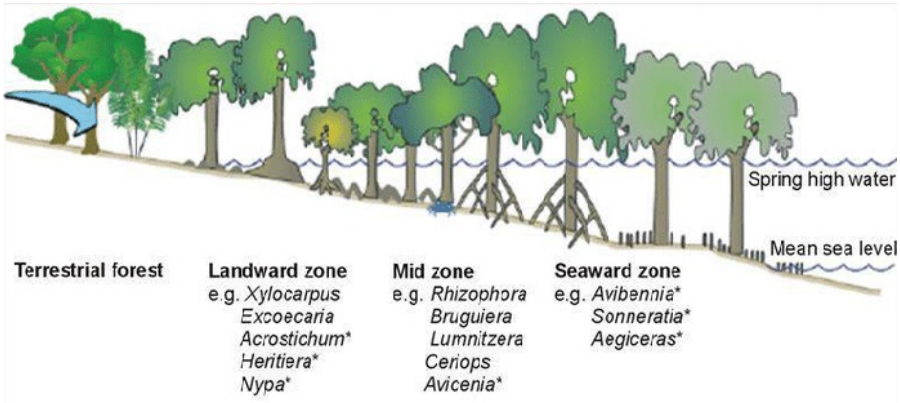

Figure 2.1: Mangrove zonation showing different zones and their occurring species (Tusinski & Verhagen, 2014)

2.1.3. Ecosystem services

Mangroves play a vital role in coastal ecosystems by serving as essential habitats for a diverse range of species. Their dense canopies provide critical nesting and roosting areas for various bird species, while the intricate root structures give shelter to many fish and shellfish species (Nagelkerken et al., 2008). These habitats in turn result in a higher productivity of the coastal ecosystem, providing essential food sources for the local population (Carrasquilla-Henao & Juanes, 2017). In addition to their ecological value, they are also significant factors in combating climate change. Due to their high rate of production as well as decomposition rate, they provide good carbon sequestration with rates 4-5 times that of boreal forests (Choudhary et al., 2024).

2.1.4. Mangrove decline

Despite the benefits they provide, many mangrove forests have disappeared over the past decades, with only 50% of the original mangrove forests remaining today (Feller et al., 2010). The leading cause of this loss is due to onshore aquaculture and agriculture (D. Friess et al., 2019). The mangrove forests were destroyed in large numbers to make way for these areas for food production. More recently, a shift has been happening away from this deforestation as recognition of the importance of mangrove ecosystem services has been growing.

2.1.5. Mangroves in Singapore

Similar to many other coastal regions worldwide, Singapore's mangrove forests have undergone significant decline due to urban expansion and land use changes. The estimated mangrove area of 75 km^2 at the start of the 19th century had significantly declined due to conversion to prawn ponds, land reclamation and use for firewood (Koon et al., 2010). In 1993, mangrove cover had dropped to just 4.9 km^2 (Hilton & Manning, 1995). Since then, the area has increased slightly, being back to 9.6 km^2 by 2016, but it remains a fraction of the original mangrove extent (D. A. Friess et al., 2016). Although mangroves occupy only 1% of Singapore's land area, the country is home to a remarkable diversity of mangrove species, with 30 distinct species recorded, thus playing a pivotal part in the coastal ecosystem (Spalding et al., 2010).

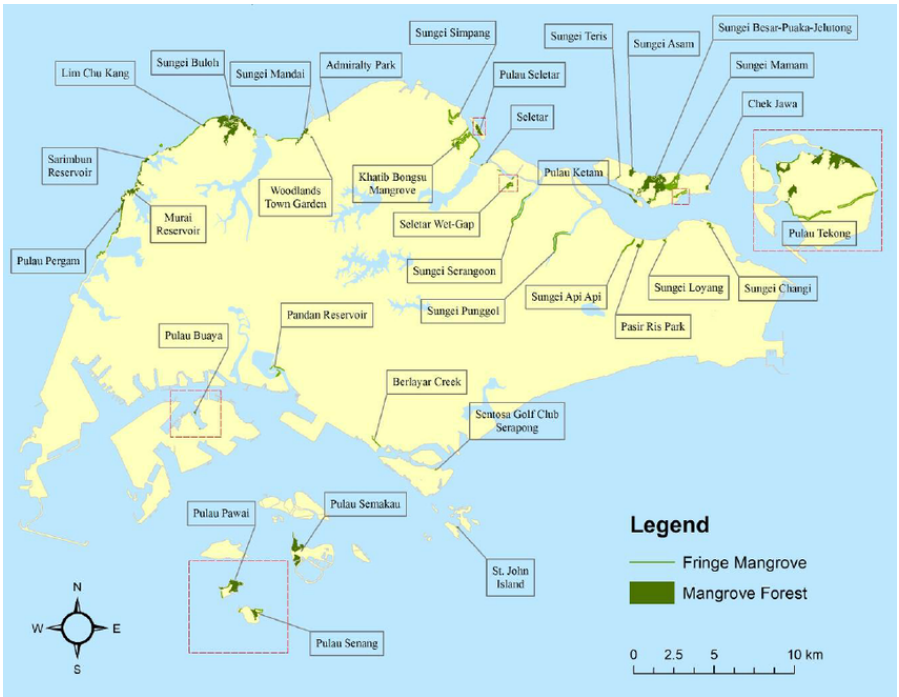

Figure 2.2: Mangrove extend in Singapore (Koon et al., 2010)

2.2. Modelling approaches for mangroves

Incorporating mangroves into a hydrodynamic model requires a parametrisation of these mangrove characteristics to be used as an energy sink term in the physical equations. This parametrisation has generally been carried out either as an increase in bed friction or as an additional friction term. In the subsections below, both approaches will be discussed. Since the drag force approach is used in this study, its explanation is more elaborate.

2.2.1. Bed friction approach

In the bed friction approach, the influence of mangroves on wave dynamics is represented as an enhanced bed shear stress (Quartel et al., 2007). This is expressed in Equation (2.1).

$$\tau_b = \frac{1}{4}\rho f_w U^2 \tag{2.1}$$

where τ_b is the bed shear stress induced by waves(N/m^2), ρ is the water density (1000 kg/m^3),f_w is the bed friction factor (-) including the effect of mangroves, u_b is the peak near-bed orbital velocity (m/s).

This method effectively increases bottom friction to simulate the presence of mangroves, without explicitly accounting for their structural characteristics. Since both share a quadratic relation to the flow velocities, it can give accurate results, but it is not a valid representation, especially with varying vegetation properties. A growing consensus is that the drag force approach offers a more realistic representation (Baron-Hyppolite et al., 2019; Smith et al., 2016).

2.2.2. Drag force approach

This approach schematises the mangroves as cylindrical structures subject to hydrodynamic forces. The Morison equation for a fixed body in an oscillatory flow is used to calculate this force and consequent energy losses (Morison et al., 1950). The result is the following formulation of the drag force of Equation (2.2).

$$F_x = \frac{1}{2}\rho \tilde{C}_\mathrm{D} b_v N u|u| \tag{2.2}$$

where $\tilde{C}_\mathrm{D}$ is the bulk drag coefficient (-), b_v is the frontal plant area per unit height (m^2/m) and N is the tree density (trees/m).

This section provides a detailed examination of the governing equation, highlighting its significance and practical application. The derivation process is first outlined to establish a clear theoretical foundation. Subsequently, the parameters b_v and N, which represent vegetation characteristics, are discussed along with different parameterisation techniques. The section then focuses on the bulk drag coefficient, beginning with a conceptual explanation of its physical meaning, followed by a discussion on how it can be determined analytically.

Drag force formulation

Following the drag force approach and schematising mangroves as one or multiple cylinders, the following section will lay out the approach to arriving at the drag force formulation. These formulations are based on the findings by Dalrymple et al. (1984), expanded on by F. J. Mendez and Losada (2004), and are based on linear wave theory.
From the conservation of energy equation, the energy dissipation can be determined by Equation (2.3).

$$\frac{\partial E c_g}{\partial x} = -\varepsilon_v \tag{2.3}$$

Where E is the wave energy, c_g is the group velocity, and ϵ_v is the energy dissipation per horizontal area. Wave energy is given by Equation (2.4).

$$E = 1/8\rho g H^2 \tag{2.4}$$

ρ is the density of the water, g is the gravitational acceleration and H is the wave height. Dalrymple et al. (1984) found the formula for energy as Equation (2.5).

$$\varepsilon_v = \overline{\int_{-h}^{-h+\alpha h} F_x u \, dz} \tag{2.5}$$

here, h is the water height, αh is the vegetation height, F_x the horizontal drag force in x-direction and u the velocity in x direction. The vertical drag forces are considered negligible in comparison to the horizontal drag forces and are excluded. F_x is then obtained by using the Morison equation, shown in Equation (2.6), which includes both drag and inertia components (Morison et al., 1950).

$$F_x = F_D + F_M = \frac{1}{2}\rho C_D b_v N u|u| + \frac{\pi}{4}\rho C_M b_v^2 N \frac{\partial u}{\partial t} \tag{2.6}$$

Where F_D is the drag force, F_M is the inertia force, C_d is the drag coefficient and C_M is the inertia coefficient.

Dalrymple et al. (1984) assumes the drag force to be the governing force and inertia to be insignificant, resulting in Equation (2.7).

$$F_x = \frac{1}{2}\rho C_D b_v N u|u| \tag{2.7}$$

Mangrove parametrisation

To define the inputs for the characteristics of the frontal area and tree density, mangroves are parametrised. For this approach, the frontal areas of mangroves are idealised as uniform cylinders, where the cylinder diameter is selected such that the average inundated frontal area matches that of the actual mangrove structure being represented.

Figure 2.3: Rhizophora Mucronata with its characteristic, intricate root system. Taken on the coast of Mauritius (Conservation, 2020)

Mangrove species, particularly Rhizophora (Figure 2.3), exhibit varying characteristics over their height. The roots are dense and intricate, having a large frontal area. The trunk is comparatively smaller, and the canopy is much wider again, having a larger frontal area. Models such as those made by (Q. Chen et al., 2021; Suzuki et al., 2012) aim to capture these variations and introduce multi-layered representations, each assigned a specific frontal area value b_v as illustrated by Figure 2.4. This parametrisation still models mangroves as uniform cylinders, but their width varies per water level, based on the average of the inundated frontal area.

No depth-resolving models including the height-varying characteristics of mangroves using this approach are currently known to exist. This presents an opportunity for a more realistic model with higher drag forces near the roots at the bottom, and lower forces higher up on the trunk. Discrete layers can be made, each replicating the average frontal area of that height range, resulting in different drag forces per layer.

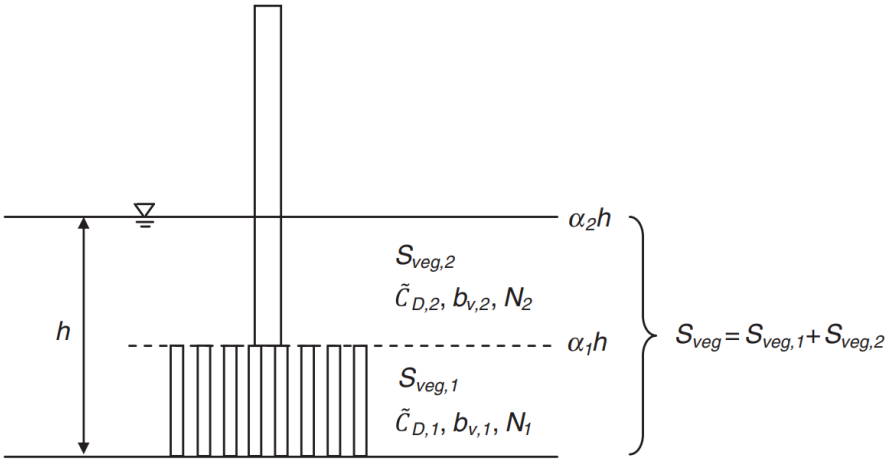

Figure 2.4: Layer schematisation made by Suzuki et al. (2012)

Bulk drag coefficient

A drag coefficient is a dimensionless number used for the quantification of the drag forces of specific shapes. The analytical solution of the drag force calculation, as done in Section 2.2.2, is made using the drag force coefficient C_d. For cylinders, as assumed in the approach, this factor is well known, as shown in Figure 2.5 with its dependency on the Reynolds number Re. Since the flow through mangroves is more complex, this formulation with C_d does not result in accurate solutions. To encompass other effects such as inertia and non-rigidity, the bulk drag coefficient, $\tilde{C}_\mathrm{d}$ is used.

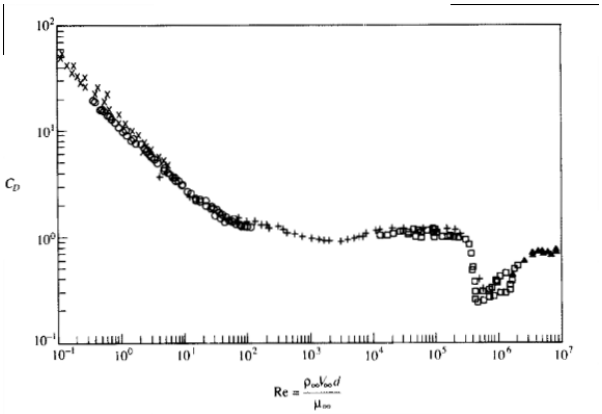

Figure 2.5: Drag force coefficient of a cylinder correlation with the Reynolds number (M. A. Mendez et al., 2017)

In mangrove modelling, $\tilde{C}_\mathrm{d}$ is used differently depending on the goal of the model. In predictive simulations without wave measurements, $\tilde{C}_\mathrm{d}$ values are often set at 1. This gives a conservative estimate

of the wave attenuation, since $\tilde{C}_\mathsf{d}$ generally range above 1 (Lopez-Arias et al., 2024). When measurements are available and the wave attenuation is known, $\tilde{C}_\mathsf{d}$ can be calibrated iteratively to match observed attenuation or be derived analytically from the wave attenuation, as described in the following section.

Analytical formulation of the drag force coefficient

To determine this drag force coefficient, an analytical formulation is used. This formulation is derived from measurements of the wave attenuation, which can be described by the wave attenuation parameter β. It encompasses the decrease in wave height over the length of the flume due to mangroves and has been analytically formulated for regular waves as Equation (2.8).

$$H = \frac{H_0}{1 + \tilde{\beta} x} \tag{2.8}$$

where H_0 is the initial wave height, x is the distance along the flume, and H is the wave height at that location.

This can be combined with the formulation of energy damping as described by Dalrymple et al. (1984), resulting in Equation (2.9).

$$\varepsilon_v = \frac{2}{3\pi} \rho C_D b_v N \left(\frac{kg}{2\sigma}\right)^3 \frac{\sinh^3 kh + 3\sinh kh}{3k\cosh^3 kh} H^3 \tag{2.9}$$

Where k is the wave number and σ is the wave angular frequency.

By combining Equation (2.8) and Equation (2.9), an analytical expression for the drag coefficient $\tilde{C}_D$ for regular waves is obtained, as shown in Equation (2.10):

$$\tilde{C}_\mathsf{D} = \frac{9\pi}{4NdH_i k} \frac{(\sinh 2kh + 2kh)\sinh kh}{\sinh^3 kl + 3\sinh kl} \beta \tag{2.10}$$

F. J. Mendez and Losada (2004) extended this formulation to obtain the formulation for irregular waves, resulting in Equation (2.11):

$$\tilde{C}_\mathsf{D} = \frac{3\sqrt{\pi}}{NdH_{\mathsf{rms},i} k_p} \frac{(\sinh 2k_p h + 2k_p h)\sinh k_p h}{\sinh^3 k_p l + 3\sinh k_p l} \beta \tag{2.11}$$

The values of $\tilde{C}_\mathsf{D}$ obtained from this formulation vary depending on mangrove characteristics and hydrodynamic conditions.

2.3. Key considerations

For the modelling of mangroves, some key considerations need to be taken into account. This section will describe the most important considerations attained from previous modelling and flume studies.

2.3.1. Relation with the Reynolds and Keulegan-Carpenter number

Similar to the drag of a cylinder, the bulk drag coefficient has also been shown to be correlated with hydraulic non-dimensional parameters such as the Reynolds number (Re), and the Keulegan-Carpenter number (KC) (Cao et al., 2016; Lopez-Arias et al., 2024; Ozeren et al., 2014; Zhang et al., 2023).

KC and Re are two important non-dimensional hydraulic parameters often used in wave attenuation by vegetation. These parameters give an insight into the type of flow conditions. The Reynolds number is determined by Equation (2.12).

$$Re = \frac{uL}{\nu} \tag{2.12}$$

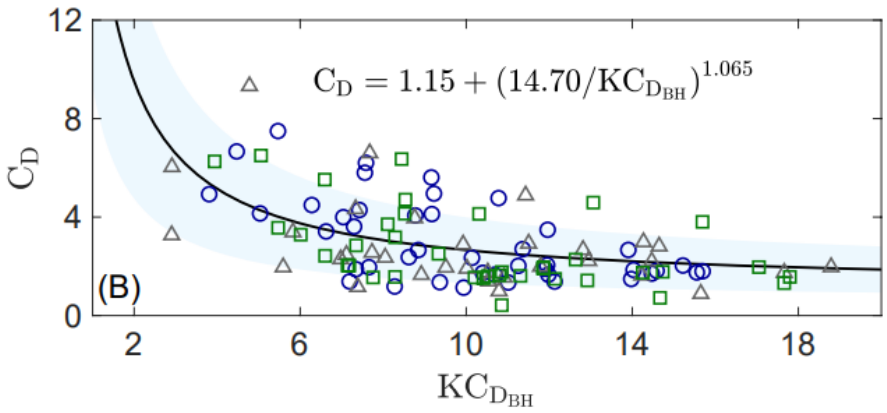

Figure 2.6: correlation between C_D and KC number as found by Chang et al. (2022)

Where u is the flow speed, L is the characteristic length and ν is the kinematic viscosity of water ($10^6 m^2/s$). The Reynolds number describes the ratio between inertial and viscous forces. It is used to determine the flow regime and is essential in calculations for energy losses from structures, for example.

The Keulegan-Carpenter number is given by Equation (2.13). It is used to describe the relative influence of drag forces over inertia, where KC values are larger for more drag-dominated wave climates.

$$KC = \frac{uT}{L} \tag{2.13}$$

The Bulk drag coefficient has been correlated with both KC and Re in many studies. There is still debate on which gives the most accurate results (H. Chen et al., 2018; Kelty et al., 2022; Lopez-Arias et al., 2024). Different studies also report varying functions on the correlation between $\tilde{C}_d$ and either KC or Re as shown in Table 2.1. These generally also have a big spread with R^2 values being around 0.6.

Table 2.1: Summary of drag coefficient formulas for various mangrove flume experiments adapted from Zhang et al. (2023).

Source	Scale	Artificial vegetation	Formula	Scope
Maza et al. (2017)	1:12	stem, root	$\tilde{C}_d = 9.49 \cdot Re^{-0.31}$	$500 < Re < 1700$
He et al. (2019)	1:10	stem, root, canopy	$\tilde{C}_d = 18.025 - e^{-0.06 KC_s}$	$10 < KC_s < 37$
Wang et al. (2022)	1:10	stem, root	$\tilde{C}_d = 0.42 + \left(\frac{0.77}{KC_s}\right)^{0.41}$	$0.01 < KC_s < 0.28$
Chang et al. (2022)	1:7	stem, root	$\tilde{C}_d = 1.15 + \left(\frac{14.70}{KC_s}\right)^{1.065}$ $\tilde{C}_d = 1.15 + \left(\frac{0.015}{Re_s}\right)^{1.044}$	$2.5 < KC_s < 20$ $180 < Re_s < 1300$
Bryant et al. (2022)	1:2.1	stem, root	$\tilde{C}_d = 0.86 + \left(\frac{1.24}{Re}\right)^{0.75}$	$0 < KC_s < 42$
Kelty et al. (2022)	1:1	stem, root, canopy	$\tilde{C}_d = 0.60 + \left(\frac{30000}{Re}\right)^{1.0}$ $\tilde{C}_d = 0.60 + \left(\frac{1019.9}{KC_s}\right)^{1.22}$	$4900 < Re < 119000$ $6.05 < KC_s < 407$
Zhang et al. (2023)	1:10	stem, root, canopy	$\tilde{C}_d = 0.60 + \left(\frac{20000}{Re}\right)^{1.41}$ $\tilde{C}_d = 0.60 + \left(\frac{80}{Ur}\right)^{0.75}$	$34900 < Re < 407000$ $0.73 < Ur < 21.33$

2.3.2. Non-linearity

The analytical formulations for wave attenuation as described in Section 2.2 are derived from linear wave theory. As waves reach the coast, however, wave non-linearity increases, causing waves to leave the domain of linear wave theory. The differentiation between these wave types is usually based on steepness and the Ursell number (Zhao et al., 2024). With increasing steepness and Ursell number, linear wave theory becomes less accurate at describing the velocities and wave profiles. The waves studied for wave dissipation in mangroves often lie outside the domain of linear wave theory, causing

inaccuracies in the outcomes. The damping factor β, for example, is dependent on the wave steepness (H/L), resulting in a decrease of $\tilde{C}_d$ (Phan et al., 2019; W. C. Wu & Cox, 2015). When finding the relationship between $\tilde{C}_d$ and Re or KC, the implications of non-linearity are also important. When determining the depth-averaged velocity for both KC and Re, this is most often determined using linear wave theory.

2.3.3. Scale effects in physical models

Due to the large size of mangrove trees, flume experiments are almost exclusively done with scale models. These scale differences bring difficulties in the comparison of different studies as well as converting the insights of these studies to real-world applications. To convert wave phenomena, as found in real-world scenarios, to experimental flume setups, scaling methods are needed.

Froude scaling relies on keeping the relation between gravitational and inertial forces constant, and is given by Equation (2.14).

$$Fr = \frac{U}{\sqrt{gL}} \tag{2.14}$$

Froude scaling is crucial is accurately representing wave characteristics at scales, and is therefore the dominant scaling method to keep the experiments most similar to the modelled realities. Reynolds scaling, on the other hand, relies on the continuity of the ratio of inertial to viscous forces and replicates the nature of boundary layer development, turbulence, and flow separation.

These processes are particularly important in mangrove systems, where complex root structures generate flow resistance and turbulence. Unfortunately, both scaling methods can't be applied simultaneously. As long as Reynolds numbers reach high enough values, flows around objects and turbulence will generally remain quite similar, leading to Froude scaling being chosen as the scaling method most often (Heller, 2017).

These scale effects, combined with model effects and measurement effects, often cause dissimilarities between modelled test and full-scale scenarios (Heller, 2011). A scale test for woody vegetation on a 1:10 scale, conducted by Kalloe et al. (2024), showed a 30% overestimation of maximum damping compared to full-scale tests. Causes attributed to these differences are the increase of viscous damping due to the lower Reynolds numbers found, especially at the smaller branches and flexibility differences.

These limitations of physical modelling highlight the value of numerical modelling as a complementary or alternative approach. Numerical models can simulate full-scale scenarios directly, without the need for scaling. This eliminates the errors that can arise in models due to mismatched Reynolds and Froude numbers. Furthermore, numerical simulations allow for greater control over boundary conditions, parameter sensitivity, and vegetation configurations.

2.3.4. Inertia

The drag force formulation for mangroves neglects the effect of the inertial force, assuming its insignificance in energetic wave climates. However, recent studies indicate that this assumption may not hold under calmer conditions. Inertia can become a dominant force at lower KC numbers, with some research suggesting that inertia remains significant for KC values up to 15 (Kelty et al., 2022), or even 25 (Chang et al., 2019). Omitting inertia in these lower KC ranges can lead to an underestimation of the total attenuation.

2.3.5. Wave period

The influence of wave period on damping remains inconclusive in the literature. Some studies report increased damping for shorter wave periods, while others report the opposite. Maza et al. (2019) states that for short waves, which are most often used in flume experiments, wave height plays a more significant role compared to wave period when it comes to attenuation rate. However, when comparing shorter wind waves to larger tidal waves, Q. Chen et al. (2021) observed smaller attenuation rates for the latter. These findings highlight the complexity of vegetation-induced attenuation.

2.3.6. Water depth
The relationship between water depth and total wave attenuation is highly dependent on the hydrodynamic and vegetation conditions. With higher water levels, a larger area of the mangrove is submerged, increasing the total frontal area. However, water depth generally reduces wave attenuation coefficients due to decreased interaction between waves and root structures (Mazda et al., 2006). In intermediate water, increased water depths also result in reduced orbital velocities, especially near the bottom where the roots are the most dense, further decreasing attenuation.

2.3.7. Wave height
Wave height has a positive relation with the wave attenuation rate. Larger waves have a higher orbital velocity, resulting in a stronger drag force (Maza et al., 2019). This trend also holds true for relative wave height (H/h), with higher ratios producing greater attenuation rates (Bryant et al., 2022).

2.3.8. Porosity effects
For mangroves, the influence of porosity has been studied, but was found to be negligible. For both wind-wave and storm-surge conditions, porosity can be neglected without significantly affecting model accuracy, and is thus omitted (Q. Chen et al., 2021; W. Wu & Marsooli, 2012).

2.4. OpenFOAM
OpenFOAM is a free, open-source Computational Fluid Dynamics (CFD) software toolbox widely used to simulate a large variety of complex fluid flows (Jasak, 2009). In wave modelling, it is often used for simulating free surface flows and interactions with structures. By solving versions of the Navier-Stokes equations, particularly the Reynolds-Averaged Navier-Stokes equations, it can solve complex hydrodynamic flow. Coupled with the interFoam solver, using the Volume of Fluid method, it can capture the interface between water and air, making it suitable for various academic and engineering purposes (Deshpande et al., 2012).

2.5. Similar studies
To highlight some of the different modelling methods used, three different approaches will be elaborated on. These approaches highlight the different levels of accuracy that can be used to determine mangrove-induced wave attenuation, and the challenges and insights from those studies.

2.5.1. Large-scale numerical models
van Wesenbeeck et al. (2025) performed over 200.00 model runs for mangrove coasts in all areas of the world. It shows that for large forests, with a width larger than 500 m, 75% or more of the incoming wave energy is dissipated, highlighting that by ensuring a large forest width, significant wave attenuation is guaranteed. It also shines extra light on the influence of the foreshore on wave attenuation due to bottom friction and depth-induced breaking.

2.5.2. 2DV Swan model
Suzuki et al. (2012) investigated wave attenuation of mangroves in the spectral wave model SWAN, using the drag formulation made by F. J. Mendez and Losada (2004) with a vertical layer schematization. Two main contributions are emphasised.

First, energy dissipation is computed by integrating the Morison-type drag force over depth. This method is validated against both the analytical model from F. J. Mendez and Losada (2004) and experimental data, showing excellent agreement.

Secondly, a layered schematization is introduced, allowing for different layers for trunks and roots. The energy dissipation is computed by integrating the Morison-type drag force over depth, with the drag force being computed individually per layer, and the total dissipation being the sum of contributions from each layer.

The model was calibrated and validated using flume experiments and field data, showing good predictive skill across a range of conditions with significantly reduced computational effort compared to full CFD approaches. But this approach does have the limitations associated with the simplified physics of

spectral models, especially within shallower water with complex bathymetry.

2.5.3. 3D OpenFOAM model

Maza, Lara, and Losada (2015) investigated Tsunami wave interaction for a 3D case in OpenFOAM after experimental results from Huang et al. (2011), which uses uniform, organised cylinders to represent mangroves. It uses two different approaches to replicate these experiments.

The first is a microscopic approach. This model replicates the exact cylinders used in the original experiment, accurately resolving the flow and drag around them. The findings of this method demonstrated good agreement with the model findings, but did have a large computational cost due to the fine mesh requirements.

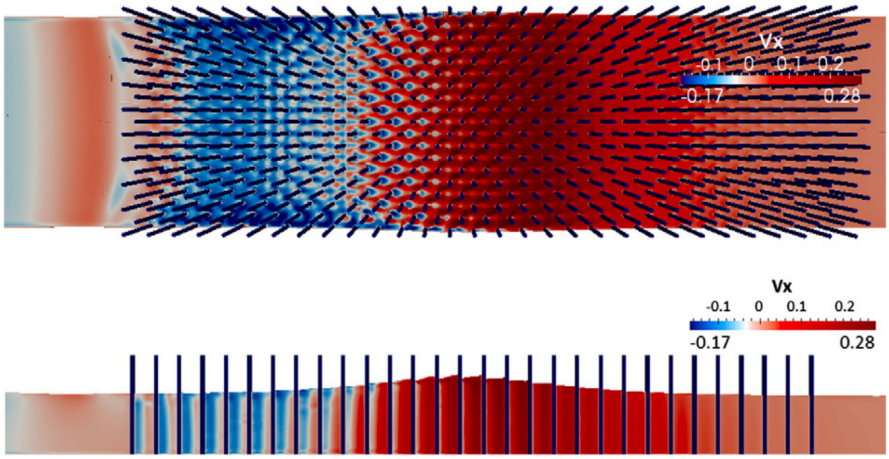

Figure 2.7: Horizontal flow velocities using the microscopic approach (Maza, Lara, & Losada, 2015)

The second approach, the macroscopic approach, Utilises volume-averaged URANS equations to simulate the vegetation effect. This approach applies the Morison equation and volume averages the drag over the total mangrove area. To guarantee a good fit with the experimental results, iteration over the $\tilde{C}_d$ value was necessary to calibrate the model. The runtimes of the model were, however, significantly shorter.

2.6. Field studies

Many different field studies have been done to measure actual attenuation caused by mangroves (Mazda et al., 2006; Quang Bao, 2011; Quartel et al., 2007). Depending on species, density and size of the mangrove forest, attenuation rates can differ vastly from small amounts of damping to fully dampened waves. Brinkman (2006) studied a site with some similarities to the Mandai area analysed in this study. It focused on fringing mangroves in Oonoonba, Australia, which has a 130 m wide coast with mainly Sonnerita in the front and Rhizophora at the back. The study showed wave heights being decreased by 75% over 80 m of mangrove forest. Another interesting study done by Horstman et al. (2014) shows the wave attenuation for two fringing mangrove coasts in southern Indonesia. Both coasts are comprised of a combination of Avicennia and Rhizophora. It showed attenuation rates of 0.002-0.003 m^{-1} for Avicennia and 0.012 m^{-1} for Rhizophora stretches. During storm conditions, wave heights were recorded to be decreased by 81% for a 102 m coast.

2.7. Takeaways

In conclusion, mangroves play a key role along the coast in enhancing flood safety, improving biodiversity and providing other vital ecosystem services. In Singapore, similar to other areas in the world, mangroves have declined over the last decade. But due to new recognition of their importance, this trend is slowly reversing.

Wave attenuation measurements from field studies reveal significant attenuation capacities of mangrove forests. Forests similar to those in the case study show attenuation rates in the range of 75%

for mangrove forests with lengths around 100 m, showing the significant effect it can have on coastal protection.

Numerical modelling can play a key role in predicting mangrove-induced wave attenuation as it allows predictions without the need for measurements or the interference of scale effects inherent in physical experiments. Different types of models can be used to make predictions on the wave attenuation of mangrove forests, the most promising of which schematises mangroves as cylinders to obtain a drag force following the Morison equation. Current models using this parametrisation, however, often calculate the drag force of mangroves by assuming a depth-averaged frontal area. In reality, the frontal area of mangroves has a high degree of variability.

The bulk drag force, a calibration parameter necessary for drag force calculations, is found analytically from the wave attenuation. These values have been shown to correlate with the Keulegan-Carpenter number, but this relation has a large degree of uncertainty. This makes it challenging to accurately predict wave attenuation for other scenarios, as it can only be accurately determined after wave attenuation measurements have been done.

To address these limitations, the development and application of a layered 2DV RANS model is proposed. Such a model could explicitly resolve height-varying characteristics and flow dynamics, potentially reducing uncertainty and improving the predictive capability of wave attenuation models in mangrove environments.

3

Introduction to flume experiment and case study

This study aims to show the capabilities of a 2DV OpenFOAM model to replicate and predict wave attenuation caused by mangrove forests. It does this by exploring two different models, a flume model and a case study model, each with its own different purpose.

Flumes provide a controlled environment in which wave behaviour can be studied. Unlike field studies, waves can be generated as necessary, measurements can be in optimal locations with high accuracy and vegetation structures can be simplified and measured. And with uniform characteristics along the depth of the flume, this lends itself well to 2DV simplifications. The purpose of recreating such a flume experiment is to show the capabilities of the mangrove model to recreate controlled environments and to compare model outcomes with accurate measurements.

Case studies, on the other hand, provide a larger challenge to recreate. Bathymetry, vegetation and wave parameters are often much more variable, with sometimes limited data availability. It is, however, essential for actual engineering purposes to find usable estimates and to gain an insight into the functioning of the system. Requiring assumptions to be made and the sensitivity of parameters to be analysed. The goal of this model is to demonstrate its functionality in simulating real-world scenarios, thereby gaining insights into its practical usefulness.

This chapter will give an introduction to the two different models created for this study, the flume model and the case-study model. It will delve into the background information and the necessary data that is further used in Chapter 4. The first part highlights the Flume experiment, discussing its experimental setup, the mangrove representation, hydrodynamic conditions and the results that were obtained from the study. The second and last section lays out the case study, its location, wave climate and mangrove information necessary for recreating it in the model.

3.1. Flume experiment

For this study, the flume experiment of Bryant et al. (2022) is replicated. It is a 1:2.1 scale model of a mangrove forest carried out by the United States Army Corps of Engineers. The goal of the study is to gain insight into the ability of an OpenFOAM model to reproduce wave attenuation caused by mangroves, specifically Rhizophora. By duplicating a representative mangrove scale model at regular intervals in the flume in combination with the placement of 16 wave gauges, quantitative information on the wave attenuation could be obtained. Using several different water heights and wave heights allows comparison of this wave attenuation for a multitude of hydrodynamic conditions.

3.1.1. Experimental setup

Rhizophora The experiments were carried out in a 58-meter-long wave flume with a width of 3 meters and a depth of 1.5 meters at the US Army Engineer Research and Development Centre in Vicksburg, Mississippi, as shown in Figure 3.1. A wave paddle was used to generate regular waves of specified height and period. A mild slope of 1:44 was featured to shoal waves before reaching the mangrove forest. The Flume ends with a dissipative beach to counteract reflection.

Wave gauges were installed along the flume to record surface elevations at various locations, spaced as shown in Figure 3.2. Larger refinement of the wave gauges is used towards the starting edge of the mangrove zone, with 4 gauges also measuring in front of it.

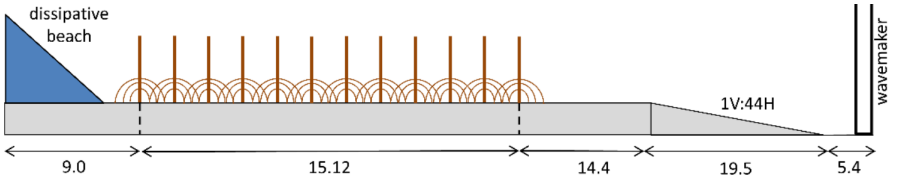

Figure 3.1: Wave flume setup used by Bryant et al. (2022)

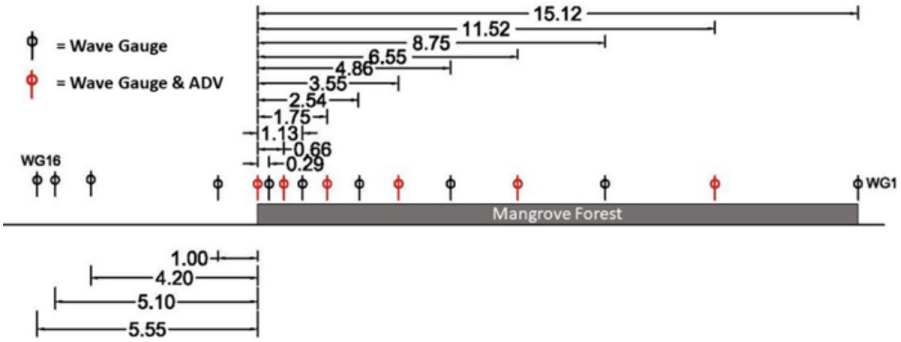

Figure 3.2: Wave gauges and their locations used by Bryant et al. (2022)

3.1.2. Mangrove representation

The mangrove representation was based on a combination of field measurements conducted in Florida on red mangroves in combination with the Rhizophora model made by Ohira et al. (2013). PVC and PEX pipes were used in the creation of the scale models, mimicking bending stiffnesses similar to those found in real Rhizophora trees, resulting in a scale model as shown in Figure 3.3. The 1:2.1 scale models are placed over a length of 15.12 meters with a density of 6.3 trees/m^2.

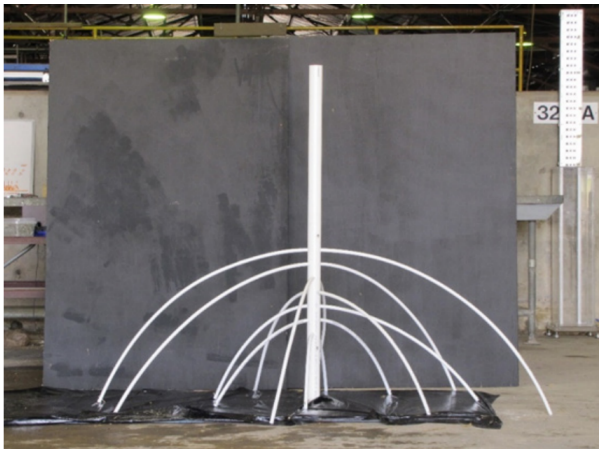

Figure 3.3: 1:2.1 scale Rhizophora mangrove model created from PVC and PEX pipes used by Bryant et al. (2022)

3.1.3. Hydrodynamic conditions

The experiment features a large scope of different hydrodynamic conditions with both regular as well as irregular waves. Water levels range between 0.35 m and 1 m, and wave heights range from 11.6 cm to 31.2 cm, with a total of 72 different hydrodynamic conditions. A full list of all conditions can be found in Appendix A.

Due to time constraints, a selection of hydrodynamic conditions was made to ensure a manageable modelling effort. The first discussion concerned the types of waves used, regular or irregular. Analysing irregular waves requires runtimes featuring at least 300 waves to obtain statistically relevant results. Regular waves require a significantly lower number of waves, reducing the required computational time. For this reason, regular waves have been selected for this study. The original experiment features 28

different hydrodynamic conditions for regular waves, exceeding feasibility for recreation and calibration. Therefore, a selection of 7 different hydrodynamic conditions is made.

The primary requirement for this selection was the stability of gauge measurements. Some conditions with high wave steepness showed larger fluctuations in wave gauge measurements, possibly attributed to reflection or instability in the wave. Since the aim of the flume model is to replicate the waves and wave attenuation of the experiment as well as possible, the 7 conditions with the least amount of perturbation in the wave gauge measurements were chosen. These 7 conditions have a water level of either $50cm$ or $70cm$ and wave periods ranging from $2s$ to $4s$. The full selection is shown in Table 3.1.

Hydrodynamic Condition (HC)	Water level h (cm)	Period (s)	Incoming Wave Height H_i (cm)
1	50	2.0	10.70
2	50	2.5	16.09
3	50	3.0	14.45
4	50	4.0	19.34
5	70	2.5	14.51
6	70	3.0	14.05
7	70	4.0	17.04

Table 3.1: List of the different hydrodynamic conditions analysed in this study

3.1.4. Results

The experiment showed varying wave attenuations over the different hydrodynamic conditions, ranging from 13% to 77% over the 15.12 meters of the mangrove area. A clear correlation was found between the damping coefficient and both wave steepness and relative depth, where β increased together with increases of both values. This correlation was even stronger when steepness and relative water depth were multiplied by a submerged volume fraction to account for differences in active frontal area with different water depths.

It also used the analytical formulation from F. J. Mendez and Losada (2004) to determine the bulk drag coefficient following Equation (2.10). Figure 3.4 shows this drag coefficient was then plotted as a function of both KC and Re, resulting in R^2 values of 0.6 for KC and 0.21 for Re.

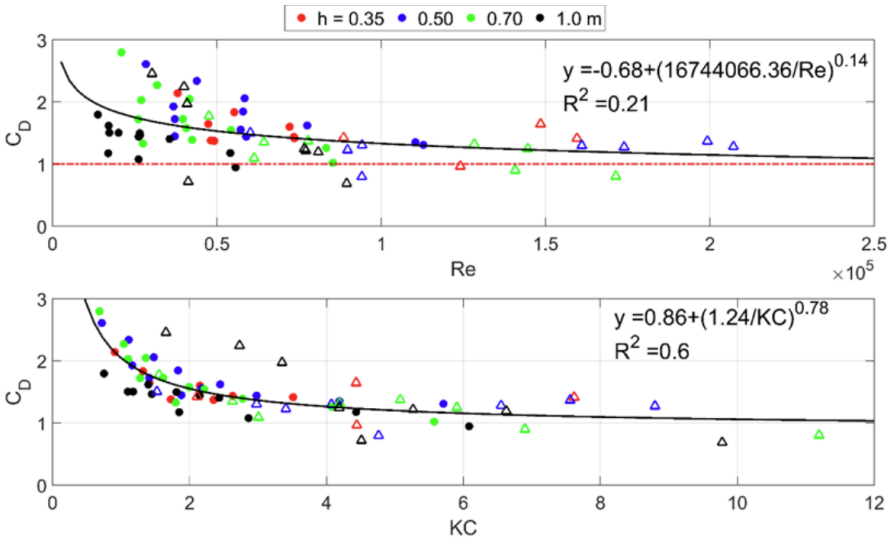

Figure 3.4: $\tilde{C}_d$ correlations found with KC and Re by Bryant et al. (2022)

3.2. Case study

To test the model in a real-life scenario, the Mandai mangrove area in Singapore is used as a case study. For the case study, the Mandai area, on the north-west coast of Singapore, is used. The Mandai area houses a fringing mangrove forest with a size of 15.4 ha (Yee et al., 2010). Despite its small it

houses a large range of flora and fauna (D. A. Friess et al., 2012). The model on the case study will focus on quantifying the expected wave attenuation from the mangroves, using data available of the area. A sensitivity analysis will be used to further develop an insight into the working of the system and the influence of different parameters. By getting insight into the wave attenuation of the mangroves in this area, levee design behind the forest could be optimised, leading to cost reductions.

3.2.1. Location

The Mandai area is situated on the north-west coast of Singapore in the Strait of Johor (Figure 3.5. The area lies in close proximity to the Sungei Buloh wetland reserve, which is an important nature conservation site for Singapore, and is planned to become a nature reserve itself in the near future (Shan, 2025). It features two rivers, the Sungei Mandai Besar in the south and the Sungei Mandar Kechil in the north. On the south-west side of the area, the Kranji dam can be found, which encloses the Kranji reservoir. Further to the east, the Johor Singapore Causeway is found, which blocks the passage of the Strait of Johor to the east.

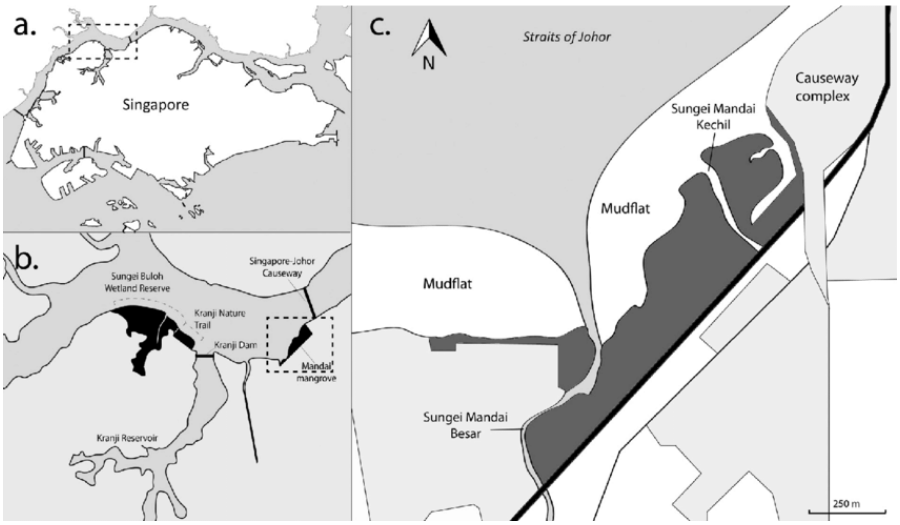

Figure 3.5: Location of the Mandai area within Singapore (D. A. Friess et al., 2012), where a. shows the country of Singapore, b. the north west coast including Sungei Buloh and the Kranji reservoir, and c. specifically on the Mandai mangrove area, highlighting the two rivers and mudflats

3.2.2. Transect selection

To assess wave attenuation through the mangrove forest, a representative transect was selected. The transect stretches along the longest fetch, in the westward direction, visible in Figure 3.6a. This captures the highest waves that face the Mandai area, and therefore the governing conditions, further detailed in Section 3.2.3.

The transect spans from the water ward's edge at the mudflat in front of the mangrove forest, stretching to the edge of the available bathymetry at the start of the levee behind the forest, shown in Figure 3.6b.

3.2.3. Wave climate

Overall, the site features low-energy hydrodynamic conditions. The tidal energy in the area is low since the water movement is restricted through the strait due to the causeway. It has a semidiurnal tide with a mean tidal range of 2.4 m and a spring tidal range of 3.9 m (Willemsen et al., 2016). The fetch, as shown in Figure 3.6a, is small, resulting in lower waves, with mean wave heights less than 20 cm (Bird et al., 2004).

Extreme scenarios

Earlier studies done on the wave climate for the north-west coast of Singapore highlighted many different wave scenarios with varying rates of exceedance as well as estimations for future scenarios, including rising sea levels and more extreme wave heights. To test the wave attenuation for mangroves in the most energetic conditions, the 10.000 year return period scenario will be modelled, which

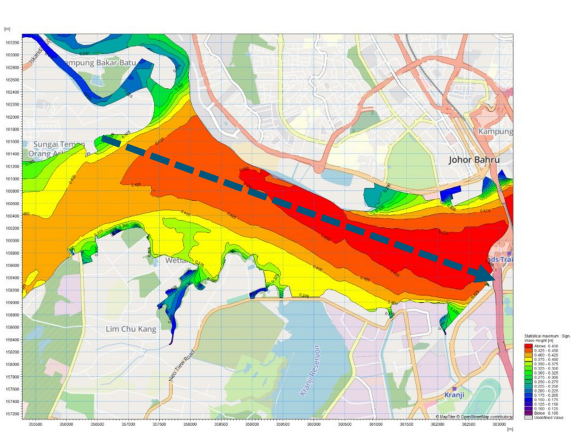

(a) Wave heights as determined by the spectral MIKE model for governing hydrodynamic conditions along with the governing fetch, along which the transect is defined.

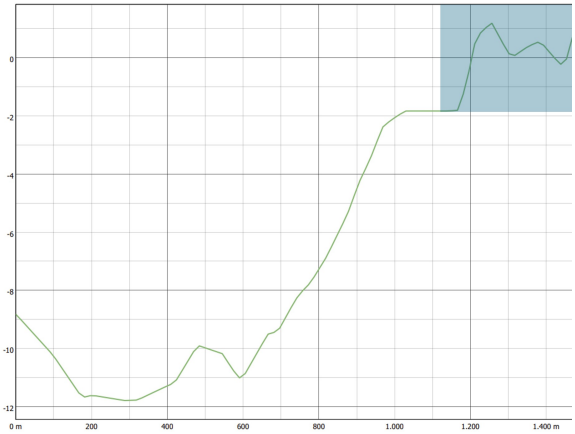

(b) Bathymetry along the fetch starting in deep water, with the modelled area highlighted.

Figure 3.6: Wave and bathymetric conditions along the case study transect.

is the highest risk probability consideration from the earlier study. By focusing on higher waves, it also allows the model to use slightly larger grid cells, reducing computational time. This 10.000 year return period scenario has the following governing conditions: Sea level = 3.59 m (+SHD), Hs = 0.4 m and T_p = 2.46 s.

Since mangroves can grow along with sea level rise (SLR), but can also be drowned with it, using the currently measured bathymetry in combination with future water level predictions can lead to misrepresentations of the actual scenarios. For that reason, no future scenarios are considered, but the model will be set on the currently expected governing conditions.

Wave calculations from earlier studies

Following these conditions, a spectral MIKE model was made to assess the wave height all over the area as seen in Figure 3.6a.

To gain specific and accurate wave conditions as input for the OpenFOAM model, a larger OpenFOAM simulation was made. The goal of this model was to determine wave inputs for the more shallow area at the start of the Mandai area, thus reducing the necessary size of the final model for which many different scenarios need to be run. This modelled an extended transect along the dominant fetch, starting from deep water in the middle of the Johor Strait. It uses as input the wave characteristics found from the spectral MIKE model at deep water, where depth has no influence on the waves. Measuring the waves again at the starting point of the final model, in shallower water, gave the following characteristics. H_{m0} = 0.49 and T_p = 2.8. This gives the design conditions laid out in Table 3.2:

Table 3.2: Design conditions for a 10.000 year return period as used as inputs for the model

	H_{m0} (m)	T_p (s)	sea level (m+SHD)
Design conditions	0.49	2.8	3.59

3.2.4. Mangroves

To model the wave attenuation of mangroves in the Mandai area, information of these trees is necessary. This section will explore the available data of the area, subdivided into three sections: species, composition, mangrove extent and spatial variability. Despite data being limited, as is often the case for such projects, there are several useful measurements on the area with which some well-informed assumptions can be made.

Species compositions

The field survey from Tembusu (2024) found 13 different mangrove species in the area, including rare species such as casuarina and sea hibiscus. The most common species found were Sonnerita, Avi-

cennia and Rhizophora. Sonnerita and Avicennia are found more towards the seaward edge, and Rhizophora more towards the back. An overview of some images highlighting the mixture of species throughout the Mandai is found in Appendix B.

Temporal variability

Inspecting the temporal variability can give insight into possible future scenarios on the mangrove extent in the area. It can answer questions on the stability of the forest, whether it has recently been increasing or decreasing or on the density and maturity of the forest

The field survey of Tembusu (2024) compared measurements on the same plots for 2019 and 2022, giving insight into changes in those three years. Canopy cover, average DBH, and tree height varied between increasing and decreasing over the different plots, but showed no clear trend. Tree health was observed as good for both years There was a slight change in the dominant species observed in some areas. With Rhizophora, Sonnerita and Avicennia all leaving one of the plots. This could be the result of changes in the environment, but might also be attributed to natural mangrove dynamics.

Using satellite imagery, more information on the mangrove cover can be obtained. Using Google Earth, imagery from multiple years is obtained. Comparing the most recent image from 2024 with the image of 2022 in Figure 3.7 shows very few changes over the last year. earlier years do, however, show a more reduced forest cover in the past. In 2015, the forest cover showed to be significantly less than in the earlier years. Going back in time even further shows a much more extended cover again, much more likely to be that of recent times. The combination of these would indicate a big decrease in mangrove extent, either by a sudden large event, such as flooding, or gradually due to environmental changes. The forest then recovered from this in the last 10 years with increased growth, which is stabilising more over the most recent years, with mangrove cover changing less.

When inspecting the periods of decreased mangrove extent, the remaining mangroves seem to be grouped on the higher lying areas where less inundation time is experienced. Mangroves on the fringes, either on the seaward side or near the creeks, have died in these times.

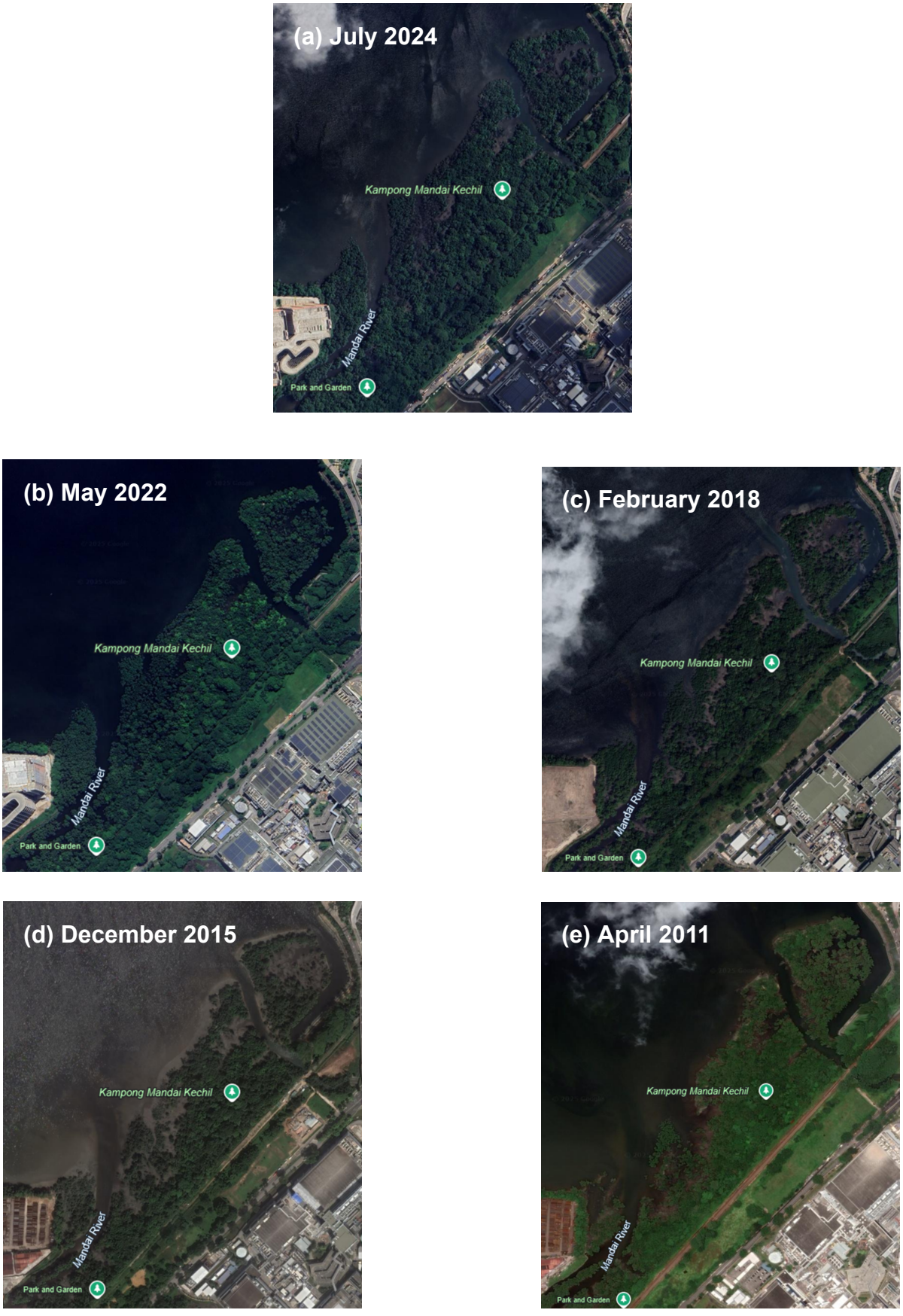

Figure 3.7: Temporal changes in mangrove biomass distribution at Mandai over a period of 13 years (2024–2011). (Google Earth, 2024)

4
Methodology

This chapter outlines the methodological framework used in this study. Building further on the background information and data laid out in Chapter 4, this chapter discusses the settings and considerations in setting up the two different models as well as the assumptions used in creating these models.

Additional model settings such as boundary conditions and numerical schemes can be found in Appendix C. Methods for data analysis can be found in Appendix D. The implementation of mangroves in OpenFOAM can be found in Appendix E. The numerical schemes used in the fvSchemes and fvSolution files can be found in Appendix F.

4.1. Flume experiment

The flume model replicates experiments conducted by Bryant et al. (2022), as discussed in Section 3.1. The goal of replicating this model is to show the capabilities of an OpenFOAM model to replicate physical processes in a controlled, well-measured environment.

4.1.1. Geometry

The geometry of the OpenFOAM model will replicate that of the experiment. The full setup is shown in Figure 4.1. To reduce computational time, the slope and area in front will be left out. Instead, the geometry will be flat with wave inputs coming from the measured wave heights in front of the mangrove forest. To accommodate wave generation in the model, an empty zone, 14 meters in length, is featured in front of the mangroves. To accommodate the flow of air in the cases of high waves and water levels, the total height of the flume is set to 1.4 meters.

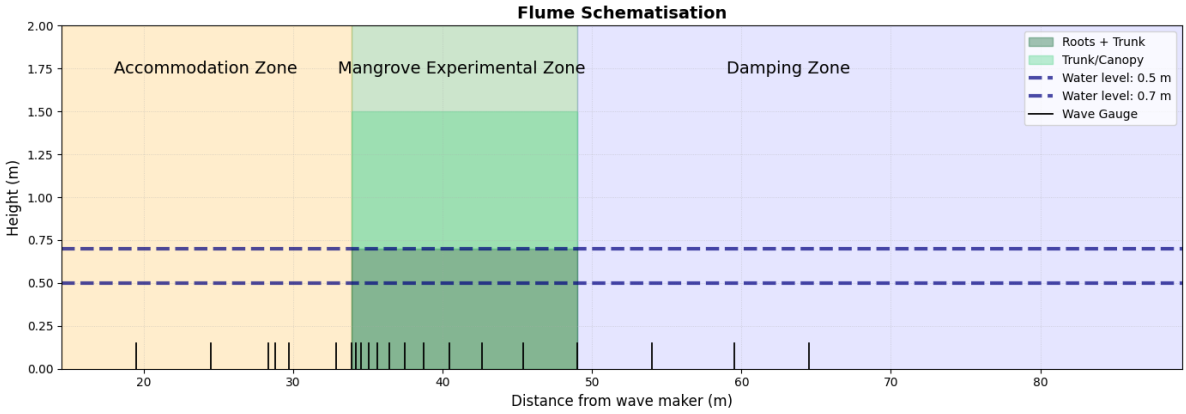

Figure 4.1: Flume schematisation as used in the numerical model.

The wave gauge locations from the experiment are directly copied into the model from the original locations of the physical experiment. To analyse the wave development at the beginning of the flume and the damping in the mangrove damping zone, extra wave gauges are added towards the extremities of the flume.

4.1.2. Mesh

The mesh needs to be designed to balance accuracy and computational time. Decreasing the cell size enhances model accuracy but also increases computational time. A commonly used guideline for cell size is that the maximum grid size should be set between 1/8th and 1/10th of the wave height. This also needs to remain true after the wave is attenuated. The mesh that suffices for the smallest waves is then used for all other cases. To further optimise the mesh, finer resolution will be applied above and below the water surface, as processes near the free surface require higher precision for accurate representation. To capture the full wave, the refinement is applied to one wave height on top as well as below the water level. Restricting this refinement to this confined area rather than the whole flume ensures computational time is optimised.

To reduce computational times and to align the grid cells more with the velocity magnitudes found in shallow and intermediate waters, rectangular grid cells are used. Following the research by Maza, Lara, and Losada (2015), a scale of 1:3 is chosen with the horizontal length being triple the vertical length of each grid cell. The cell height is chosen to be 1.4 cm, remaining in the range of 8 cells per wave height, even for the lowest waves. The surface level refinement further decreases this cell size to 0.7 cm to make sure the dampened waves remain properly modelled.

4.1.3. Turbulence

The model was initially tested using a $\kappa - \epsilon$ turbulence closure. This proved, however, to be unwanted. By modelling turbulence, wave attenuation was drastically overestimated, leading to unrealistic results (Figure 4.2). This is a known problem with 2DV modelling in OpenFOAM, and turbulence is generally turned off (Larsen & Fuhrman, 2018).

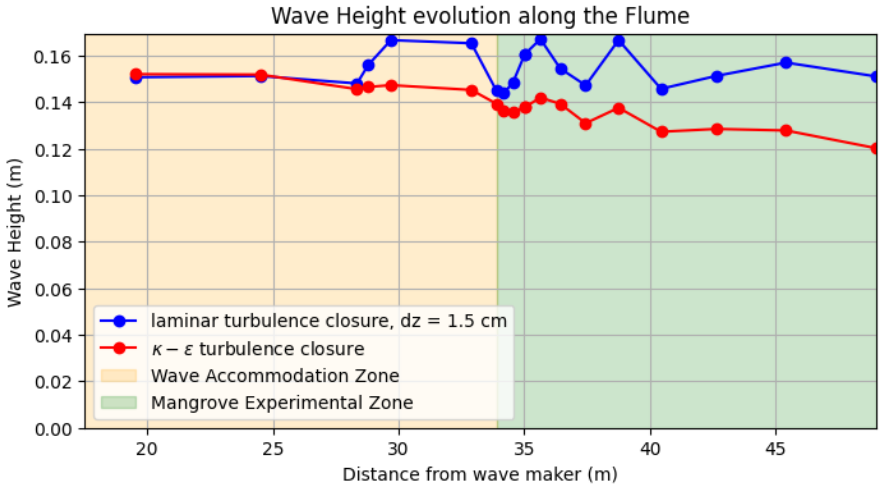

Figure 4.2: Wave height evolution along the flume 2 runs, with different turbulence closures. The laminar turbulence closure, showing no direct decrease in wave height over the length of the flume.

4.1.4. Reflection

In early tests of the OpenFOAM model, reflection resulted in interference. These runs relied solely on the shallow water absorption outlet condition to combat reflection. Multiple solutions were tested to combat this problem. Multiple iterations of ramps were tested. This would replicate the dissipative beach in the physical experiment, but it showed too much reflection, with local spikes of 15% of the incoming wave height, where no significant variations should be present. A simple extension of the flume also showed decreasing reflection, but this was due to turbulence still being implemented in the model, and now having a larger length to dampen the waves.

After testing multiple different new solutions to this problem, shown in Figure 4.3, the best solution was a combination of two implementations. The first implementation was the extension of the mangrove forest by 40 meters. This naturally dampens the wave. The second implementation was to increase the grid size behind the experimental extent of the mangrove forest. There, locally, the grid cells are quadrupled

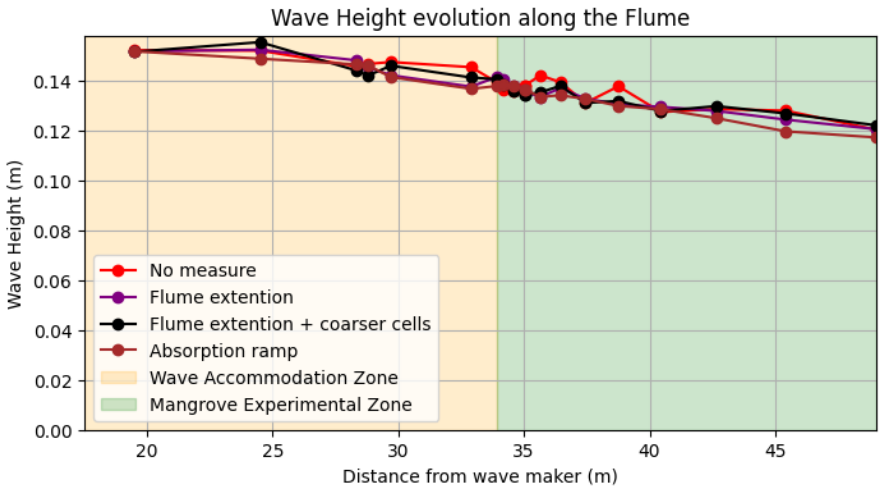

Figure 4.3: Different damping measures and their results on reflection. In a flume without mangroves, with a $\kappa - \epsilon$ turbulence closure, also resulting in additional damping

in size, now with a height of 5.6 cm and a length of 16.8 cm. Besides extra numerical damping, this also provides a drastic reduction in the number of grid cells, allowing for faster computing of the model.

4.1.5. Wave input

The wave input follows from the selection made in Section 3.1.3. Wave generation in OpenFOAM is done with each hydrodynamic condition being generated by its accompanying wave theory. This ensures that the wave shape is modelled correctly. This accompanying wave theory is determined based on the diagram from Le Méhauté (1976). Except for hydrodynamic condition 1, all conditions follow Cnoidal wave theory. Condition 1 follows Stokes II theory.

Determining the incoming wave is not straightforward. Wave heights from the experiment are known at the location of the wave paddle, where shoaling has not occurred yet, and right in front of the mangrove forest, where wave heights have increased due to the resistance of the mangrove area. Thus, the wave heights must be determined iteratively to match the modelled wave height to the measured wave height in front of the mangrove forest. As Figure 4.4 shows, the measurements of the wave height have imperfections and do not completely follow the fitted attenuation line. This means that only choosing a single point for this iteration could lead to big errors. For this reason, the wave height, at the location of the forest start, as predicted by the fitted curve, is used for both the experimental data and the model as the iterated value, denoted as H_i.

Table 4.1: Different hydrodynamic conditions analysed in this study

Hydrodynamic Condition (HC)	Water level h (cm)	Period (s)	Incoming Wave Height H_i (cm)	β	Wave Theory
1	50	2.0	10.70	0.0722	Stokes II
2	50	2.5	16.09	0.0835	Cnoidal
3	50	3.0	14.45	0.0628	Cnoidal
4	50	4.0	19.34	0.1028	Cnoidal
5	70	2.5	14.51	0.0441	Cnoidal
6	70	3.0	14.05	0.0391	Cnoidal
7	70	4.0	17.04	0.0549	Cnoidal

4.1.6. Mangrove parametrisation

The drag force exerted by mangroves is calculated using a layered approach based on the Morison equation, as outlined in Section 2.2.2. Distinct layers are used to capture the variations in the frontal area over the height of the trees. Using scans of the physical model, the height-varying frontal area was computed (Bryant et al., 2022). This information is used to create 4 different layers, laid out in

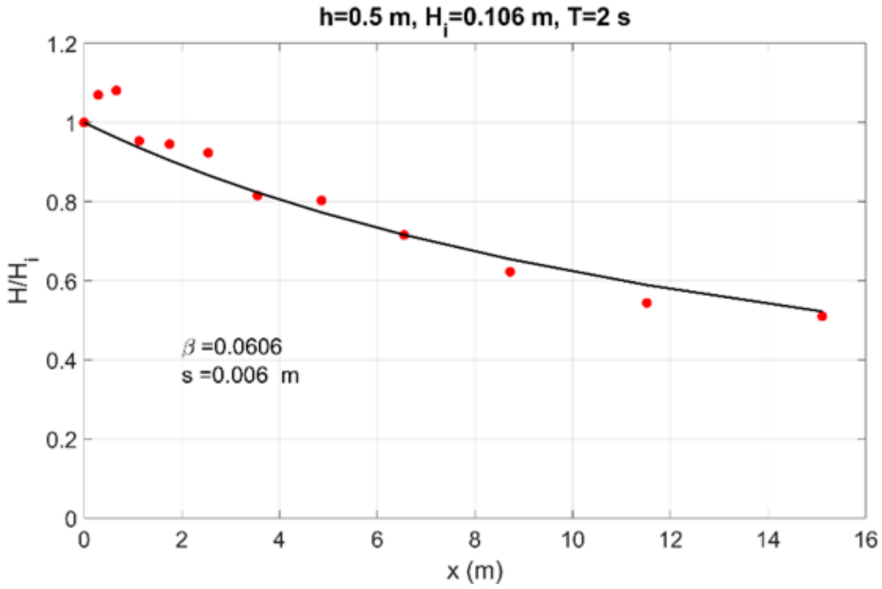

Figure 4.4: Wave height measurements with fitted decay curve for HC1 (Bryant et al., 2022)

Table 4.2, each using the average frontal area of that layer. These averaged values, when combined with the corresponding parameters in the Morison equation, yield distinct volume-averaged drag forces for each layer, thereby capturing the non-uniform distribution of vegetation drag throughout the water column. Figure 4.5 goes over these steps.

Table 4.2: Average frontal area per meter height for different vertical sections.

Layer	section range(m)	Average width (m^2/m)
4	0.70 – 1.50	0.060
3	0.50 – 0.70	0.164
2	0.35 – 0.50	0.261
1	0.00 – 0.35	0.290

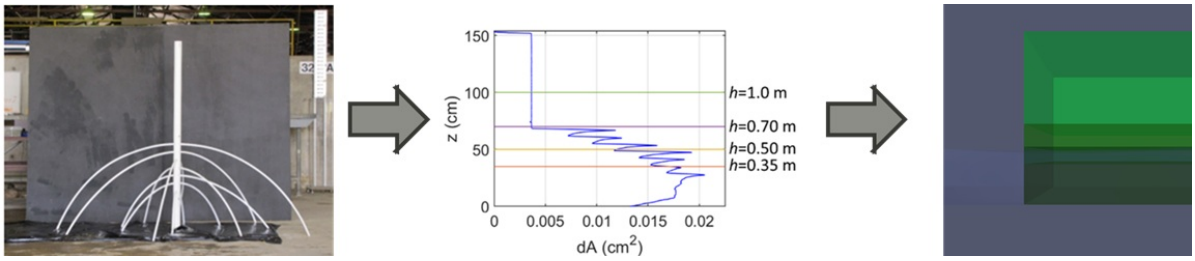

Figure 4.5: Steps from scale model to frontal area to implementation of varying layers in OpenFOAM

4.1.7. Model Calibration

To evaluate the model's accuracy in representing the physical processes of the flume experiment, calibration is performed. This process consists of two main steps: a mesh sensitivity analysis and wave shape validation.

The first step in analysing the mesh performance is to inspect the numerical dissipation. This is achieved by comparing the wave heights along different mesh configurations in an empty flume. To quantify the numerical damping, the wave height at the last gauge of the experimental mangrove zone is used for comparison, with the results of the finest mesh as the benchmark.

Since the mesh size is more critical for smaller waves, HC1 is used to establish mesh performance, as this hydrodynamic condition features the smallest waves, 10.7 cm. To avoid interference from wave reflections, the arrival time of the first reflected wave was estimated based on the wave celerity of 2 m/s, resulting in a reflection time of approximately 50 s. The average wave height of the last five waves before this time was used for comparison. The mesh configurations tested are summarised in Table 4.3.

Run	dx (cm)	dz (cm)	dz as % of H
Finer mesh	1.74	0.58	5.92
Normal mesh	2.10	0.70	7.14
Coarser mesh	2.63	0.875	8.93
Coarser mesh 2	2.91	0.97	9.92

Table 4.3: four different mesh configurations and their corresponding values as used for the sensitivity analysis for the flume model

The second step focused on validating the wave generation method, since there are many different possibilities in OpenFOAM for wave generation. For each hydrodynamic condition, the modelled wave profile in front of the experimental mangrove zone is overlaid with the measurements from the wave gauges in the experiment. If discrepancies are observed, alternative wave generation methods are tested until a satisfactory match is achieved.

4.1.8. Bulk drag force calibration

The bulk drag coefficient, $\tilde{C}_\mathrm{d}$, is calibrated iteratively using experimental wave height measurements obtained from the physical flume setup.

The accuracy $\tilde{C}_\mathrm{d}$ is often assessed by comparing simulated and measured H_{M0} values at the last wave gauge at the end of the flume (WG1) given an incoming wave height. The experimental measurements, however, often can have substantial deviations from the trend line in the attenuation. Using a single point as a calibration value can introduce a large error. Using the damping coefficient, β, as a calibration value can drastically decrease the error, as it accounts for attenuation along the forest and thus reduces the impact of perturbations in a single wave gauge on the results.

Calibration is considered complete when the modelled wave height decay corresponds to a β value within 3% of the experimentally derived value. Initial estimates for $\tilde{C}_\mathrm{D}$ are based on values reported by Bryant et al. (2022), found through the analytical formulation. Since a higher incoming wave height can also influence the β values, both h and $\tilde{C}_\mathrm{d}$ need to be calibrated together.

4.1.9. Validation

To assess the accuracy and reliability of the flume model, two complementary validation approaches were employed: Comparison of the wave height evolution for single runs and analysis of the iteratively obtained $\tilde{C}_\mathrm{d}$ values.

Wave height evolution

Firstly, comparing the spatial evolution of wave heights between the model and experimental measurements. This comparison is conducted for each hydrodynamic condition to evaluate the model's ability to replicate wave attenuation through the mangrove zone. A good agreement in the rate of wave height decay would indicate that the model accurately captures the physical damping effects of vegetation, given the right parameterisation and drag force calibration.

Calibrated bulk drag coefficient

The second step of validation involves interpreting the calibrated bulk drag coefficient. In most studies, $\tilde{C}_\mathrm{d}$ is determined from the analytical formulation, as discussed in Section 2.2.2. $\tilde{C}_\mathrm{d}$ values for the flume experiment were also obtained this way. When related to the Keulegan-Carpenter number, this relation showed an R^2 value of 0.6, signifying a mild correlation, comparable to other studies. This formulation relies on the assumptions of linear wave theory and depth-averaged frontal area, which is, however, not valid for any of the hydrodynamic conditions.

The hypothesis for this model is that, by using calibration with a RANS model, the uncertainty of this relation can be reduced. The reason for this is that instead of relying on the analytical formulation, which is based on linear wave theory, the determination of $\tilde{C}_\mathsf{d}$ can now be based on findings using a RANS hydrodynamic model, which is not limited to linear wave theory. To address this limitation, the hypothesis proposes that calibration using a Reynolds-Averaged Navier–Stokes (RANS) model with a layered frontal area approach could reduce the uncertainty in the correlation between $\tilde{C}_\mathsf{d}$ and KC. This approach has two advantages over the analytical approach. It does not rely on assumptions of linear wave theory, but can model hydrodynamic conditions that fall outside of the ranges of this theory. It can also represent the variation in frontal area over the height of the mangroves better by using multiple layers with average frontal areas. This is a more realistic parameterisation than the assumption of a uniform average area over the height of the mangrove.

To test this hypothesis, for all 7 wave tests, the KC-$\tilde{C}_\mathsf{d}$ relations will be determined with both the analytical and model-iterated $\tilde{C}_\mathsf{d}$ values. Finding improved R^2 values for the iteratively found $\tilde{C}_\mathsf{d}$ would then support the hypothesis. Furthermore, the obtained $\tilde{C}_\mathsf{d}$ will also be compared with those found in literature Kelty et al. (2022), Lopez-Arias et al. (2024), and Maza et al. (2019) to inspect the relation to those findings and provide a wider reference frame.

4.1.10. Effect of the layered approach

To inspect the influence of using the layered frontal area representation on wave attenuation, this layered approach, as used throughout this study, is compared to a more traditional approach with a depth-averaged frontal area. This entails that the frontal area used is constant over the depth, the average of the total submerged area.

The analysis focuses on HC5 and involves a comparison of the wave attenuation following each approach, using the same $\tilde{C}_\mathsf{d}$. A calibration for the depth-averaged approaches was performed to give further insight into the difference between the two approaches. Comparison will be done on the β values obtained from each case, showing the attenuation differences.

To further analyse the influence of the layered approach, velocity profiles will be examined. Both approaches will use their own calibrated $\tilde{C}_\mathsf{d}$, enabling comparison between velocities of the same magnitude.

4.2. Case study

The case study will focus on capturing the wave attenuation properties of the Mandai area on the northwest coast of Singapore. The goal of this simulation is to show the capabilities of a 2DV OpenFOAM model in real-world scenarios. Similar to the previous section, this section will focus on the model setup, specifically for the case study. Large parts of the setup will have a similar methodology, but due to the added complexity compared to the flume, some steps will differ significantly. For a comprehensive overview of the study area and data availability, see Chapter 3.

4.2.1. Geometry

To represent the governing conditions for the Mandai forest, a transect is chosen along the longest fetch that reaches the forest with waves coming from the east. To reduce computational time, the domain is chosen right in front of the mangrove forest.

The bathymetry used is provided by the Singapore Land Authority. It is based on a combination of nautical charts with extra point measurements added, merged in a grid with $5m$ spacing. it originates from 2019 and is the most up-to-date Bathymetry of the area available as far is known.

The number of points of the bathymetry is reduced in the model by selecting the 10 most crucial reference points, leading to the bathymetry representation as can be seen in Figure 4.6.

Wave gauges are placed every 30 meters with extra refinement towards the forest edges to allow for a more detailed view of the wave heights in these locations.

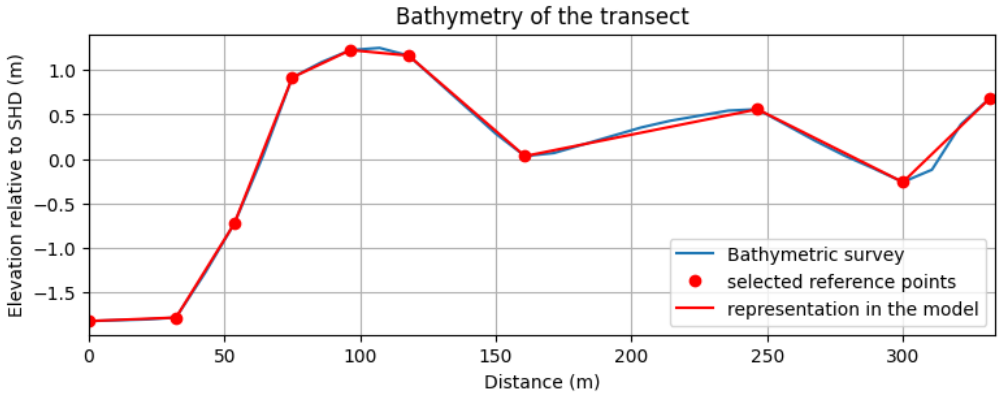

Figure 4.6: Bathymetry of the transect with both points from the original bathymetry as well as the representation in the model

4.2.2. Mesh

The meshing approach generally follows the same methodology of Section 4.1.2, but a few key differences. An additional refinement is applied at the water surface to account for the irregular wave conditions in the case study. Specifically, the mesh is refined over a vertical span of H_{M0} both above and below the waterline, as $2H_{M0}$ is considered a reasonable estimate for the maximum wave height. To reduce computational time, the surface is double refined, resulting in grid cells that are four times smaller compared to those in deeper areas. A transition layer with single refinement is used between the double-refined layer and the non-refined layer to make the change more gradual. To accommodate the bathymetry and allow for a smooth integration, an extra refinement layer is also added at the bottom of the model. This mesh is displayed in Figure 4.7.

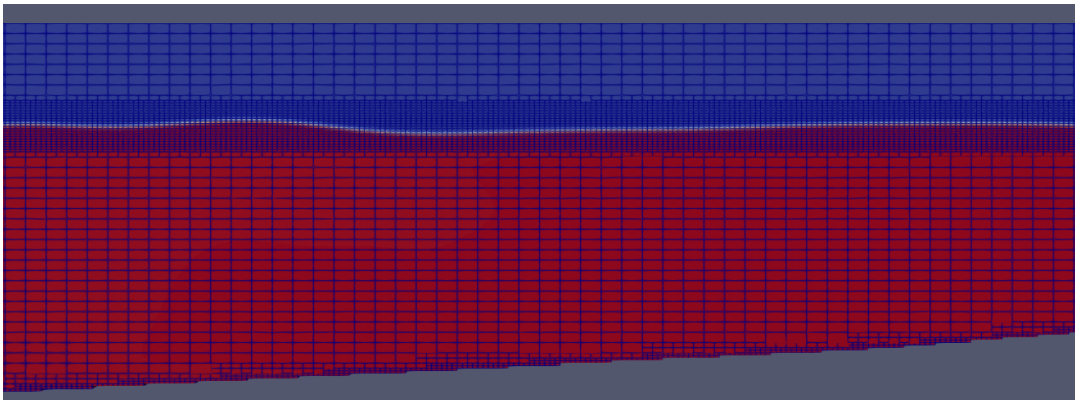

Figure 4.7: Mesh of the case study with refinement at the surface and bottom. Waves are shown from the air-water interface at the edges of both colours.

Similarly to the flume model, rectangular grid cells are used to decrease computational time. From tests with adding ramps to the flume model, rectangular grid cells sometimes caused instabilities in the model in places on non-flat bathymetry. For that reason, the ratio of dz/dx is increased from 1:3 to 1:2. This resulted in a stable model while still decreasing computational time. The smallest grid cell dimensions used at the surface are measured, dz = 5cm and dx = 10 cm. This is the finest resolution that allows the model to finish within the maximum available computational time on the DelftBlue supercomputer (DHPC, 2024).

4.2.3. Reflection

Reflection is generally more problematic in regular wave conditions and is expected to be less significant for the irregular waves used in this case study (Maza et al., 2019). The case study model uses the shallow water absorption outlet condition similar to the flume model, but no further damping zone is added.

4.2.4. Wave input

From the earlier studies, as discussed in Section 3.2.3 H_{m0} = 0.49 m and T_p = 2.8 were found as input values. Using these H_{m0} and T_p in combination with a JONSWAP spectrum with peak enhancement factor γ = 3.3, gives the wave inputs for the final model. Using a JONSWAP spectrum is common for overtopping designs and gives conservative estimates compared to other spectra.

Waves are generated using the *irregularMultiDirectional* wave model in OpenFOAM.This model creates irregular waves in multiple directions. But since only one direction is needed in this 2DV model, the directional value is set to 0. The other inputs for this, wave period, wave height, and wave phase, are generated to represent the wave spectrum as stated above. Wave heights follow from the JONSWAP formulation. The frequency range is selected between 0.1 and 1.5 s^{-1} since extension on either side resulted in no significant changes to the spectrum. 300 spectral components were used to capture this spectrum. The inputs for wave phases are obtained by random sampling between the values of 0 and 2π. These inputs are kept constant to retain the same sequence of waves for each run.

4.2.5. Mangrove parametrisation

For the case study, there is more uncertainty regarding the species and densities of the study area. Recent studies reveal that the area consists of a combination of different species, with Avicennia being more prevalent on the seaward side and Sonnerita and Rhizophora taking dominance landwards. For the purpose of this study, the area is assumed to be uniformly inhabited by Rhizophora species. To determine the effect of this assumption, one sensitivity run will be done with Avicennia dimensioning.

Finding the average frontal area of a mangrove forest is a challenging task. Where the flume study used a replica of a model in continuous intervals, real-world forests are much less predictable. There is a large variety in tree heights, shapes, densities and even species. Since there are no tree measurements for the area, estimations and simplifications have to be done in order to find useful values as input for the model.

As presented in the previous chapter, the study site consists of a large variety of species, including Sonnerita, Avicennia and Rhizophora. To simplify the model, it is chosen to represent the area as a uniform Rhizophora forest. This enables better comparability with the flume study. The frontal area of Avicennia will, however, also be tested in the sensitivity analysis to highlight any shortcomings in this simplification.

The frontal area of the Rhizophora roots is based on the simplification from (Horstman et al., 2013). These measurements were done on the east bank of the Mae Nam Trang in Thailand, 6 km from the open sea. Similar to the Mandai site, this study area also featured creeks. These measurements have also already been used as root dimensioning for earlier studies of the north-west coast of Singapore (Broekema, 2013).

Canopies are outside of the scope of this study and are out incorporated in the dimensioning. Although they are sometimes known to contribute to the attenuation capacity, their flexibility inhibits them from being incorporated in this approach (Zhang et al., 2023). Incorporating the frontal area of the canopy would lead to an overestimation of the drag forces from the Morison equation.

Since the trunk also contributes to the attenuation capacity of mangroves, it is added to this schematisation. From the field survey from 2022, an average DBH (Diameter at Breast height) of 14.3 cm was found. For this approach, this diameter is assumed to be constant over the height, whereas in reality it decreases higher up the tree. This decrease is assumed to be more than compensated for by the omission of the extra resistance from branches and foliage of the canopy. The height of the mangroves from the survey was found to be above 10 meters, reaching far above any possible hydrodynamic condition.

Table 4.4: Schematisation of frontal area layers based on vertical distribution of Rhizophora roots from (Horstman et al., 2013) in combination with field measurements of DBH from (Tembusu, 2024)

Layer	Height Range [m]	Stem Diameter [m]	Number of Stems	Total Frontal Area per Tree [m²]	Frontal Area per m² [m²/m²]
1	0.00–0.10	0.023	168	3.864	0.46368
2	0.10–0.50	0.024	76	1.824	0.21888
3	0.50–1.50	0.024	42	1.008	0.12096
4	1.50–2.00	0.036	9	0.324	0.03888
5	2.00–10.00	0.143	1	0.143	0.01716

The tree density is set at 0.12 trees/m^2, as found by the field survey from 2022 for the A3 plot containing mainly Rhizophora. This gives the average frontal area for Rhizophora mangroves as shown in Table 4.4 and visualised in Figure 4.8.

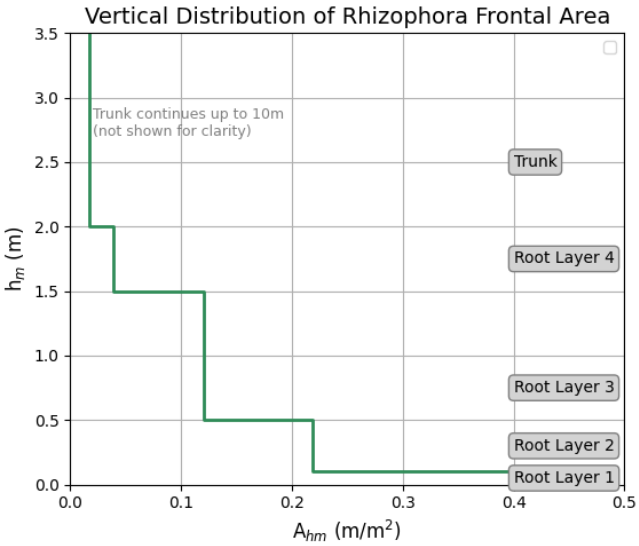

Figure 4.8: Schematised averaged frontal for the Rhizophora forest

The schematisation for the Avicennia run consists only of 2 layers, the pneumatophores and the trunk, since those are the two main attenuation parts of the tree besides the canopy, which is also not considered for the same reasons as for the Rhizophora schematisation. The dimensions of this schematisation are based on the measurements from the field survey. The Tree density for Avicennia officinalis found in that study was 0.13 trees/m^2 with a DBH of 11.4 cm, also assumed to be constant over the tree heights, which exceed 10 m. Pneumatophores were mentioned with a density of 70.4 (n/m^2), an average height of 22.4 cm, and an average diameter of 9.6 mm (Table 4.5).

Table 4.5: Schematisation of frontal area layers based on pneumatophore and DBH measurements from Tembusu (2024)

Layer	Height Range [m]	Stem Diameter [m]	Number of Stems	Frontal Area per m² [m²/m²]
Pneumatophores	0.00–0.224	0.0096	70.4 (n/m^2)	0.6758
Trunk	0.224–10.00	0.114	1	0.0148

Unlike the flume model, the case study will not undergo calibration and validation with respect to $\tilde{C}_d$. Since there are no measurements on wave attenuation available, this is not possible. Instead, similar to most field study models, a value of 1 will be used, giving a conservative estimate of the expected damping, since $\tilde{C}_d$ values are almost exclusively greater than 1 (Lopez-Arias et al., 2024).

4.2.6. Mangrove extent

The location of the mangrove trees is determined based on satellite images from Google Earth (Google Earth, 2024). The last of these images is taken in July 2024. Since the temporal variability in the mangrove extent is low in recent years, as discussed in Section 3.2.4, it can be assumed that the situation as captured by the satellite imagery differs little from the current situation.

By overlaying the satellite images with the bathymetry profile, it shows that points of lower bathymetry correspond to non-vegetated areas.

From the overlay, shown in Figure 4.9, it is estimated that at the front of the mangrove forest, where wave action is more abundant, the governing bathymetry level for mangrove growth is set at 0.5 m. In the more sheltered areas of the mangrove forest, next to the creeks, this limit is set at 0.2 m. This results in three distinct mangrove areas with a total length of 183 m.

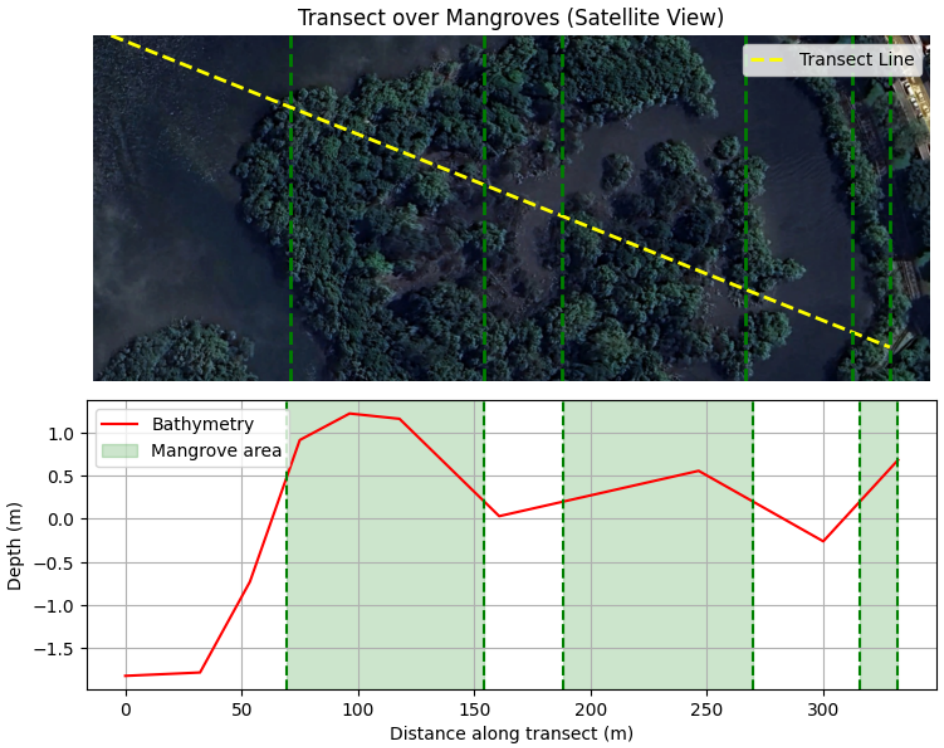

Figure 4.9: Mangrove extent obtained by overlapping satellite imagery with the local bathymetry (Google Earth, 2024)

4.2.7. Calibration

Similar to the flume study, calibration on mesh size must be done. Due to constraints in computational time, no smaller meshes can be compared, since the selected mesh size is the smallest attainable size. Comparing smaller meshes can still inform on the performance of the mesh by highlighting the differences. The meshes to be compared have the following dimensions: dz = 5 cm, dx = 10 cm (selected mesh), dz = 6.25 cm & dz = 12.5 cm and dz = 7.5 cm & dx = 15 cm (Table 4.6. The meshes are tested for the base case with mangroves since that is where the smallest wave heights are expected, and thus, the highest sensitivity to mesh size.

Table 4.6: Mesh configurations and their corresponding values used for the sensitivity analysis of the case study

Run	dx (cm)	dz (cm)	dz as % of H_s
Selected mesh	10	5	10.2
Coarser mesh	12	6	12.24
Coarser mesh 2	14	7	14.29

4.2.8. Validation

The case study aims to demonstrate the capabilities of OpenFOAM to replicate mangrove-induced wave attenuation for real coasts. Since no measurements on the actual attenuation are available, the accuracy of the simulations can not be validated. The model can, however, be compared to the analytical wave attenuation. By rewriting Equation (2.11) for β, the following formula is obtained.

$$\tilde{\beta} = \frac{1}{3\sqrt{\pi}} \tilde{C}_D b_v N H_{\text{rms},0} k \frac{\sinh^3 kh + 3\sinh kh}{(\sinh 2kh + 2kh)\sinh kh} \tag{4.1}$$

Using the analytical formulation for the wave attenuation, in combination with local hydrodynamic parameters at each point, the mangrove-induced wave attenuation can be calculated along the first mangrove zone as shown in Figure 5.19. The total attenuation at each point is subtracted from the unvegetated case to account for bathymetry effects and numerical damping to have a good comparison to the

modelled mangrove-induced attenuation. The Python implementation to arrive at these wave heights can be found in Appendix J.

4.2.9. Sensitivity analysis

To gain a better understanding of the performance of the OpenFOAM model, a sensitivity analysis will be performed. This analysis involves a series of model runs in which only one parameter is varied at a time while all other parameters remain consistent with the base case. The goal of this sensitivity analysis is to obtain a better understanding of the influence of individual parameters on the overall model outcome. This helps in highlighting the most influential parameters and understanding the model's uncertainties. The parameters selected for analysis, along with their respective ranges, are summarised in the Table 4.7. The total added wave attenuation by the mangroves will be calculated in order to compare the results of different runs. This is calculated by taking the difference between the vegetated and unvegetated runs as a percentage of the incoming wave height. This allows comparison between scenarios of different wave heights and water levels as well.

by calculating the difference in wave height at the last measurement point of the original model run compared to the sensitivity run.

Varying water levels

Using the current selected hydrodynamic parameters results in waves in intermediate water over the length of the transect, with negligible bottom influence. To test the model for cases where such bottom influences are larger, two runs with lower water levels are created. The first run uses a water level of 3.09 meters, a decrease of 0.5 m. The second scenario uses a water level of 2.09 for even more shallow waves. These water levels, with respect to the Rhizophora parameterisation, are shown in Figure 4.10. Since factors such as shoaling and wave breaking also differ drastically with changing water levels, both scenarios are modelled, both forested and unforested, to find the influence of mangroves in these cases.

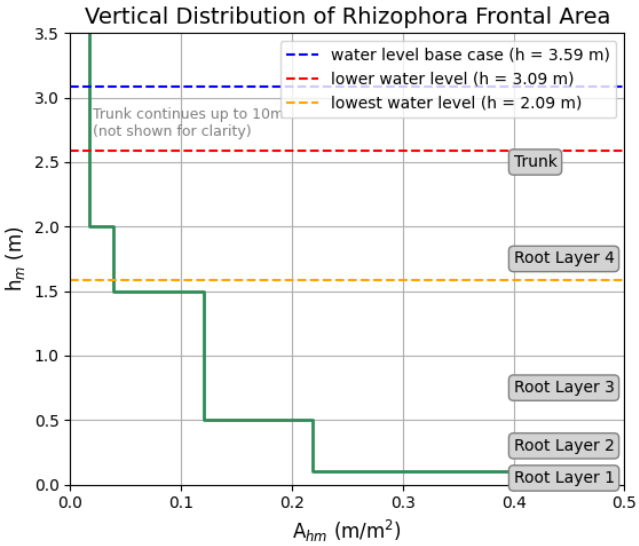

Figure 4.10: Different water levels used for the sensitivity analysis, shown in reference to the Rhizophora in an area where the bathymetry has a height of 0.5 m +SHD

Increased wave height

The waves with a significant wave height of 0.49 meters are currently the maximum expected wave heights in this system, with an expected return period of 1:10.000 years. It is, however, still interesting to see how this model would perform with higher waves. Testing for smaller waves is not possible with this setup, since the grid performance can not be guaranteed for smaller waves. To model higher waves, similar steps are followed as in Section 4.2.4. The significant wave height is now increased by 20 centimetres, Hs = 0.69. Wave steepness for H_s is kept constant by changing Tp. For the base run

with H_s = 0.49, the wavelength at the beginning of the model is 12.15 m, resulting in a steepness of 0.040. With a T_p of 3.1 seconds and the increased wave height of 0.69 m, the steepness remains 0.040 with a wave length of 14.72 meters. All other steps and settings remain the same. This simulation is then run for both with and without mangroves to obtain the effect of the mangrove wave attenuation.

Reduced mangrove cover

From the temporal analysis on the Mandai region in Section 3.2.4, it was visible that the mangrove cover in the Mandai area has at times been more sparse compared to now. Recreating these scenarios in the model can give insight into its effect on wave attenuation. Analysing the mangrove extent in a more struggling period reveals that mangrove extent remains more prevalent on high-lying points in the bathymetry. That is, if bathymetry is assumed not to have changed in those times. Since no measurements from that period are available for this study, constant bathymetry is assumed. To recreate the reduced mangrove cover, the water level is used as a guideline, similar to recreating the regular extent. A water level of 1 m is used as a guideline for the front edge of the forest. The landward limit is set at 0.4 m, giving the following representation. The total length of the mangrove cover has now reduced by 71 m to 112 m (Figure 4.11).

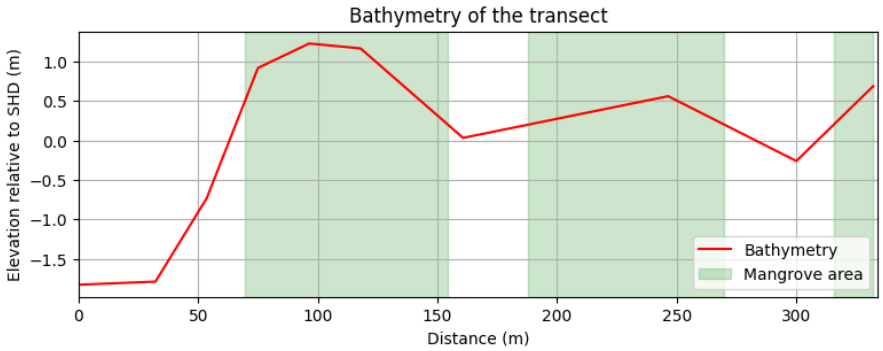

Figure 4.11: Mangrove extend along the transect with reduced mangrove cover

Drag force changes

The base scenario features many assumptions relating to the drag force. These include vegetation parameters such as the tree density and tree frontal area simplifications, but also assumptions on the Bulk drag coefficient, which is set to 1. Since these factors could have significantly different values in the field, the effects of differences in the drag forces should be tested to inspect the influence of possible changes. These can represent a difference in forest density or $\tilde{C}_\mathrm{d}$, for example. It is chosen to test this for an increase in drag force by 1.5 and a decrease by a factor of 1.5.

Avicennia trees

Since the assumption of a species-uniform forest is made, with Rhizophora chosen to represent all mangrove species, the sensitivity of the model to other species should be tested. This is carried out by using the dimensioning of Avicennia as laid out in Section 4.2.5. Differences in the results of this run with the Rhizophora parametrisation will give further insights into the importance of tree species in wave attenuation.

Averaged frontal area

The difference in wave attenuation between a layered approach and a constant averaged frontal area will be tested to inspect the influence of the layered parameterisation. The average frontal area is determined by multiplying the average frontal area for each layer by the layer height and dividing this by the total height of all layers. The layer height of layer 5, the trunk, reaches up to the water level of 3.59 m, combined with an average bathymetry height of 0.54 m, is considered to be submerged for 1.05 m. The average frontal area is thus determined to be 0.0959 m/m^2

Table 4.7: Sensitivity analysis Runs and Conditions for the case study model

Run	ESL	Hs	Tp	Forest cover	Other
Base	3.59 m +SHD	0.49 m	2.8 s	183 m	-
Lower water level	3.09 m +SHD	0.49 m	2.8 s	183 m	-
Lowest water level	2.09 m +SHD	0.49 m	2.8 s	183 m	-
Higher waves	3.59 m +SHD	0.69 m	3.8 s	183 m	-
Reduced forest cover	3.59 m +SHD	0.49 m	2.8 s	112 m	-
Increased drag force	3.59 m +SHD	0.49 m	2.8 s	183 m	Cd = 1.5
Decreased drag force	3.59 m +SHD	0.49 m	2.8 s	183 m	Cd = 1 / 1.5
Avicennia	3.59 m +SHD	0.49 m	2.8 s	183 m	Avicennia representation
Averaged frontal area	3.59 m +SHD	0.49 m	2.8 s	183 m	Averaged frontal area

4.3. Assumptions

For the model to simulate the effects of mangroves on wave attenuation, several assumptions must be made. As it is crucial to understand these to interpret the results and their shortcomings, this section aims to elaborate on the significant assumptions of both models.

4.3.1. Turbulence

In 2DV OpenFOAM simulations, the presence of a turbulence closure model is known to overestimate the energy dissipation due to the instability, resulting in exponential growth of the turbulent kinetic energy (Larsen & Fuhrman, 2018). Allowing this in the model would make the results unrepresentative of real scenarios, since much of the energy dissipation would now be due to turbulent losses instead of vegetation drag. This only leaves the option for a laminar turbulence closure in the model

4.3.2. Bottom friction

Dissipation from mangroves is assumed to be much greater than bottom friction. Therefore, the term will be neglected in both the flume and case-study models (Suzuki et al., 2019; Willemsen et al., 2016).

4.3.3. Mangrove parametrisation for Mandai

Several assumptions were necessary to simplify the representation of the mangrove vegetation in Mandai in the model. These assumptions primarily concern the structure, species composition, and data sources used for parameterisation.

- **Single species representation:** The mangrove forest was assumed to consist entirely of Rhizophora species. In reality, as the field survey from Tembusu (2024) highlights, the site consists of a mixed-species mangrove forest. This assumption introduces potential deviations in drag estimation, as different species exhibit varying root geometries and densities.
- **Root parametrisation :** No measurements on root structure are available for the study site. Instead, root parameterisation is derived from measurements from Horstman et al. (2013). These measurements were conducted in Thailand at a similar study site, but may differ from actual characteristics.
- **Trunk parametrisation :** The parametrisation of the trunk layer of the is based on measurement from a single Rhizophora plot. It assumes that this single plot is representative of the whole study area. Such extrapolation neglects spatial variability within the same species.
- **Density uniformity:** The density of the mangrove forest, similarly to the trunk parametrisation, based on a single Rhizophora plot. It is assumed to be uniform over the study area, omitting any density differences and their effects on wave attenuation.
- **Bulk drag coefficient:** Without measurements, calibration on the bulk drag coefficient is unattainable. A conservative approach is used, and $\tilde{C}_d$ is set at a value of 1.
- **Mangrove canopy:** Canopies are not taken into account for this study, and are assumed not to be inundated and provide attenuation.

While these simplifications are necessary to facilitate the mangrove representation in the model, they may impact the reliability of the results. More reliable measurements on the mangroves in the study area would decrease the uncertainty in these predictions.

4.3.4. Hydrodynamics in Mandai

Representing the hydrodynamics in Mandai requires some key assumptions necessary due to limitations in the model and data availability.

- **Wave spectrum:** No information on the wave spectrum at the start of the study area was known. A JONSWAP spectrum with γ = 3.3 is assumed. This spectrum is made for areas with larger fetches and more developed waves, but it gives a conservative estimate.
- **Alongshore uniformity:** To represent a three-dimensional coast with a 2DV model, alongshore uniformity of coast and mangrove parameters is implicitly assumed. However, in reality, there is much variation along the coast at Mandai.
- **Normally incident waves:** With 2DV modelling, waves attacking at an angle can not be simulated. The transect line is determined to have the governing waves attacking straight at the beach, but waves from other wave angles might produce different results than those found in this study.
- **Morphodynamics:** The model does not resolve any morphodynamic changes along the coast. These changes can, over time, or during extreme storms, cause bathymetry changes leading to changes in the hydrodynamics.
- **Bottom friction:** No measurement on bottom roughness, but since dissipation from mangroves is much greater than bottom friction, the term will be neglected (Suzuki et al., 2019; Willemsen et al., 2016).

5
Results

This Chapter focuses on the results from the research. The results section is divided between the two different models. The First section explores the results of the flume experiment, highlighting the insights obtained from it, and analysing the effect of the layered approach. The second section presents the results of the case study and explores the findings from the sensitivity analysis in greater detail.

5.1. Flume experiment

This section presents the results of the flume model simulations. It starts with model calibration, is followed by validation, and ends with the results of the comparison between the layered and depth-averaged approach.

5.1.1. Model calibration

To ensure the flume model accurately represents the hydrodynamics of the experiment, calibration must be done as outlined in Section 4.1.7.

The mesh calibration shows no significant numerical dissipation for all cases. as shown in Figure 5.1, no wave height decrease occurs over the length of the flume. Fluctuations show a more prominent role in the coarser cases. Especially for the coarsest mesh size with dz = 0.97, the model shows unreliable results with wave heights increasing over the length of the mangrove area. The selected mesh size shows small fluctuations, with a slight increase at the end of the flume of 0.6%, but is considered within limits. Since mesh size is most influential for the lowest wave heights, mesh performance only increases for the other hydrodynamic conditions with higher waves.

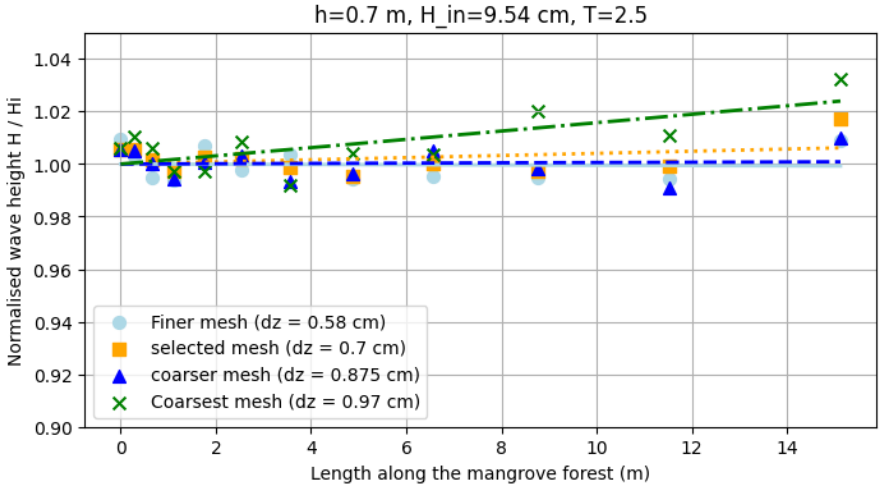

Figure 5.1: Wave heights along the mangrove area in an empty flume for multiple mesh sizes for HC1

The ability to recreate the wave profiles as measured in the experiment is the second step for calibration. The wave profiles of the model results and experimental measurements are compared to inspect the accuracy of the model in generating and propagating these waves in their measured shapes. The measurements for these profiles are taken from the first wave gauge in front of the mangrove forest.

These show great overlap for both the Stokes II-generated waves of WC1 (Figure 5.2), as well as the other wave conditions using Cnoidal wave theory.

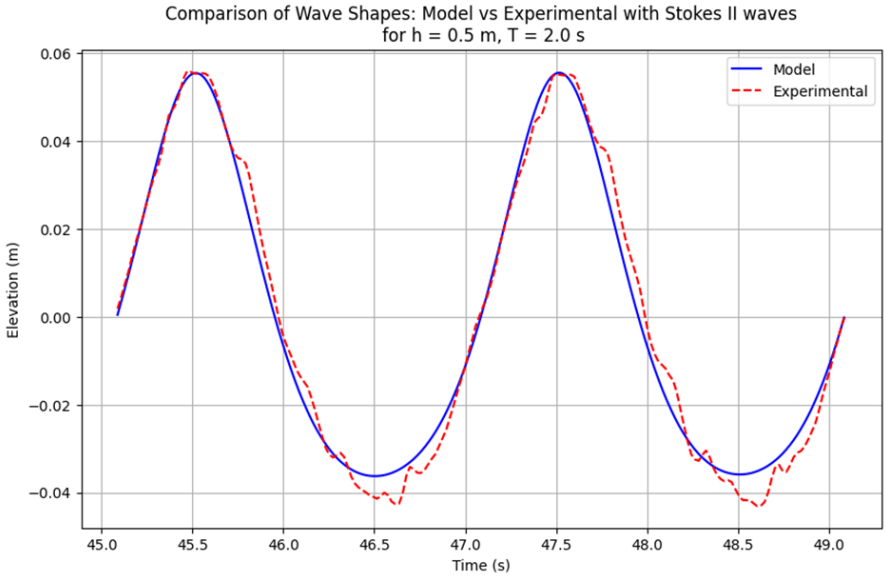

Figure 5.2: Wave profile comparison between model results and experimental measurements for HC1

More complicated wave profiles, such as that of HC4, also show a remarkable similarity with the model. HC4 is the case with the largest skewness of all wave conditions tested. It features the highest waves of all 0.5 m water level conditions, with waves of 10.7 cm. As shown in Figure 5.3, the skewness of the wave is captured with small peaks and long, flat troughs. All other results on the wave profiles can be found in Appendix G.

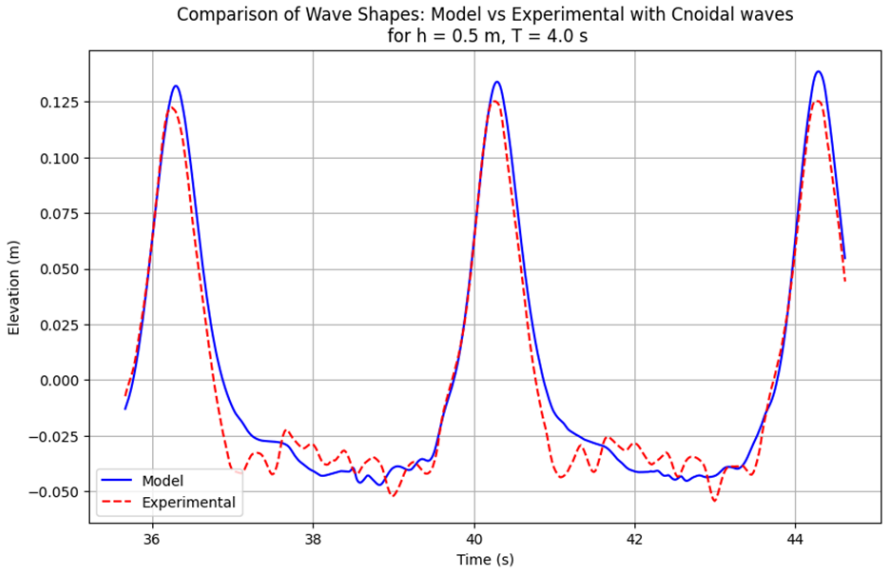

Figure 5.3: Wave profile comparison between model results and experimental measurements for HC4

A comparison of the wave skewness and asymmetry between the model and the experimental measurements, shown in Table 5.1, reveals a good representation of the asymmetry by the model (RMSE = 0.006). Skewness on the other hand is less well represented (RMSE = 0.156). Particularly for the higher waves in the low water level (h=0.5 m), the skewness is overrepresented in the model.

Table 5.1: Comparison of experimental and model values for wave skewness and asymmetry.

Case	Skewness (Exp)	Skewness (Model)	Asymmetry (Exp)	Asymmetry (Model)
HC1	0.307	0.464	0.109	0.102
HC2	0.590	0.630	0.128	0.118
HC3	0.558	0.872	0.089	0.082
HC4	1.261	1.434	0.105	0.102
HC5	0.363	0.375	0.112	0.111
HC6	0.401	0.521	0.108	0.107
HC7	0.404	0.416	0.087	0.089

5.1.2. Bulk drag force calibration

Calibration on the bulk drag coefficient is done according to Section 4.1.8.
By iterating with both the incoming wave height and the $\tilde{C}_d$ value, the values for the incoming wave height and β have been replicated in the model. Figure 5.4 shows the calibrated flume model for HC4. It shows a similar trend, with a β from the model of 10.23, compared to 0.1028 from the experimental values. The collection of all results can be found in Appendix H.

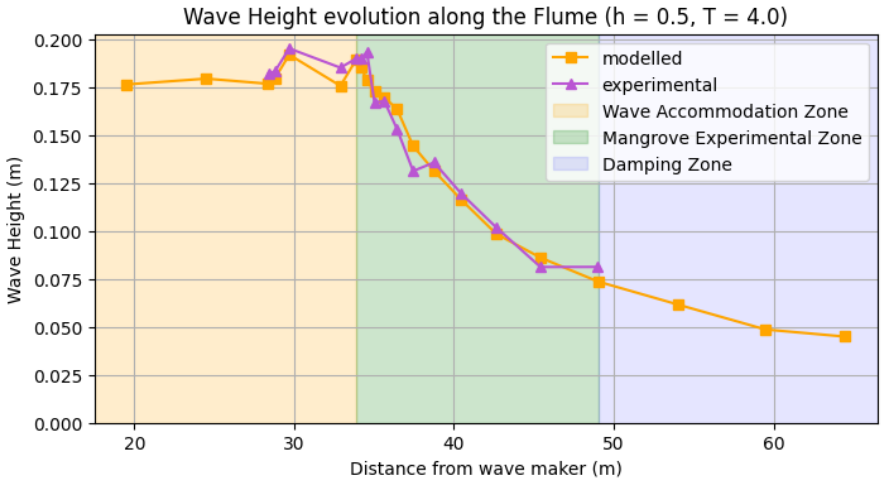

Figure 5.4: Wave height evolution of the flume measurements vs model results after calibration along the whole flume for HC4

5.1.3. Validation

As proposed in Section 4.1.9, the validation of the flume model follows from two parts. The replication of the wave height evolution along the flume, and the correlation of the obtained Bulk drag coefficients with the Keulegan-Carpenter number. For all 7 hydrodynamic conditions, the bulk drag coefficient and wave height have been calibrated to fit the β value as well as the incoming wave heights along the mangrove area, as described in Section 4.1.8. This section explores the results from these calibrations.

Wave height evolution

Showing the wave height evolution gives an insight into the capabilities of the model to replicate flume scenarios, given the correct input values.

Figure 5.4 and Figure 5.5 show the wave height evolution for the calibrated model compared to the experimental measurements. The model is calibrated on the experimental zone. This area shows the wave attenuation as a result of the mangroves. The area shows observable deviations between individual measurements, but a clear agreement in trend.

In the transition from the wave accommodation zone to the experimental mangrove zone, an increase in wave height compared to the original wave height used as input. This is likely due to the resistance force from the mangroves. This is also considered to be the cause for the high fluctuation in wave

heights from the gauges in front of the mangroves in the wave accommodation zone. The resistance causes partial reflection, resulting in interference.

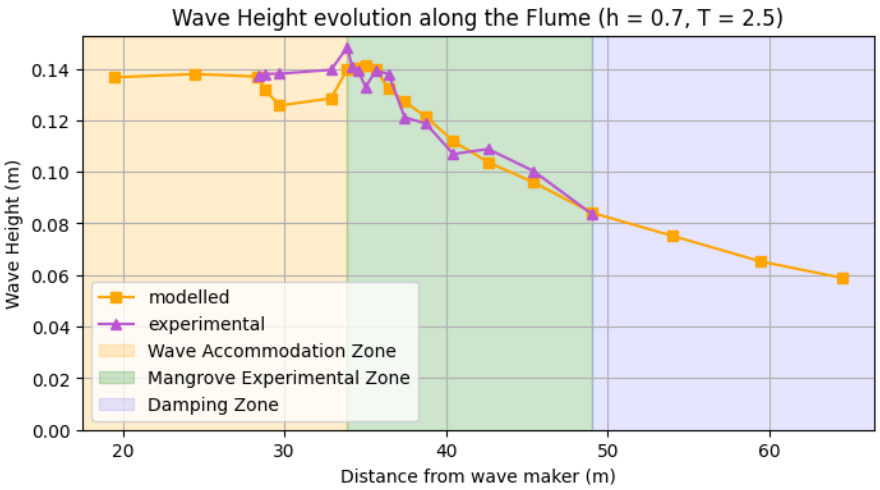

Figure 5.5: Wave height evolution of the model findings vs the flume measurements along the whole flume for HC5

The damping zone is exclusively used in the model, and not in the physical experiment, to limit the effect of reflection, as outlined in Section 4.1.4. It shows the wave height decreasing further over the length of the model, limiting the damping.

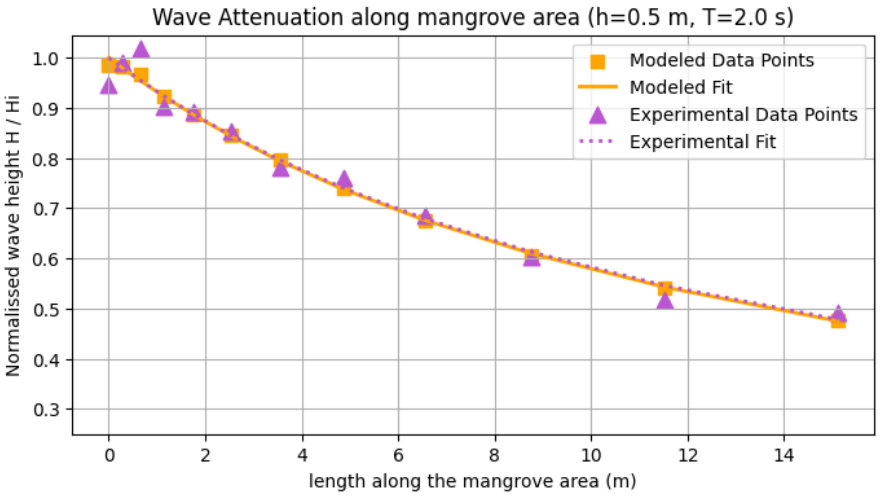

Figure 5.6: Comparison of model finding vs experiment measurements along the experimental mangrove zone for HC1

Focusing exclusively on the experimental mangrove zone allows for a better analysis of the modelled wave attenuation (Figure 5.6. For both the model and the experimental data, the wave attenuation is fitted along this 15.12-meter area. The modelled attenuation shows excellent agreement in the attenuation trend with the experiment. Both cases show deviations from the trend line, with the model result having a lower Root Mean Squared Error (RMSE) compared to the experiment (Table 5.2). On average, 0.00284 m vs 0.00391, respectively.

Calibrated bulk drag coefficients

Following the calibration, the obtained $\tilde{C}_d$ values, their analytical counterpart and the corresponding KC numbers for each hydrodynamic condition are shown in Table 5.3. Since the hydrodynamic conditions are the same for the experimental and model cases, KC numbers are also equal. There is, however, a big difference between the $\tilde{C}_d$ values. Iteratively obtained $\tilde{C}_d$ values have a higher value

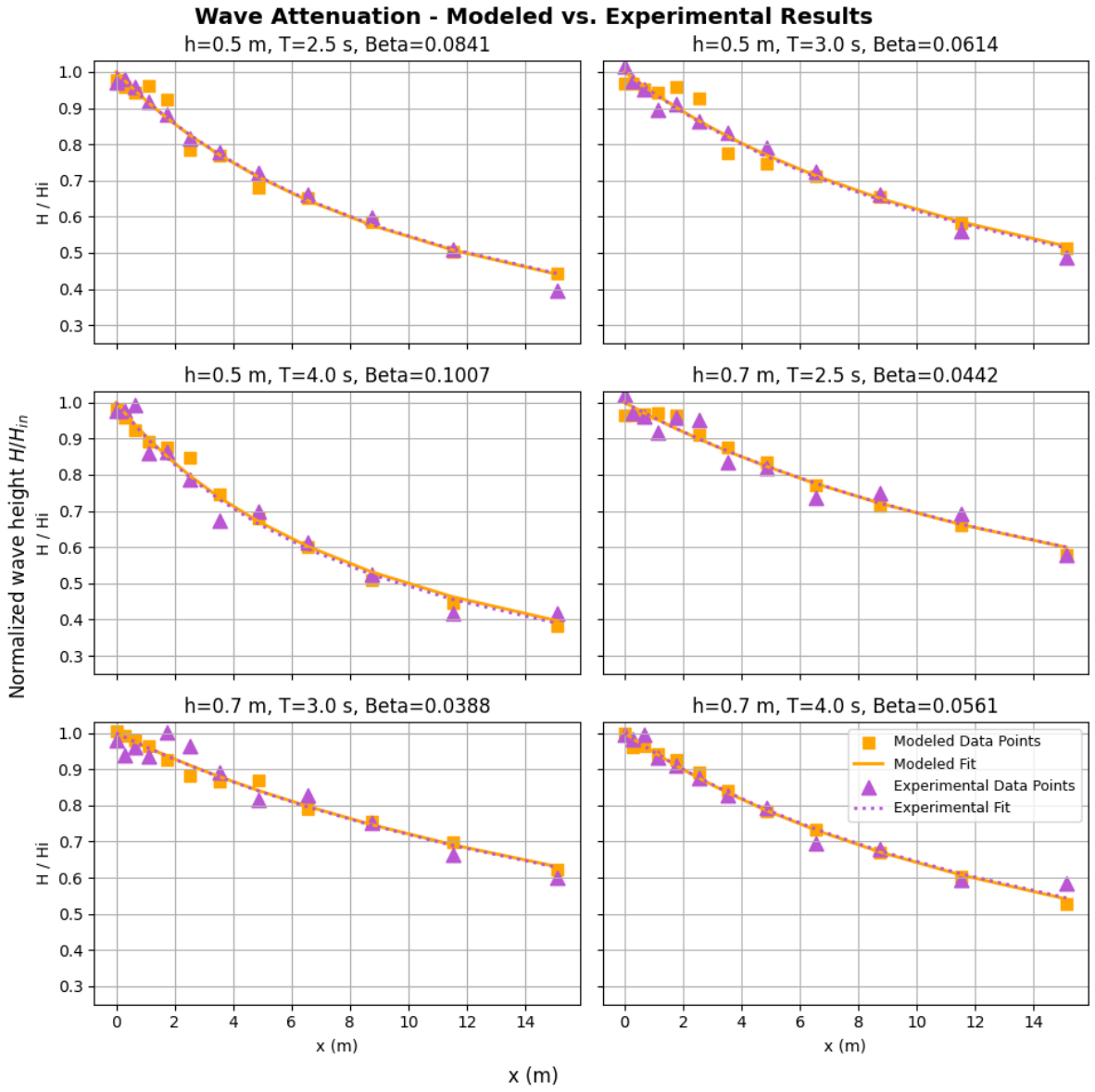

Figure 5.7: Calibrations for the other 6 wave conditions compared to the measurements from the experiment. Figure shows wave height evolutions along the mangrove area.

Table 5.2: Comparison of β values and RMSE for Experiment and Model

HC	β Experiment (m^{-1})	β Model (m^{-1})	Diff. β (%)	RMSE Experiment (m)	RMSE Model (m)
1	0.0722	0.0731	1.30	0.0030	0.0007
2	0.0834	0.0841	0.84	0.0030	0.0043
3	0.0627	0.0614	1.98	0.0027	0.0044
4	0.1038	0.1007	2.92	0.0062	0.0040
5	0.0440	0.0442	0.34	0.0043	0.0028
6	0.0392	0.0388	0.94	0.0049	0.0020
7	0.0553	0.0561	1.32	0.0033	0.0017

for all hydrodynamic conditions than those found with the analytical approach from the experimental measurements. The amount of difference varies between different conditions, ranging from 0.02 for HC3 to 0.63 for HC4. Larger calibrated bulk drag coefficients also show a more significant difference in $\tilde{C}_d$ with their analytical counterparts.

Table 5.3: Comparison of Calibrated and Analytical Drag Coefficients with KC Values

HC	Calibrated Cd	Analytical Cd	KC
1	1.95	1.51	24.85
2	1.58	1.31	45.35
3	1.25	1.23	49.57
4	1.75	1.12	91.77
5	1.67	1.35	36.88
6	1.53	1.10	43.24
7	1.89	1.37	68.49

Determining the correlation for both cases can give insight into the performance of the model. Figure 5.8 shows, contrary to the hypothesised result, that the correlation between $\tilde{C}_d$ and KC obtained from the model is worse than that of the experimental results. The $\tilde{C}_d$ obtained from the model has an R^2 value of 0.010, showing a weak correlation. The R^2 value of the model output is higher, 0.437. This is still not considered a strong correlation, but significantly higher than that of the modelled outcomes.

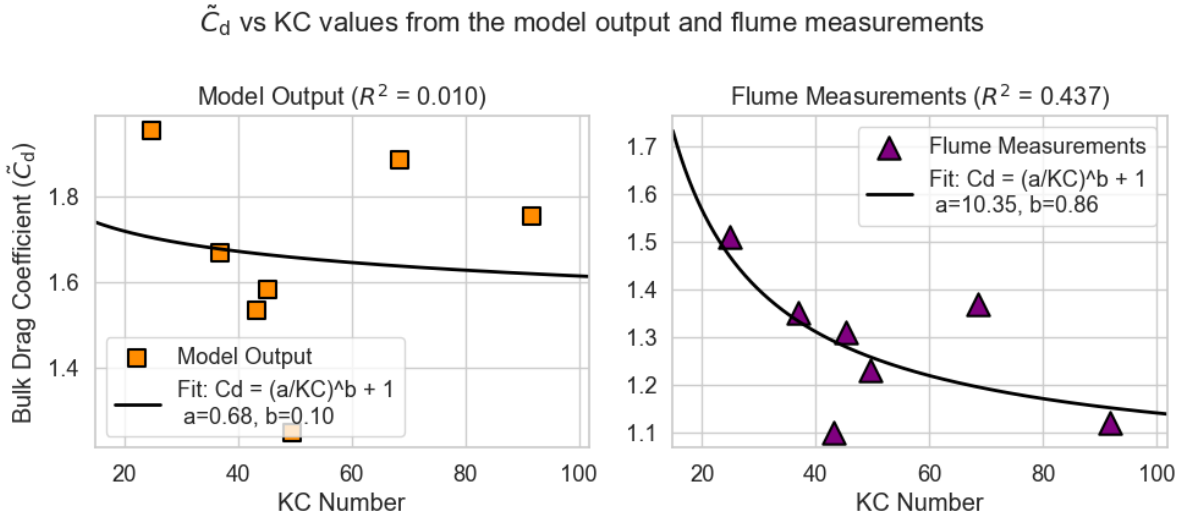

Figure 5.8: Correlation between $\tilde{C}_d$ and KC for both the iterated model values and the analytical formulation

To provide cross-validation and provide a larger reference frame for the $\tilde{C}_d$ values and their relation to KC, these can be compared to values found in other studies. Figure 5.9 shows this comparison to the studies of Kelty et al. (2022), Lopez-Arias et al. (2024), and Maza et al. (2019). It shows a good fit of the analytically determined $\tilde{C}_d$ values, comparable to that of the other studies. The results of the iteratively

found $\tilde{C}_d$ show less agreement with the other results. For all KC numbers, the bulk drag coefficient exceeds the fitted curve.

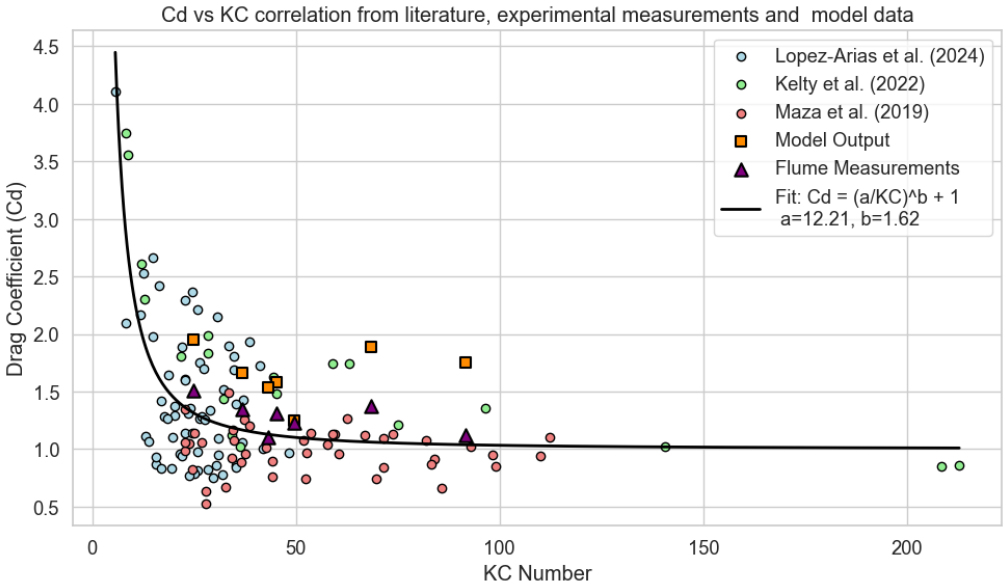

Figure 5.9: Comparison of the $\tilde{C}_d$-KC values to other experimental data of Lopez-Arias et al. (2024), Kelty et al. (2022) and Maza et al. (2019). Adapted from Lopez-Arias et al. (2024).

5.1.4. Layered approach

Following Section 4.1.10, the comparison between the layered approach and a depth-averaged approach is carried out, displayed in Figure 5.10.

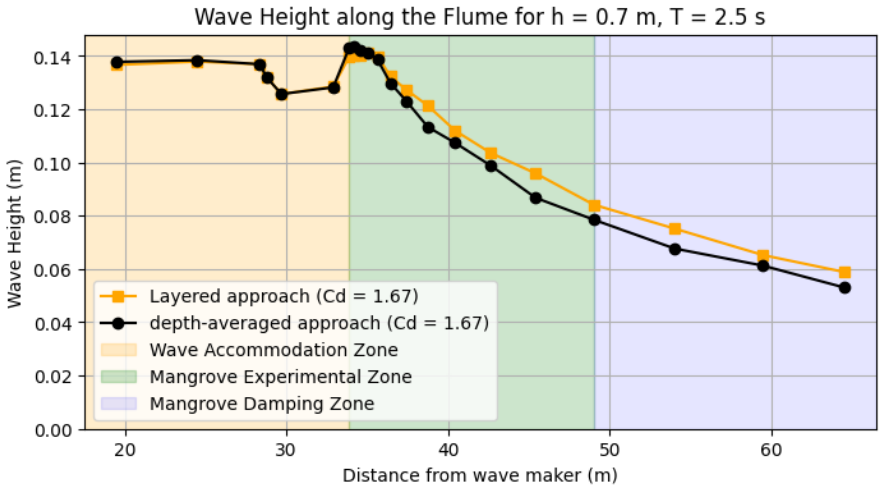

Figure 5.10: Modelled wave heights over the full length of the flume for the layered approach and the depth-averaged approach for WC5 using $\tilde{C}_d$ = 1.67 for both approaches

In the mangrove area, a difference in attenuation rate between the two methods is observable. Despite having the same submerged frontal area, the attenuation rate of the depth-averaged frontal area is 30.1% higher than that of the layered approach.

This overestimation raises the question of what the attenuation capacity of the depth-averaged frontal area approach is when the value of $\tilde{C}_d$ is the analytically determined 1.35 instead of the iteratively found 1.75 (using the layered approach). This shows a relatively similar result to the layered approach with calibrated $\tilde{C}_d$, and thus the experimental results.

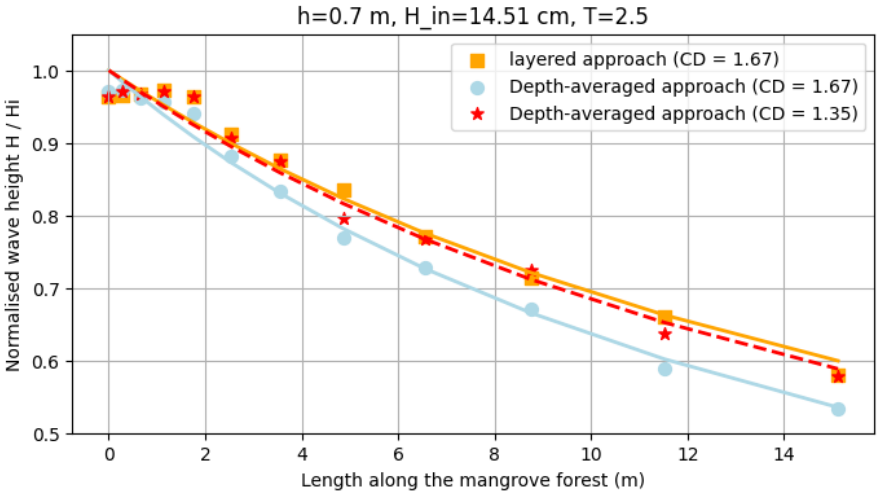

Figure 5.11: Comparison of the wave heights along the mangrove zone for layered approach (with calibrated $\tilde{C}_d$) and the depth averaged frontal area (with the analytical and calibrated $\tilde{C}_d$)

Table 5.4 displays the beta values for these runs. Similar to the calibration of the bulk drag coefficient for the layered approach, $\tilde{C}_d$ is calibrated for the depth-averaged approach. This reveals a value of 1.23, much closer to the analytically determined 1.35.

Input	β value
Experimental measurements	0.0440
Layered approach ($\tilde{C}_d$) = 1.67	0.0442
Depth-averaged frontal area ($\tilde{C}_d$ = 1.23)	0.0441
Depth-averaged frontal area ($\tilde{C}_d$ = 1.35)	0.0463
Depth-averaged frontal area ($\tilde{C}_d$ = 1.67)	0.0574

Table 5.4: Beta values of the different fitted curves with HC5

Velocity profiles

The analysis on velocity profiles, as stated in Section 4.1.10, was carried out using both approaches with their own calibrated bulk drag coefficient, fitted to the experimental results, to ensure similar absolute vertical velocities (Figure 5.12.

Inside the mangrove zone, at x = 45 m, the influence of the approaches is apparent. The depth-averaged method produces a recognisable and relatively smooth velocity profile, whereas the layered approach exhibits a more irregular profile. This irregularity is characterised by distinct variations in velocity that correspond to the transitions between mangrove layers. As the frontal area increases lower in the flume, so do the corresponding drag forces. And layers with higher drag forces exhibit lower velocities. This leads to extra step-wise decreases in absolute velocity, on top of a smoother decrease also visible in the depth average approach.

In front of the experimental mangrove zone, the depth-averaged approach shows a notably higher negative orbital velocity at the top of the water column. This might be due to reflection being stronger in that area for the depth-averaged approach, compared to the layered approach, where the higher layers apply the lowest amount of drag.

Despite having significantly different drag factors, the average flow velocities in the mangrove zone are comparable. This is expected since both cases show the same total wave attenuation.

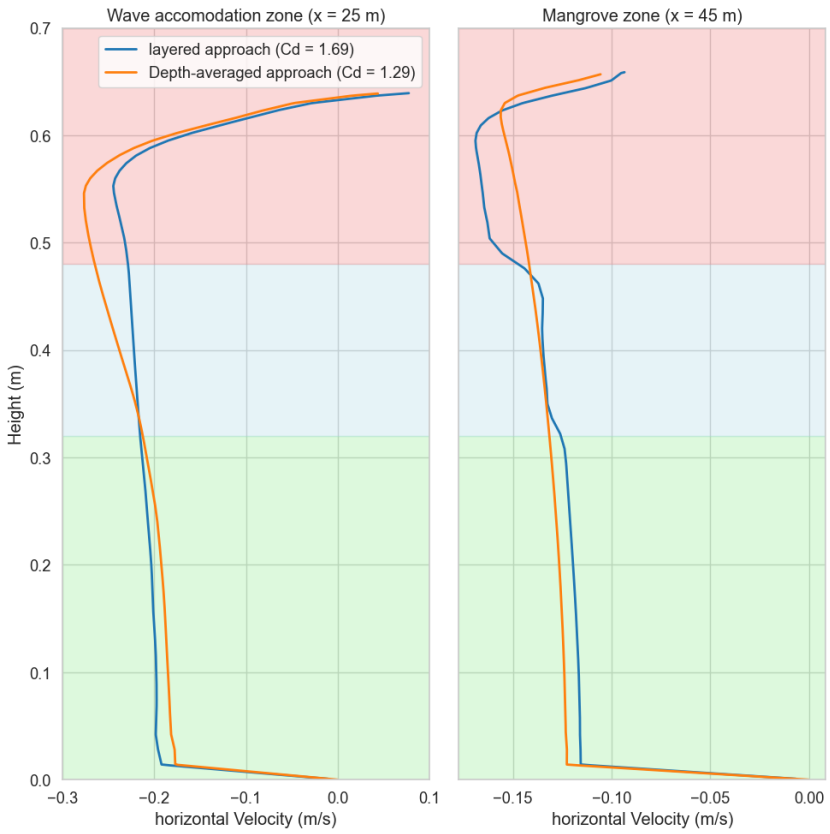

Figure 5.12: Comparison of the velocity profiles of the layered approach with $\tilde{C}_d$ = 1.67 and the depth-averaged approach with $\tilde{C}_d$ = 1.29. The location is at 45 meters, towards the end of the mangrove zone, at a moment of maximum negative velocity. The plots show the multiple root layers as used in the layered approach.

5.2. Case study

This section lays out the results from the case study, starting with the calibration. This is followed by the results of the base case and the sensitivity analysis. Lastly, the comparison between the modelled and analytical attenuation is shown.

5.2.1. Calibration

As presented in Section 4.2.7, calibration on the case study is performed for three different meshes for the base case with mangroves as shown in Figure 5.13 this is the regular case without any of the additions of the sensitivity analysis, but with mangroves. The base case plot without mangroves is added as a reference in the figure.

The coarsest mesh, dz = 7.5 cm, exhibits a large deviation from the other two meshes, starting right at the beginning and growing further along the length of the transect, resulting in a significant 27% less than that of the selected mesh. The intermediate mesh, dz = 6.25 cm, shows a smaller deviation. Especially at the beginning, just before reaching the forest, the wave heights of both meshes show similar results. After 70 meters, significant deviations are observable, which grow increasingly larger over the length of the transect, resulting in a difference of 11% at the end. This suggests that at the start, with significant wave heights above 38 cm, the mesh performance of both meshes is adequate. But as wave heights decrease over the length of the flume due to breaking and attenuation from mangroves, the mesh becomes less reliable and significant numerical damping interferes with obtaining reliable results.

5.2.2. Base case

The Base case, without the presence of mangroves, displayed in Figure 5.14, shows a significant reduction in wave height over the length of the flume. The wave height reduces to 25.6 cm, a deduction

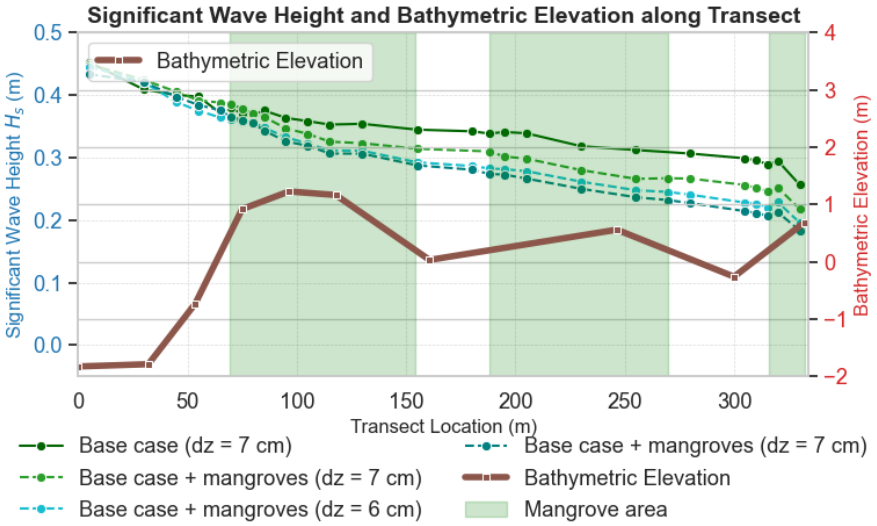

Figure 5.13: Mesh calibration for the base case of the case study model with mangroves. mesh sizes are: dz = 5 cm, dx = 10 cm (selected mesh), dz = 6.25 cm & dx = 12.5 cm and dz = 7.5 cm & dx = 15 cm

of 43% compared to the starting wave height. The measurement at the first wave gauge also shows a deviation from the original wave height, measuring 45.3 cm instead of 49 cm.

The influence of bathymetry on wave transformation appears limited. Minor shoaling is observed around 70 meters, followed by a small amount of breaking. At the end of the transect, the steep decline in wave height also signifies some breaking as a result of the steeper increase in bathymetry.

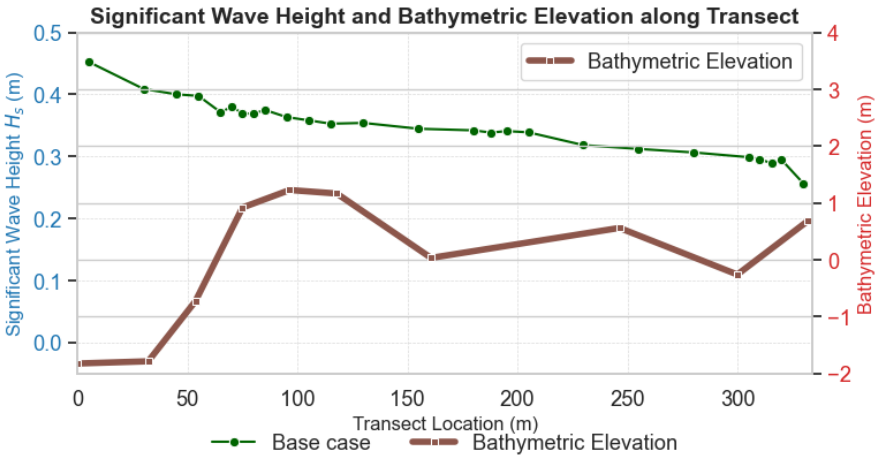

Figure 5.14: Significant wave height evolution along the transect for the base case with no mangroves present

Introducing mangroves to the system, shown in Figure 5.15, results in additional wave attenuation due to the added drag force. The total added wave attenuation by the mangroves, calculated as the difference in wave height between the vegetated and unvegetated simulations as a percentage of the incoming wave height increases along the transect. Especially in the first mangrove zone, the attenuation is apparent. Interestingly, after the first mangrove zone, the added attenuation from the mangroves decreases as the total attenuation only increases slightly. The shape of the added attenuation in the mangrove areas also follows the same shape observed in the flume section with a steep decline in the beginning, flattening out further along the forested area. The total added attenuation of mangroves is 8.8% for the last wave gauge.

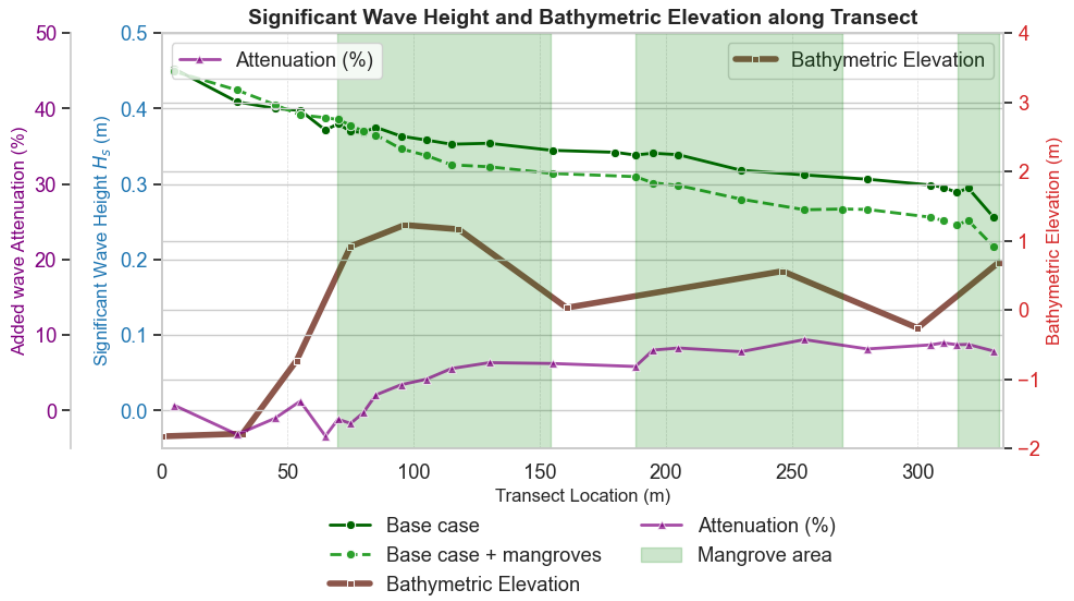

Figure 5.15: Significant wave height evolution along the transect for the base case with and without mangroves. The bottom line shows the difference in wave height, highlighting the influence of the mangroves.

5.2.3. Sensitivity analysis

In the sensitivity analysis, the different sensitivity runs as proposed in Section 4.2.9 are reported on. A full overview of the reductions in the significant wave heights for all scenarios, both with and without mangroves, as well as the added attenuation for all of the mangrove is shown in Table 5.5. All plots for the sensitivity analysis can be found in Appendix I.

Table 5.5: Significant wave height reduction for all scenarios. The added attenuation column shows the percentage increase in wave height reduction compared to the unvegetated base scenario.

Category	Scenario	H_s Reduction (%)	Added Attenuation (%)
unvegetated	base	-43.4	–
	lower water level (h = 3.09 m)	-40.3	–
	lowest water level (h = 2.09 m)	-49.9	–
	increased wave height (H_s = 0.69 m)	-30.2	–
vegetated	base	-51.6	8.8
	lower water level (h = 3.09 m)	-52.5	10.8
	lowest water level (h = 2.09 m)	-66.5	17.1
	increased wave height (H_s = 0.69 m)	-46.4	16.6
	reduced mangrove cover (112 m)	-49.3	6.4
	decreased drag force ($\tilde{C}$d $\div$1.5)	-48.9	6.1
	increased drag force ($\tilde{C}$d$\times$1.5)	-54.8	12.1
	Avicennia parametrisation	-47.1	5.3
	averaged frontal area	-61.7	19.2

Decreased water level

Figure 5.16 illustrates the impact of lower water level where h = 3.09 m (blue), the lowest water level where h = 2.09 m (red) and the base case where h = 3.59 m (green). For the moderate reduction (3.09 m), the total wave height reduction remains similar for both vegetated and unvegetated runs, suggesting minimal influence from water depth. However, the vegetated run shows slightly higher attenuation, resulting in an added attenuation of 10.8%.

In contrast, the lowest water level, h = 2.09, shows a stronger bottom influence. At the start of the first mangrove zone, wave breaking occurs, resulting in a reduction of 39.8% for the non-vegetated run and

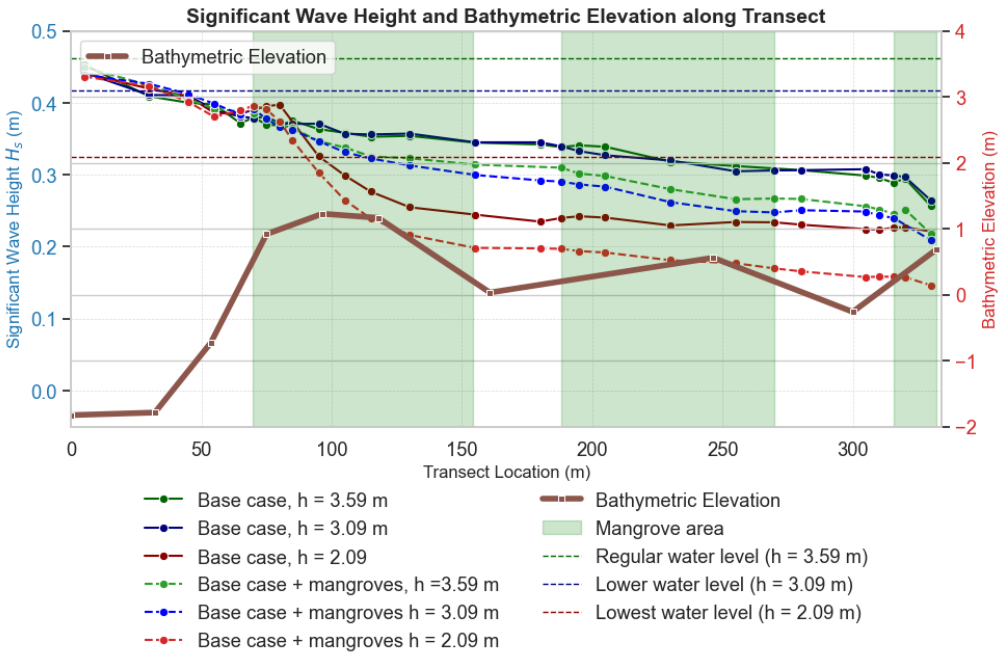

Figure 5.16: Significant wave height evolution along the transect with two reduced water levels (h = 3.09 m and h = 2.09), compared with the regular water level (h = 3.59 m). All scenarios are shown with and without mangroves.

50.1% for the mangrove run. The total reductions in wave height, compared to the first gauge measurements, are 48.9% and 66.5% for the non-vegetated and vegetated runs, respectively. Resulting in a total added attenuation of the mangroves of 17.1%.

Increased wave height

Figure 5.17 compares the changes in wave height between the base case (H_s = 0.49 m) and the increased wave height case (H_s = 0.69 m). All significant wave heights are normalised by dividing them by the measurements from the first wave gauge.
For the case without mangroves, significantly less decline over the length of the transect, with a total decrease of 30.2% compared to 43,4% for the base case. This further supports a large influence of numerical damping for the regular cases where H_s = 0.49 m, as larger wave heights experience less numerical damping.
The final normalised wave height for the mangrove case with increased wave heights is higher than that of the regular wave height scenario with mangroves, but the added attenuation of the mangroves is almost double that of the base case, with 19.2%.

Reduced mangrove cover

The reduction in mangrove cover from 183 m to 112 m shows clear differences in attenuation between the mangrove-induced wave attenuation in the mangrove areas, as the attenuation starts earlier for the fully vegetated scenario. The total added attenuation is 6.4%, a decrease of 27% compared to the base case.

Drag force changes

The final reduction compared to the base case reveals a total reduction in wave height of 3.1 cm, 4.3 cm and 5.7 cm for $\tilde{C}_d$ = 0.66, 1 and 1.5, each step having an increase of 50%. The added attenuations are 6.1%, 8.8% and 12.1%.

Avicennia trees

The Avicennia-based parametrisation results in lower wave attenuation compared to the Rhizophora-based base case. The added attenuation is 5.3%, almost half that of the base scenario.

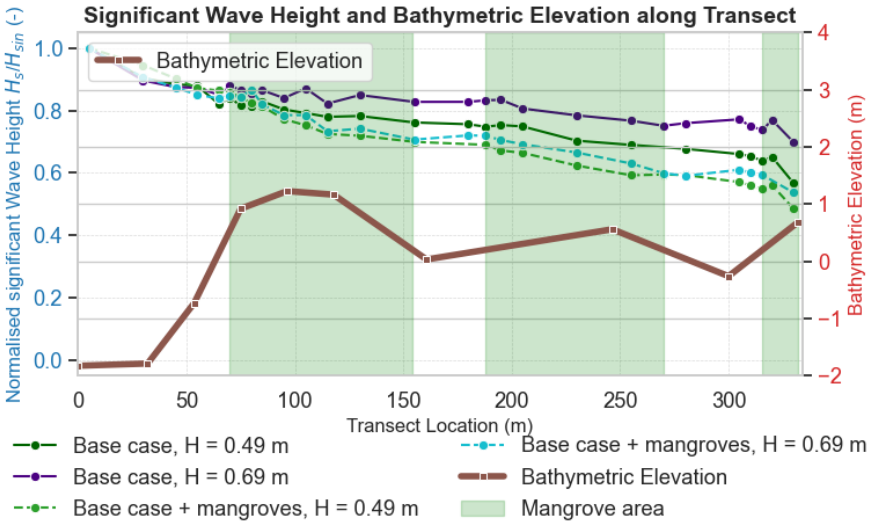

Figure 5.17: Significant wave height evolution along the transect with increased wave height (H_s = 0.69 m, T_p = 3.1 s). Shown for both with and without mangroves

Depth-averaged frontal area

Figure 5.18 compares the layered and depth-averaged frontal area approaches. The run using a depth-frontal area shows a much higher attenuation rate than the base scenario with mangroves. This results in an added attenuation of 19.2%, almost twice as high as that of the base case.

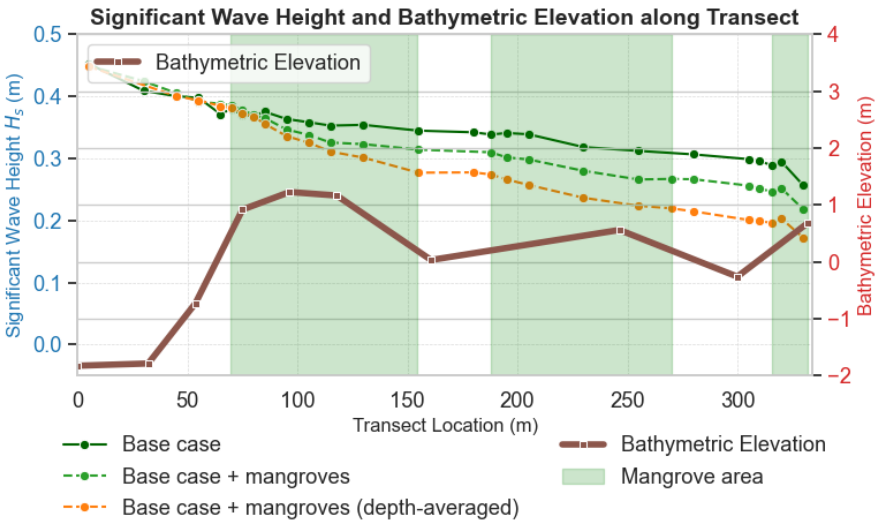

Figure 5.18: Wave height evolution along the first mangrove zone, showing the difference between the depth-averaged approach and the layered approach

5.2.4. Comparison to the analytical attenuation

Figure 5.19 shows the attenuation along the first mangrove zone for the model outcome of the base case, as well as the analytical attenuation determined according to Section 2.2.2. The analytical attenuation shows a good fit with the model outcomes. Where the analytical attenuation shows a reduction to 31.4 cm, the model outcome shows a reduction to 30.3 cm, a difference of 2.2% of the wave height This is more than twice as large as that of the numerical model.

Comparing this analytical wave attenuation to the modelled attenuation for higher waves generally shows a good overlap as well, as seen in Figure 5.20. The final wave heights are 44.4 cm for the model and 46.4 cm for the analytical attenuation, a difference of 3.0% of the wave height.

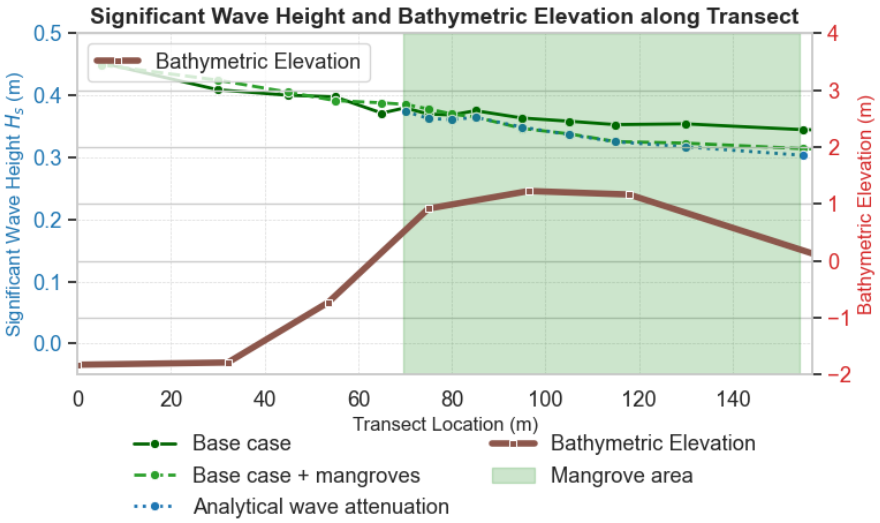

Figure 5.19: Wave height evolution along the first mangrove zone, showing the difference between the attenuation of the numerical mangrove implementation and the analytical approach. For the base case with mangroves

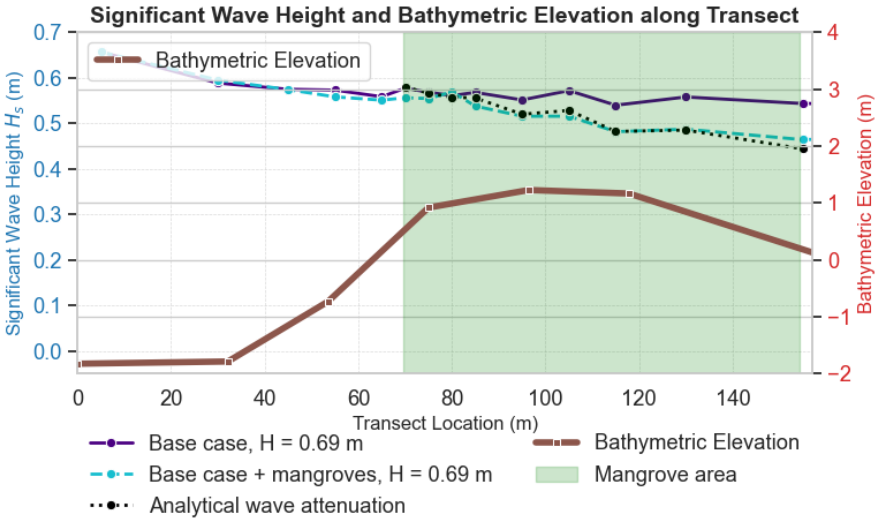

Figure 5.20: Wave height evolution along the first mangrove zone, showing the difference between the attenuation of the numerical mangrove implementation and the analytical approach. For increased wave heights (H_s = 0.69 m, T_p = 3.1 s)

6
Discussion

This chapter discusses and contextualises the findings from the previous chapter. First, the flume model is examined, followed by the case study model. In the end, the limitations of the study are reviewed.

6.1. Flume

The results obtained from the flume models provide valuable insights into the capability of 2DV RANS models to replicate wave attenuation from mangroves. The ability to compare model results to real-world measurements in a controlled environment allows for direct comparison with physical measurements, offering a reliable basis to evaluate model performance under various hydrodynamic conditions. This also enables the identification of both the strengths and limitations of the numerical model.

6.1.1. Calibration

The calibrations demonstrate that the model can replicate the experimental measurements reliably and highlight its capability in replication through calibration. Mesh calibration confirmed that the selected mesh (dz = 0.7 cm, dx = 2.1 cm) provides a reliable balance between computational efficiency and numerical stability. While no meshes showed any observable numerical dissipation within the experimental domain, coarser meshes showed significant deviations, unsuitable for this study.

The calibration of wave profiles, evaluated in front of the mangrove area, demonstrated good agreement between the modelled and measured wave shapes. The ability to replicate both Stokes waves and Cnoidal profiles confirms the robustness of the wave generation in the model. This supports the use of the model for representing a wide range of wave conditions relevant for coastal mangrove systems.

6.1.2. Wave height evolution

After calibrating the bulk drag coefficient, the model showed strong agreement in attenuation trends with the experimental measurements. All β values were calibrated to within at least 97% agreement with the experimental β values. Both the model and the experimental results showed minor deviations of individual wave gauges from the trend attenuation line, with average RMSE values of 0.00284 m and 0.00391, respectively. Several factors may contribute to these discrepancies. Despite efforts to minimise wave reflection, through a dissipative beach in the experiment and a damping zone in the model, residual reflections may still influence the results. As noted by Maza, Lara, Losada, et al. (2015), reflection, especially for regular waves, can significantly affect the results. Additionally, internal reflection in the mangrove zone, caused by individual mangroves for the physical experiment, or by the drag force in the model, may introduce local interference. Sensor inaccuracies in the physical setup, as well as limitations in free surface resolution in the numerical model, may further contribute to the observed deviations.

6.1.3. Calibrated bulk drag coefficients

The hypothesis stated that calibrated $\tilde{C}$d from the flume model would result in a more realistic representation of the physical processes and thus result in a stronger correlation between $\tilde{C}$d and KC, compared to the same relation with the analytically obtained $\tilde{C}$d This hypothesis was based on two primary assumptions: first, that a layered representation more accurately captures the vertical variations in mangrove frontal area, and second, that a RANS model offers superior accuracy over the analytical method, since it does not rely on the assumptions of linear wave theory.

However, this hypothesis was not supported by the results. The calibrated $\tilde{C}$d values showed a poor

correlation with KC (R^2 = 0.010), whereas the analytically derived values showed a moderately stronger correlation (R^2 = 0.437). This outcome suggests that the added complexity of the RANS model and vertical layering does not necessarily translate into improved predictive power when using KC-based formulations.

To isolate the effect of the numerical model itself, the Flume measurements were compared to a depth-averaged implementation using the analytically derived $\tilde{C}$d. This showed a calibrated bulk drag coefficient for the depth-averaged case being very similar to the analytical $\tilde{C}$d, highlighting only a slight difference between the use of a RANS model and the analytical method when frontal area is assumed constant over depth. This suggests that using linear wave theory as a simplification for the calculation of vegetation-induced wave attenuation can lead to accurate calculations. So, for cases where the frontal area of vegetation can reasonably be assumed uniform over the depth, the analytical approach, despite its generalisations on wave theory, can lead to accurate outcomes.

In contrast, when comparing the layered model to a simplified depth-averaged approach under identical forcing conditions, a more notable difference was observed. The layered model predicted a wave attenuation coefficient (β) that was approximately 29.9% lower. This suggests that the choice of a layered representation significantly influences the modelled wave attenuation, with a considerable reduction of the actual damping.

Traditionally, studies often assume a uniform frontal area distribution or use approximations that effectively depth-average this property. Even in multilayer implementations such as that of Suzuki et al. (2019) and Q. Chen et al. (2021), the calculation of the energy sink is based on the drag of a depth-averaged frontal area. These findings suggest that this assumption can lead to a considerable overestimation of the total attenuation.

The plotted velocity profiles provide further insight into the discrepancy between the two approaches. It found a significant influence of the depth-varying drag force on the velocity profile. As drag forces increase towards the bottom of the flume due to larger frontal areas, the velocity decreases. This change in velocity profile shows higher velocities in low-drag areas and lower velocities in high-drag areas. Due to the quadratic relationship between the flow velocity, this results in a lower amount of total drag. These non-linear effects in the velocity profile are not found in the analytical formulation, where the damping coefficient β is linearly related to the frontal area and drag force. The results suggest that this may be an oversimplification, as variations in the velocity profile can lead to deviations from this expected relationship, especially for thicker forest covers and mangroves with denser root structures.

6.2. Case study

This section discusses the results obtained from the case study model. Elaborating further on the findings obtained through the model and sensitivity analysis, and putting the results in a larger frame by comparing it to findings from the literature study.

6.2.1. Calibration

The calibration of the case study reveals a significant influence of numerical camping on the model outcomes. The selected mesh (dz = 5 cm) showed notable differences with the larger meshes. The mesh fineness is restricted by the maximum computational availability, with maximum runtimes up to 24 hours with 64 cores. Given the substantial difference between mesh results, the difference in wave decay between the current mesh and a suitable mesh is likely to be significant. The difference between the empty base case and the increased wave height scenario further supports this. With no mangrove-induced attenuation present, the case with higher waves shows only a decrease in wave height of 30.2% along the transect, compared to 43.4% for the base case. This indicates that numerical processes, rather than physical processes, are likely responsible for most of the wave height reduction for the empty scenarios, and also play a large role in the forested scenarios. Especially since, as the mangroves reduce the wave heights, numerical dissipation is further increased due to the smaller waves. No other forms of energy dissipation are present that could explain this decrease in wave height, as bottom friction is neglected and a laminar turbulence closure is used. As a result, quantitative analysis on the wave attenuation carried out by mangroves is unfortunately restricted. Qualitative analysis will thus be used to inspect the influence of different parameters on the wave attenuation.

6.2.2. Wave breaking and depth influences

Across all cases, results show a large decrease in significant wave height measured by the first wave gauge compared to the significant wave height used as input. With a depth of 5.4 m and the relatively small waves, this is unlikely to be a result of depth-induced breaking. Sensitivity runs, with larger waves and lower water levels showing similar levels of decrease, further confirm this, since both runs would show more depth-induced breaking as a result of higher wave heights or shallower water.

This would suggest that it might be due to steepness-induced breaking, also called whitecapping. The incoming generated waves are likely unstable, resulting in immediate breaking. This implies a potential error in the approximation of the prescribed wave conditions, as the wave properties assigned do not result in stable waves. Although breaking limits for monochromatic waves, such as that of Miche (1944), are not satisfied, wave-wave interactions between waves of different frequencies can increase steepness, leading to whitecapping (Janssen, 2004).

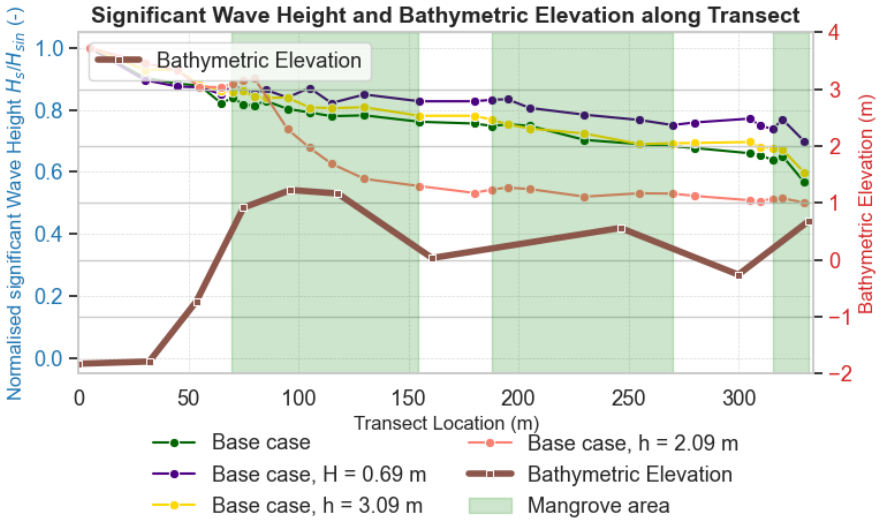

Figure 6.1: Significant wave height evolution along the transect for the base case, lower water level (h = 3.09 m), lowest water level (h = 2.09 m) and increased wave height (H_s = 0.69 m, T_p = 3.1 s), all without mangroves

Depth-induced breaking is, however, clearly evident in the lowest water level scenario (h = 2.09 m). Just before the highest point of the bathymetry, 80 meters along the transect, the water depth reaches 1 meter, and the significant wave height decreases drastically. The breaking index γ (h/H) reaches a value of 0.4, which is consistent with the onset of breaking in irregular waves Bosboom and Stive (2023) and Goda (2010). Interestingly, behind this breaking area, 180 meters along the transect, the wave height remains relatively constant. Based on the large amount of numerical damping in the system, this is odd, as further reduction would be expected.

The other cases generally show little influence of the bathymetry. Ratios of h/L, based on peak period and significant wave height, range between 0.44, 0.41 and 0.31 m at the deepest point, and 0.22, 0.17 and 0.19 m at the most shallow point, for the base case, increased wave height and lower water level, respectively. These values show that the waves are constantly in intermediate water.

6.2.3. Base case

When mangroves are introduced into the model, they produce a modest additional reduction in wave height of 8.8% compared to the unvegetated base case. This is significantly lower than the field measurements discussed in Section 2.6, where reductions of 75% over stretches of 80 meters were reported. The key factor contributing to this discrepancy is likely the mangrove parameterisation used in this study. A comparison with field measurements presented by Lopez-Arias et al. (2024) reveals that the frontal area values applied here are relatively low. Measurements on other coasts show frontal areas four times higher across all vertical layers of the mangrove profile, which would result in substantially greater wave attenuation.

Another influence is the use of a bulk drag coefficient of 1. For the base case, the Keulegan-Carpenter number, based on a representative diameter of 2.4 cm and a water depth of 3.09 m, is 37.8. Lying within the ranges observed in the flume model and outside the influence range of inertial forces, as discussed in Section 2.3.4. Based on the analytical $\tilde{C}_d$–KC relationship, a value of $\tilde{C}_d \approx 1.2$ would be more appropriate. However, results from the flume model suggest that such values may underestimate attenuation when using a layered approach, and that higher values may yield more realistic outcomes. Since a conservative value of $\tilde{C}_d = 1$ is used throughout this study, the resulting attenuation is likely underestimated.

Finally, numerical dissipation may also play a role in the limited attenuation observed. As shown in the sensitivity analysis and supported by literature (Maza et al., 2019), larger wave heights tend to produce greater attenuation. As waves propagate along the transect, their height decreases due to both mangrove-induced wave attenuation and numerical damping. This reduction in wave height further reduces the attenuation rates. Without any numerical damping in the model, wave heights towards the end would be higher, and thus result in more total attenuation.

6.2.4. Sensitivity analysis

This section discusses the outcomes of the sensitivity analysis and their implications for modelling mangrove-induced wave attenuation for real-world coasts. The results clearly show that wave attenuation is highly sensitive to changes in hydrodynamic conditions, vegetation properties, and modelling approaches.

Reduced water levels

The sensitivity analysis confirms that lower water levels lead to significantly higher wave attenuation. At reduced water depths, a larger proportion of the mangrove root system is engaged with the wave motion. Since the roots typically offer the highest drag due to their complex and dense structure, this results in more substantial wave dissipation. These findings are in line with field observations such as those reported by (Mazda et al., 2006).

Increased wave height

Higher wave heights result in greater wave attenuation due to the quadratic relationship between drag force and flow velocity. As orbital velocities increase with wave height, the energy dissipation through drag increases accordingly. This relationship is well-documented in both laboratory experiments and field studies (Bryant et al., 2022; Horstman et al., 2014; Kelty et al., 2022). Although the current study does not include breaking waves, it is essential to note that under extreme wave conditions, wave breaking would further enhance energy dissipation before reaching the coastline.

Drag force changes

The influence of changes in the total drag, signifying changes in the mangrove density or bulk drag coefficient, shows larger attenuation rates for larger drag forces. Increasing $\tilde{C}$d from 0.66 to 1 resulted in a 44% increase in attenuation, while a further increase to $\tilde{C}$d $= 1.5$ led to an additional 38% increase. Although not perfectly linear, these results are consistent with trends found in experimental studies where increasing vegetation density led to proportionally higher attenuation rates (Anderson & Smith, 2014; Kelty et al., 2022). This reinforces the critical role of accurate vegetation measurements.

Avicennia parametrisation

Runs with the Avicennia parametrisation showed attenuation more than halved compared to the Rhizophora parametrisation. This can be explained by the significant difference in submerged frontal area added by the roots of the Rhizophora trees. Similar results are also found in field studies such as that of Horstman et al. (2014), where attenuation rates more than six times as high were found for the Rhizophora zones compared to the Avicennia/Sonnerita zones. These differences not only depend on species, but also on tree densities. The large differences in attenuation between species highlight the need for precise information on the species composition in an area.

Depth-averaged frontal area

Similar to the results of the flume, using a depth-averaged frontal area results in a much larger total amount of damping. The added attenuation is more than twice as large as that of the base case, more

significant than has been observed in any of the flume cases, where the depth-averaged frontal area showed a 30% higher attenuation rate than the layered approach. Where the flume study had water levels reaching up to the beginning of the stem, with most of the water passing through different sections of the roots, the case study also has a significant amount of trunk submerged, as seen in Figure 4.10. Thus, there is a substantial difference in frontal area between different layers. This larger difference could result in a larger change in the velocity profile, which could explain the significant difference in attenuation between the layered approach and the depth-averaged approach. This further proves the need for using a layered approach in these models.

6.2.5. Comparison with analytical damping

The Analytical formulations follow the model outcomes relatively well, with a difference of only 2.2% for the base case and 3.0% for the larger wave height scenario. It could be concluded that the model represents the analytical solution well, and thus, that the model performs well. However, based on other findings in this study, this agreement between the model outcomes and the analytical approach is unexpected and leads to more doubt on the performance of the model. In the flume model, results showed that most cases exhibited a significant difference between the analytical and model outcomes, with analytical results showing a larger total attenuation. From the closer analysis of HC5, this difference was most significantly attributed to the difference in mangrove parametrisation, with a depth-averaged frontal area approach leading to a 30% increase in damping compared to the layered approach. A similar result is found in the case study, where the depth-averaged run shows an added attenuation more than twice as high as that of the depth-averaged approach. Based on this, a much higher attenuation of the analytical approach is to be expected. Possibilities of this discrepancy can be found in uncertainties in the model. Another option might be that for irregular waves, the difference between the RANS model and the analytical assumption of linear wave theory leads to larger differences, counteracting the overestimation as a result of the depth-averaged approach. For a more conclusive answer to this, a finer mesh should be used to study.

6.3. Limitations

While this study shows potential for the application of the method, it also has its limitations, which are essential to discuss for a better understanding of the result and its implications.

- **Skewness:** The flume model represents the waves with a larger skewness than the experiment, especially for HC3 and HC4, which could lead to higher peak velocities, and thus larger drag forces.
- **Numerical dissipation:** The largest limitation of the case study model is the significant numerical dissipation. This prohibits any of the results from being used for quantitative analysis and, more generally, reduces the reliability of the model outcomes. The current constraints on modelling time of 24 hours with 64 cores restricts any possibility for a finer mesh.
- **Measurement fluctuations:** Both models show fluctuations in measurements, where otherwise smoother trends are expected. For the flume model, this is visible in the calibration section, where a smooth line is expected in a straight flume without any obstructions. For the case study, this is the most obvious in the first few gauges before the first mangrove zone. With inputs being the same, and no effect of the mangroves being expected, the measurements at these gauges would be assumed to be the same, but instead, small deviations for different runs are observable.
- **Wave gauge errors:** For some runs, wave gauges have also shown unrealistic values due to an error, with values being either more than twice as high, or 0. These outliers have been removed from the plots and are not taken into consideration. The reason behind this is unknown.
- **Wave representation:** In the case study, the wave parameters are not represented in the model with total accuracy. The initial wave heights as measured by the first gauge are several centimetres below the values determined in Section 4.2.4. This could be due to errors in the assumed wave spectrum, the wave properties or the generation in the model.
- **Mangrove representation:** For the case study, the mangrove representation rests on many assumptions and would require a more extensive measurement campaign for it to
- **2-dimensional:** Since the model uses a 2D vertical plane, it neglects lateral variability and cross-

shore hydrodynamics. Lateral changes in vegetation properties and hydrodynamic processes, such as refraction and diffraction, can not be captured. This restricts the model's ability to capture all the complexity involved in mangrove-induced wave attenuation.

- **Bottom friction and turbulence:** Currently, both bottom friction and turbulence are not included in the model, but could lead to accuracy errors.
- **Statistical significance:** Further limitations of this study lie in the numerical significance. With only 7 different hydrodynamic conditions analysed, and the velocity profile of only one condition, this restricts the generalisation of the findings.
- **Drag parametrisation:** in OpenFOAM, drag is applied per cell. This constrains the parametrisation of mangroves to the cell dimensions.

7
Conclusion

The goal of this research was to evaluate the modelling capabilities of a 2DV OpenFOAM model in simulating the attenuation capacity of mangrove forests. The study involved the development of two different models: a flume model, replicating the physical experiment done by Kelty et al. (2022), and a case study model replicating a transect through the Mandai mangrove forest in Singapore. Both models applied a layered approach to replicate the distinct variations in frontal area over the height of Rhizophora trees.

This chapter addresses the three sub-questions stated in the introduction and synthesises the findings to answer the main research question.

1. How can OpenFOAM be used to more accurately capture the frontal area variations over the height of mangroves in wave modelling?

To capture the frontal area variations of mangroves, this study implemented different layers, each with its distinct frontal area, to capture these variations and their effects on the drag force exerted by the mangroves. These layers consisted of multiple different layers to capture varying root characteristics, combined with one layer for the trunk.

The flume simulations demonstrate that this layered approach significantly influences wave attenuation outcomes. A comparison with a depth-averaged frontal area approach showed that the latter overestimated attenuation. Further investigation in the velocity profile showed significant influence of frontal area variations and challenges the validity of the assumption of frontal area uniformity over the depth, as used for many implementations such as the SWAN implementation of Suzuki et al. (2012).

2. What benefit can OpenFOAM provide in decreasing the uncertainty of the relation between the bulk drag coefficient and the Keulegan-Carpenter number?

After calibration, the flume model runs show good agreement with the experimental measurements. Average deviations of single wave gauges from the attenuation trend were smaller for the model outcomes, and β values were replicated to within 3% accuracy.

However, contrary to the original hypothesis, the uncertainty of the $\tilde{C}_\mathrm{d}$ - KC relation did not decrease for the calibrated bulk drag coefficients. Changes in the velocity profile due to different layers cause a non-linear influence of the drag force on the attenuation that could be consequential to this mismatch.

3. To what extent can an OpenFOAM model accurately predict the wave attenuation for the North-West coast of Singapore?

Due to excessive numerical damping in the case study model, the model created for this study cannot be used for any quantitative predictions. The sensitivity analysis still allowed for a qualitative analysis showing the influence of different parameters on the total attenuation. The setup of the flume further proves that with more available computational power. By using a finer mesh, an OpenFOAM model can lead to increased accuracy for wave attenuation modelling, as it shows the capability of simulating complex hydrodynamics for a wide range of scenarios.

Answering these sub-questions then allows the main question to be answered:

To what extent can a 2DV OpenFOAM accurately represent wave attenuation due to mangrove forests for flume tests and real coasts?

This study provides new insights into the application of mangroves in CFD. With calibration on wave measurements, the model is capable of accurately reproducing wave attenuation for different hydrodynamics. By solving the Reynolds Averaged Navier Stokes equations and incorporating a layered mangrove parametrisation, the model captures non-linear interactions between the depth-varying drag force and the velocity profile. This approach revealed lower attenuation rates than those predicted by traditional depth-averaged models, underscoring its importance.
Furthermore, the model proved to be applicable to real-world scenarios. It successfully simulated the influence of varying forest extents, wave heights, and vegetation densities, while also accounting for complex bathymetry. Although numerical damping limited quantitative accuracy in the case study, the model provided valuable qualitative insights, confirming its potential as a tool for assessing mangrove-induced wave attenuation in both experimental and real-world scenarios.

8
Recommendations

Future research

One of the most critical questions emerging from this study is how to establish a reliable and generalizable relationship for the bulk drag coefficient, $\tilde{C}$d, that accounts for the influence of depth-varying velocity profiles. Future research could analyse a larger number of scenarios to obtain a statistically significant dataset. Besides replicating physical experiments, flume conditions could also be manipulated solely in the numerical model. This could more easily allow for the isolation of specific parameters, such as vegetation density, and be less costly.

To find a suitable relationship for the calibrated $\tilde{C}_\mathrm{d}$ values, Machine learning could be used, as it can be very effective in finding non-linear patterns with many variables. Active learning methods can help guide the selection of model scenarios, reducing the required number of simulations. Since the number of layers is arbitrarily defined, it could be suggested to start with two different layers, one for the roots and one for the trunk. This would simplify the system drastically, allowing for easier analysis.

Another promising addition to the model could be the inclusion of canopies in the parameterisation of mangroves. Canopies can provide significant attenuation, particularly during high water conditions when waves interact with the flexible canopy. This would require a different approach than is used for the trunk and roots, as the assumption of rigidity, necessary for these calculations, does not hold for the flexible leaves and branches (van Veelen et al., 2020). To incorporate this, the Euler-Bernoulli beam theory can be used to estimate the drag force in flexible parts of the trees without further calibration of a drag coefficient (van Veelen et al., 2021).

Furthermore, OpenFOAM models could be used to study bound long waves interactions. The dissipation and transformation of these waves by mangroves remains poorly understood, yet they can contribute significantly to coastal flooding and erosion. OpenFOAM models can help in understanding these interactions by allowing the simulation of many wave conditions, focused on understanding this interaction, with a much lower cost compared to physical modelling.

Mandai mangrove area

Despite the inability of the current model to provide accurate quantitative predictions for wave attenuation by mangroves in the Mandai area on the north-west coast of Singapore, it can still offer valuable insights for future engineering efforts. Currently, the design of coastal protection structures in the area, such as levees, does not account for the potential wave attenuation provided by mangroves. Incorporating this natural damping could lead to a reduction in required levee heights, offering both cost savings and environmental benefits. Implementation should draw inspiration from Mancheño et al. (2024), considering both tree growth and stability.

The first recommendation for future modelling is to adopt a finer mesh. The current mesh exhibited significant numerical dissipation, which compromised the accuracy of the results. A finer mesh, combined with calibration on its accuracy, is essential to ensure that numerical errors are minimised and that the model can reliably capture the wave attenuation. Finer meshes would, however, result in longer modelling times. Halving the mesh size requires 8 times the computational power of the currently used 24 hours with 64 cores. Based on the findings of the flume, halving the mesh size, thus octupling computational demand, would result in acceptable numerical dissipation, but this would require further validation.

Secondly, a more accurate representation of the mangrove forest composition is crucial. This study demonstrated that the attenuation from the Rhizophora parameterisation is nearly three times larger than that of Avicennia under similar conditions. Results also showed that simplified representations using depth-averaged frontal areas can lead to a substantial overestimation of wave attenuation, highlighting the importance of a layered approach and accurate root measurements. Variation in the densities also had a significant impact on the amount of attenuation. Accurate, site-specific measurements of root dimensions, trunk properties, and canopy characteristics are essential to prevent overestimation of attenuation, which could lead to unsafe coastal designs.

However, collecting accurate in situ measurements remains challenging. Manual fieldwork is the most reliable but labour-intensive and impractical for large-scale studies. Satellite imagery offers broader coverage but struggles to capture understory features, which, as this study highlights, play a significant role in wave attenuation (Hyyppä et al., 2020). While local allometric relationships can help estimate these features, they often reduce accuracy. Ground-based technologies such as LiDAR or Terrestrial Laser Scanning offer a balanced alternative, combining higher accuracy than satellite data with greater efficiency than manual measurements (Dunlop et al., 2025).

Furthermore, future modelling should incorporate the impacts of sea level rise. The sensitivity analysis revealed that wave attenuation remained relatively constant across water level variations, with no significant influence from the bottom. Literature shows, however, that as water depths increase, the relative contribution of root structures to wave attenuation reduces, resulting in a lower amount of attenuation. Therefore, accounting for projected sea level rise is essential for improving the accuracy of future scenario predictions.

Additionally, the adaptive capacity of mangrove ecosystems should be considered. Depending on factors such as species composition, sediment availability, and hydrodynamic conditions, mangrove forests may be able to keep pace with rising sea levels. Integrating this dynamic response into future models will enhance the reliability of long-term predictions.

Engineering application

The case study and its sensitivity analysis demonstrate the possibilities of this modelling approach for real-world applications, with its advantages in its ability to simulate complex bathymetry, hydrodynamic conditions and different forest parameters.

The flume study furthermore showed the ability of the model to recreate attenuation trends after calibration, and it demonstrated its ability to model the complex relation between depth-varying drag force and the resulting velocity profiles, questioning the validity of the assumption of a uniform representation.

The lack of correlation, and thus the capability of predicting the bulk drag coefficient, highlights the current limitations of this model. Without an accurate method to determine $\tilde{C}_\mathrm{d}$ for a given scenario, the model loses credibility for wave attenuation predictions. This CFD approach could be used in combination with a depth-averaged single layer, for which the $\tilde{C}_\mathrm{d}$-KC correlation is likely better, while still having the advantage of CFD modelling to capture complex wave dynamics.

For further use of the layered approach for real-coast applications, calibration and validation on field measurements could provide a crucial addition for the applicability and reliability of this implementation, and would therefore be highly recommended.

The development of a predictive method to determine $\tilde{C}_\mathrm{d}$ for the layered approach would lead to a great improvement for this model, and could enable further advances in the accuracy of determining mangrove-induced wave attenuation.

Other additions to the model could further improve the realism. More lateral layers can be added to capture differences in forest densities along a transect. A levee can also be added at the end of the transect to model the actual wave run-up and gain a better understanding of the influence of mangroves on levee design. If computational time allows it, or for smaller areas, 3D simulations could also allow the spatial variability of the mangrove forest to be included, and can model its interaction with hydrodynamic phenomena such as reflection and refraction.

References

Anderson, M. E., & Smith, J. M. (2014). Wave attenuation by flexible, idealized salt marsh vegetation. *Coastal Engineering*, *83*, 82–92. https://doi.org/10.1016/j.coastaleng.2013.10.004

Baron-Hyppolite, C., Lashley, C. H., Garzon, J., Miesse, T., Ferreira, C., & Bricker, J. D. (2019). Comparison of Implicit and Explicit Vegetation Representations in SWAN Hindcasting Wave Dissipation by Coastal Wetlands in Chesapeake Bay [Number: 1 Publisher: Multidisciplinary Digital Publishing Institute]. *Geosciences*, *9*(1), 8. https://doi.org/10.3390/geosciences9010008

Bird, M., Chua, S., Fifield, L. K., Teh, T. S., & Lai, J. (2004). Evolution of the Sungei Buloh–Kranji mangrove coast, Singapore. *Applied Geography*, *24*(3), 181–198. https://doi.org/10.1016/j.apgeog.2004.04.002

Bosboom, J., & Stive, M. J. F. (2023, January). *Coastal Dynamics* [Publication Title: TU Delft OPEN Books]. TU Delft OPEN Books. https://doi.org/10.5074/T.2021.001

Brinkman, R. M. (2006). Wave attenuation in mangrove forests: An investigation through field and theoretical studies.

Broekema, Y. (2013). Hydrodynamic modelling of a mangrove system in Singapore.

Bryant, M., Bryant, D., Provost, L., Hurst, N., McHugh, M., Wargula, A., & Tomiczek, T. (2022, September). *Wave attenuation of coastal mangroves at a near-prototype scale* (tech. rep.). Engineer Research and Development Center (U.S.) https://doi.org/10.21079/11681/45565

Cao, H., Chen, Y., Tian, Y., & Feng, W. (2016). Field Investigation into Wave Attenuation in the Mangrove Environment of the South China Sea Coast [Publisher: Coastal Education and Research Foundation]. *Journal of Coastal Research*, *32*(6), 1417–1427. https://doi.org/10.2112/JCOASTRES-D-15-00124.1

Carrasquilla-Henao, M., & Juanes, F. (2017). Mangroves enhance local fisheries catches: A global meta-analysis. *Fish and Fisheries*, *18*(1), 79–93. https://doi.org/10.1111/faf.12168

Chang, C.-W., Mori, N., Tsuruta, N., & Suzuki, K. (2019). Estimation of Wave Force Coefficients on Mangrove Models. *Journal of Japan Society of Civil Engineers, Ser. B2 (Coastal Engineering)*, *75*(2), I_1105–I_1110. https://doi.org/10.2208/kaigan.75.I_1105

Chang, C.-W., Mori, N., Tsuruta, N., Suzuki, K., & Yanagisawa, H. (2022). An Experimental Study of Mangrove-Induced Resistance on Water Waves Considering the Impacts of Typical Rhizophora Roots. *Journal of Geophysical Research: Oceans*, *127*(6), e2022JC018653. https://doi.org/10.1029/2022JC018653

Chen, H., Ni, Y., Li, Y., Liu, F., Ou, S., Su, M., Peng, Y., Hu, Z., Uijttewaal, W., & Suzuki, T. (2018). Deriving vegetation drag coefficients in combined wave-current flows by calibration and direct measurement methods. *Advances in Water Resources*, *122*, 217–227. https://doi.org/10.1016/j.advwatres.2018.10.008

Chen, Q., Li, Y., Kelly, D. M., Zhang, K., Zachry, B., & Rhome, J. (2021). Improved modeling of the role of mangroves in storm surge attenuation. *Estuarine, Coastal and Shelf Science*, *260*, 107515. https://doi.org/10.1016/j.ecss.2021.107515

Choudhary, B., Dhar, V., & Pawase, A. S. (2024). Blue carbon and the role of mangroves in carbon sequestration: Its mechanisms, estimation, human impacts and conservation strategies for economic incentives. *Journal of Sea Research*, *199*, 102504. https://doi.org/10.1016/j.seares.2024.102504

Conservation, R. (2020, November). Rhizophora mucronata. Retrieved June 2, 2025, from https://www.facebook.com/reefconservationmu/posts/rhizophora-mucronatarhizophora-mucronata-commonly-known-as-the-red-mangrove-is-t/3457459311012825/

Dalrymple, R. A., Kirby, J. T., & Hwang, P. A. (1984). Wave Diffraction Due to Areas of Energy Dissipation [Publisher: American Society of Civil Engineers]. *Journal of Waterway, Port, Coastal, and Ocean Engineering*, *110*(1), 67–79. https://doi.org/10.1061/(ASCE)0733-950X(1984)110:1(67)

Deshpande, S. S., Anumolu, L., & Trujillo, M. F. (2012). Evaluating the performance of the two-phase flow solver interFoam [Publisher: IOP Publishing]. *Computational Science & Discovery*, *5*(1), 014016. https://doi.org/10.1088/1749-4699/5/1/014016

DHPC. (2024). DelftBlue Supercomputer (Phase 2). https://doc.dhpc.tudelft.nl/delftblue/

Dunlop, T., Mancheño, A. G., Glamore, W., Felder, S., & Van Wesenbeeck, B. K. (2025). Quantifying Mangrove Forest Attributes Using Terrestrial Laser Scanning [Publisher: Springer Science and Business Media LLC]. *Estuaries and Coasts*, *48*(4). https://doi.org/10.1007/s12237-025-01533-0

Feller, I. C., Lovelock, C. E., Berger, U., McKee, K. L., Joye, S. B., & Ball, M. C. (2010). Biocomplexity in Mangrove Ecosystems [Publisher: Annual Reviews]. *Annual Review of Marine Science*, *2*(Volume 2, 2010), 395–417. https://doi.org/10.1146/annurev.marine.010908.163809

Friess, D. A., Phelps, J., Leong, R. C., Lee, W. K., & Wee, A. K. S. (2012). Mandai Mangrove, Singapore: Lessons for the Conservation of Southeast Asia's Mangroves.

Friess, D., Rogers, K., Lovelock, C., Krauss, K., Hamilton, S., Lee, S., Lucas, R., Primavera, J., Rajkaran, A., & Shi, S. (2019). The State of the World's Mangrove Forests: Past, Present, and Future. *Annual Review of Environment and Resources*, *44*, 1–27. https://doi.org/10.1146/annurev-environ-101718-033302

Friess, D. A., Richards, D. R., & Phang, V. X. H. (2016). Mangrove forests store high densities of carbon across the tropical urban landscape of Singapore. *Urban Ecosystems*, *19*(2), 795–810. https://doi.org/10.1007/s11252-015-0511-3

Getzner, M., & Islam, M. S. (2020). Ecosystem Services of Mangrove Forests: Results of a Meta-Analysis of Economic Values. *International Journal of Environmental Research and Public Health*, *17*(16), 5830. https://doi.org/10.3390/ijerph17165830

Goda, Y. (2010). Reanalysis of Regular and Random Breaking Wave Statistics. *Coastal Engineering Journal*, *52*(1), 71–106. https://doi.org/10.1142/S0578563410002129

Google Earth. (2024, July). Map showing Mandai Kechil. Retrieved April 24, 2025, from https://earth.google.com/web/

He, F., Chen, J., & Jiang, C. (2019). Surface wave attenuation by vegetation with the stem, root and canopy. *Coastal Engineering*, *152*, 103509. https://doi.org/10.1016/j.coastaleng.2019.103509

Heller, V. (2011). Scale effects in physical hydraulic engineering models [Publisher: Taylor & Francis]. *Journal of Hydraulic Research*. Retrieved April 23, 2025, from https://www.tandfonline.com/doi/abs/10.1080/00221686.2011.578914

Heller, V. (2017). Self-similarity and Reynolds number invariance in Froude modelling [Publisher: IAHR Website _eprint: https://doi.org/10.1080/00221686.2016.1250832]. *Journal of Hydraulic Research*, *55*(3), 293–309. https://doi.org/10.1080/00221686.2016.1250832

Hilton, M., & Manning, S. (1995). Conversion of Coastal Habitats in Singapore: Indications of Unsustainable Development. *Environmental Conservation*, *22*(4), 307–322. https://doi.org/10.1017/S0376892900034883

Hoque, A., Rahman, M., & Paul, G. C. (2023). 1D-2D mathematical modeling of wave refraction and wave attenuation by mangrove forests. *Ocean Engineering*, *286*, 115619. https://doi.org/10.1016/j.oceaneng.2023.115619

Horstman, E., Dohmen-Janssen, C., Narra, P., Van Den Berg, N., Siemerink, M., & Hulscher, S. (2014). Wave attenuation in mangroves: A quantitative approach to field observations. *Coastal Engineering*, *94*, 47–62. https://doi.org/10.1016/j.coastaleng.2014.08.005

Horstman, E., Dohmen-Janssen, M., & Hulscher, S. (2013). Modeling tidal dynamics in a mangrove creek catchment in Delft3D. *Coastal Dynamics*.

Huang, Z., Yao, Y., Sim, S. Y., & Yao, Y. (2011). Interaction of solitary waves with emergent, rigid vegetation. *Ocean Engineering*, *38*(10), 1080–1088. https://doi.org/10.1016/j.oceaneng.2011.03.003

Hyyppä, E., Yu, X., Kaartinen, H., Hakala, T., Kukko, A., Vastaranta, M., & Hyyppä, J. (2020). Comparison of Backpack, Handheld, Under-Canopy UAV, and Above-Canopy UAV Laser Scanning for Field Reference Data Collection in Boreal Forests [Number: 20 Publisher: Multidisciplinary Digital Publishing Institute]. *Remote Sensing*, *12*(20), 3327. https://doi.org/10.3390/rs12203327

Janssen, P. (2004, October). *The Interaction of Ocean Waves and Wind* (1st ed.). Cambridge University Press. https://doi.org/10.1017/CBO9780511525018

Jasak, H. (2009). OpenFOAM: Open source CFD in research and industry. *International Journal of Naval Architecture and Ocean Engineering*, *1*(2), 89–94. https://doi.org/10.2478/IJNAOE-2013-0011

Jordan, P., & Fröhle, P. (2022). Bridging the gap between coastal engineering and nature conservation? *Journal of Coastal Conservation*, *26*(2), 4. https://doi.org/10.1007/s11852-021-00848-x

Kalloe, S. A., Hofland, B., & Van Wesenbeeck, B. K. (2024). Scaled versus real-scale tests: Identifying scale and model errors in wave damping through woody vegetation. *Ecological Engineering*, *202*, 107241. https://doi.org/10.1016/j.ecoleng.2024.107241

Kelty, K., Tomiczek, T., Cox, D. T., Lomonaco, P., & Mitchell, W. (2022). Prototype-Scale Physical Model of Wave Attenuation Through a Mangrove Forest of Moderate Cross-Shore Thickness: LiDAR-Based Characterization and Reynolds Scaling for Engineering With Nature [Publisher: Frontiers]. *Frontiers in Marine Science*, *8*. https://doi.org/10.3389/fmars.2021.780946

Koon, Y. A. T., Ang, W. F., Teo, S., Liew, S. C., & Tan, H. (2010). The present extent of mangrove forests in Singapore. *Nature in Singapore*, *2010*.

Larsen, B. E., & Fuhrman, D. R. (2018). On the over-production of turbulence beneath surface waves in Reynolds-averaged Navier–Stokes models. *Journal of Fluid Mechanics*, *853*, 419–460. https://doi.org/10.1017/jfm.2018.577

Le Méhauté, B. (1976). *An Introduction to Hydrodynamics and Water Waves*. Springer Berlin Heidelberg. https://doi.org/10.1007/978-3-642-85567-2

Loon, A. F. V., Brake, B. T., Huijgevoort, M. H. J. V., & Dijksma, R. (2016). Hydrological Classification, a Practical Tool for Mangrove Restoration [Publisher: Public Library of Science]. *plos one*, *11*(3), e0150302. https://doi.org/10.1371/journal.pone.0150302

Lopez-Arias, F., Maza, M., Calleja, F., Govaere, G., & Lara, J. L. (2024). Integrated drag coefficient formula for estimating the wave attenuation capacity of Rhizophora sp. mangrove forests [Publisher: Frontiers]. *Frontiers in Marine Science*, *11*. https://doi.org/10.3389/fmars.2024.1383368

Mancheño, A. G., Vuik, V., van Wesenbeeck, B. K., Jonkman, S. N., van Hespen, R., Moll, J. R., Kazi, S., Urrutia, I., & van Ledden, M. (2024). Integrating mangrove growth and failure in coastal flood protection designs [Publisher: Nature Publishing Group]. *Scientific Reports*, *14*(1), 7951. https://doi.org/10.1038/s41598-024-58705-4

Maza, M., Lara, J. L., Losada, I. J., Ondiviela, B., Trinogga, J., & Bouma, T. J. (2015). Large-scale 3-D experiments of wave and current interaction with real vegetation. Part 2: Experimental analysis. *Coastal Engineering*, *106*, 73–86. https://doi.org/10.1016/j.coastaleng.2015.09.010

Maza, M., Adler, K., Ramos, D., Garcia, A. M., & Nepf, H. (2017). Velocity and Drag Evolution From the Leading Edge of a Model Mangrove Forest. *Journal of Geophysical Research: Oceans*, *122*(11), 9144–9159. https://doi.org/10.1002/2017JC012945

Maza, M., Lara, J. L., & Losada, I. J. (2019). Experimental analysis of wave attenuation and drag forces in a realistic fringe *Rhizophora* mangrove forest. *Advances in Water Resources*, *131*, 103376. https://doi.org/10.1016/j.advwatres.2019.07.006

Maza, M., Lara, J. L., & Losada, I. J. (2015). Tsunami wave interaction with mangrove forests: A 3-D numerical approach. *Coastal Engineering*, *98*, 33–54. https://doi.org/10.1016/j.coastaleng.2015.01.002

Mazda, Y., Magi, M., Ikeda, Y., Kurokawa, T., & Asano, T. (2006). Wave reduction in a mangrove forest dominated by Sonneratia sp. *Wetlands Ecology and Management*, *14*(4), 365–378. https://doi.org/10.1007/s11273-005-5388-0

McIvor, A., Möller, I., Spencer, T., & Spalding, M. (2012). Reduction of wind and swell waves by mangroves. Natural coastal protection series: Report 1. Cambridge Coastal Research Unit working paper 40. *Reduction of wind and swell waves by mangroves, Natural Coastal Protection Series: Report 1*.

Mendez, F. J., & Losada, I. J. (2004). An empirical model to estimate the propagation of random breaking and nonbreaking waves over vegetation fields. *Coastal Engineering*, *51*(2), 103–118. https://doi.org/10.1016/j.coastaleng.2003.11.003

Mendez, M. A., Di Narco, M., & Benocci, C. (2017). Running FineOpen43 Simulations at VKI: A tutorial and a collection of scripts.

Miche, R. (1944). Mouvements ondulatoires de l'océan pour une eau profonde constante et décroissante. Annales des Ponts et Chaussées. *Annales des Ponts et Chauss´ees*, *114*, 369–406.

Morison, J., Johnson, J., & Schaaf, S. (1950). The Force Exerted by Surface Waves on Piles. *Journal of Petroleum Technology*, *2*(05), 149–154. https://doi.org/10.2118/950149-G

Nagelkerken, I., Blaber, S. J. M., Bouillon, S., Green, P., Haywood, M., Kirton, L. G., Meynecke, J. .-., Pawlik, J., Penrose, H. M., Sasekumar, A., & Somerfield, P. J. (2008). The habitat function of mangroves for terrestrial and marine fauna: A review. *Aquatic Botany*, *89*(2), 155–185. https://doi.org/10.1016/j.aquabot.2007.12.007

Ohira, W., Honda, K., Nagai, M., & Ratanasuwan, A. (2013). Mangrove stilt root morphology modeling for estimating hydraulic drag in tsunami inundation simulation. *Trees*, *27*(1), 141–148. https://doi.org/10.1007/s00468-012-0782-8

Ozeren, Y., Wren, D. G., & Wu, W. (2014). Experimental Investigation of Wave Attenuation through Model and Live Vegetation [Publisher: American Society of Civil Engineers]. *Journal of Waterway, Port, Coastal, and Ocean Engineering*, *140*(5), 04014019. https://doi.org/10.1061/(ASCE)WW.1943-5460.0000251

Phan, K. L., Stive, M. J. F., Zijlema, M., Truong, H. S., & Aarninkhof, S. G. J. (2019). The effects of wave non-linearity on wave attenuation by vegetation. *Coastal Engineering*, *147*, 63–74. https://doi.org/10.1016/j.coastaleng.2019.01.004

Quang Bao, T. (2011). Effect of mangrove forest structures on wave attenuation in coastal Vietnam. *Oceanologia*, *53*(3), 807–818. https://doi.org/10.5697/oc.53-3.807

Quartel, S., Kroon, A., Augustinus, P., Van Santen, P., & Tri, N. (2007). Wave attenuation in coastal mangroves in the Red River Delta, Vietnam. *Journal of Asian Earth Sciences*, *29*(4), 576–584. https://doi.org/10.1016/j.jseaes.2006.05.008

Seddon, N., Chausson, A., Berry, P., Girardin, C. A. J., Smith, A., & Turner, B. (2020). Understanding the value and limits of nature-based solutions to climate change and other global challenges [Publisher: Royal Society]. *Philosophical Transactions of the Royal Society B: Biological Sciences*, *375*(1794), 20190120. https://doi.org/10.1098/rstb.2019.0120

Shan, C. H. (2025). New Mandai mangrove and mudflat nature park, enhanced Bukit Batok nature corridor await from 2028. *The Straits Times*. Retrieved May 22, 2025, from https://www.straitstimes.com/singapore/new-mandai-mangrove-and-mudflat-park-enhanced-bukit-batok-nature-corridor-await-visitors-from-2028

Smith, J. M., Bryant, M. A., & Wamsley, T. V. (2016). Wetland buffers: Numerical modeling of wave dissipation by vegetation [_eprint: https://onlinelibrary.wiley.com/doi/pdf/10.1002/esp.3904]. *Earth Surface Processes and Landforms*, *41*(6), 847–854. https://doi.org/10.1002/esp.3904

Spalding, M., Kainuma, M., & Collins, L. (2010). World Atlas of Mangroves. https://doi.org/10.34892/W2EW-M835

Suzuki, T., Hu, Z., Kumada, K., Phan, L., & Zijlema, M. (2019). Non-hydrostatic modeling of drag, inertia and porous effects in wave propagation over dense vegetation fields. *Coastal Engineering*, *149*, 49–64. https://doi.org/10.1016/j.coastaleng.2019.03.011

Suzuki, T., Zijlema, M., Burger, B., Meijer, M. C., & Narayan, S. (2012). Wave dissipation by vegetation with layer schematization in SWAN. *Coastal Engineering*, *59*(1), 64–71. https://doi.org/10.1016/j.coastaleng.2011.07.006

Tan. (2011). Flikr page of Ria Tan. Retrieved May 6, 2025, from https://www.flickr.com/photos/wildsingapore/

Tembusu. (2024, December). Environmental impact assessment (EIA) for proposed Mandai Mangrove & Mudflat nature park. https://www.nparks.gov.sg/docs/default-source/nature-docs/environmental-studies-sustainable-development/mmm-eia-(public-disclosure).pdf?sfvrsn=3c1f1327_1

Tusinski, A., & Verhagen, H. J. (2014). The use of mangroves in coastal protection. *Coastal Engineering Proceedings*, *1*(34), 45. https://doi.org/10.9753/icce.v34.management.45

van Veelen, T. J., Fairchild, T. P., Reeve, D. E., & Karunarathna, H. (2020). Experimental study on vegetation flexibility as control parameter for wave damping and velocity structure [Publisher: Elsevier BV]. *Coastal Engineering*, *157*, 103648. https://doi.org/10.1016/j.coastaleng.2020.103648

van Veelen, T. J., Karunarathna, H., & Reeve, D. E. (2021). Modelling wave attenuation by quasi-flexible coastal vegetation [Publisher: Elsevier BV]. *Coastal Engineering*, *164*, 103820. https://doi.org/10.1016/j.coastaleng.2020.103820

van Wesenbeeck, B. K., van Zelst, V. T. M., Antolinez, J. A. A., & de Boer, W. P. (2025). Quantifying uncertainty in wave attenuation by mangroves to inform coastal green belt policies [Publisher: Nature Publishing Group]. *Communications Earth & Environment*, *6*(1), 1–8. https://doi.org/10.1038/s43247-025-02178-4

van Zelst, V. T. M., Dijkstra, J. T., van Wesenbeeck, B. K., Eilander, D., Morris, E. P., Winsemius, H. C., Ward, P. J., & de Vries, M. B. (2021). Cutting the costs of coastal protection by integrating vegetation in flood defences [Publisher: Nature Publishing Group]. *Nature Communications*, *12*(1), 6533. https://doi.org/10.1038/s41467-021-26887-4

Wang, Y., Yin, Z., & Liu, Y. (2020). Numerical investigation of solitary wave attenuation and resistance induced by rigid vegetation based on a 3-D RANS model. *Advances in Water Resources*, *146*, 103755. https://doi.org/10.1016/j.advwatres.2020.103755

Wang, Y., Yin, Z., & Liu, Y. (2022). Experimental investigation of wave attenuation and bulk drag coefficient in mangrove forest with complex root morphology. *Applied Ocean Research*, *118*, 102974. https://doi.org/10.1016/j.apor.2021.102974

Willemsen, P., Horstman, E., Borsje, B., Friess, D., & Dohmen-Janssen, C. (2016). Sensitivity of the sediment trapping capacity of an estuarine mangrove forest. *Geomorphology*, *273*, 189–201. https://doi.org/10.1016/j.geomorph.2016.07.038

Wu, W. C., & Cox, D. T. (2015). Effects of wave steepness and relative water depth on wave attenuation by emergent vegetation. *Estuarine, Coastal and Shelf Science*, *164*, 443–450. https://doi.org/10.1016/j.ecss.2015.08.009

Wu, W., & Marsooli, R. (2012). A depth-averaged 2D shallow water model for breaking and non-breaking long waves affected by rigid vegetation. *Journal of Hydraulic Research*, *50*(6), 558–575. https://doi.org/10.1080/00221686.2012.734534

Yee, A. T. K., Ang, W. F., Teo, S., Liew, S. C., & Tan, H. T. W. (2010). The present extent of mangroves in Singapore.

Zhang, R., Chen, Y., Lei, J., Zhou, X., Yao, P., & Stive, M. J. F. (2023). Experimental investigation of wave attenuation by mangrove forests with submerged canopies. *Coastal Engineering*, *186*, 104403. https://doi.org/10.1016/j.coastaleng.2023.104403

Zhao, K., Wang, Y., & Liu, P. L. .-. (2024). A guide for selecting periodic water wave theories - Le Méhauté (1976)'s graph revisited. *Coastal Engineering*, *188*, 104432. https://doi.org/10.1016/j.coastaleng.2023.104432

A

Wave conditions of flume experiment

The wave conditions used in the experiments of Bryant et al. (2022).

Table A.1: Incident wave conditions (measured at WG 12).

Irregular Waves			Regular Waves		
h [m]	H_{m0} **[cm]**	T_p **[sec]**	**h [m]**	H_i **[cm]**	T **[sec]**
0.35	7.9	2.0	0.35	12.3	2.0
0.35	9.5	2.5	0.35	20.1	2.5
0.35	9.6	3.0	0.35	16.6	3.0
0.35	9.6	4.0	0.35	21.1	4.0
0.35	11.1	2.0	0.50	10.6	2.0
0.35	13.8	2.5	0.50	16.0	2.5
0.35	13.8	3.0	0.50	15.0	3.0
0.35	13.7	4.0	0.50	15.4	4.0
0.50	7.3	2.0	0.50	28.2	2.0
0.50	9.3	2.5	0.50	35.2	2.5
0.50	9.2	3.0	0.50	33.2	3.0
0.50	9.1	4.0	0.50	28.5	4.0
0.50	11.1	2.0	0.70	11.6	2.0
0.50	14.1	2.5	0.70	15.0	2.5
0.50	14.1	3.0	0.70	14.0	3.0
0.50	13.9	4.0	0.70	17.3	4.0
0.50	14.6	2.0	0.70	31.4	2.0
0.50	18.5	2.5	0.70	33.8	2.5
0.50	24.3	3.0	0.70	32.1	3.0
0.50	24.5	4.0	0.70	38.1	4.0
0.70	7.5	2.0	1.0	12.1	2.0
0.70	9.4	2.5	1.0	15.0	2.5
0.70	9.2	3.0	1.0	14.8	3.0
0.70	9.2	4.0	1.0	14.4	4.0
0.70	11.4	2.0	1.0	30.7	2.0
0.70	14.0	2.5	1.0	28.8	2.5
0.70	14.0	3.0	1.0	29.2	3.0
0.70	14.0	4.0	1.0	31.2	4.0
0.70	14.8	2.0			
0.70	18.7	2.5			
0.70	26.8	3.0			
0.70	27.7	4.0			
1.0	8.2	2.0			
1.0	9.8	2.5			
1.0	9.3	3.0			
1.0	9.0	4.0			
1.0	12.0	2.0			
1.0	14.8	2.5			
1.0	14.3	3.0			
1.0	14.0	4.0			
1.0	15.6	2.0			
1.0	19.6	2.5			
1.0	28.8	3.0			
1.0	29.1	4.0			

B

Mandai mangrove overview

Figure B.1: Pictures from the Mandai area showing many different species mixed (Tan, 2011)

C
Additional model settings

This appendix describes the additional settings used in the model such as the boundary conditions and settings for numerical stability

C.1. Numerical stability

The timesteps were set to auto adjust to remain stable. For both cases a maxCo of 0.6 s and maxAlpaCo of 0.4 s. These values are wel withing the safe range for avoiding numerical instabilities. For the flume case a max delta T value of 0.005 s was chosen. For Case study runs 0.08 s. Higher values could cause significant reductions in modelling time, but proved to result in instabilities in some cases.

C.2. Boundary conditions

	inlet	outlet	atmosphere	Bottom	front/back	grass
`alpha1`	zeroGradient	zeroGradient	inletOutlet	zeroGradient	empty	zeroGradient
`U`	zeroGradient	fixedValue	zeroGradient	noSlip	empty	fixedValue
`p_rgh`	zeroGradient	zeroGradient	totalPressure	zeroGradient	empty	zeroGradient

Table C.1: Boundary conditions used for different variables across domain boundaries.

C.3. Computational resources

The models are run using the DelftBlue supercomputer of the TU Delft. A maximum of 64 cores can be used simultanuously. The cores are Intel XEON E5-6248R 24C, with a clock speed of 3.0GHz (DHPC, 2024). The maximum allowable time for master students is 24 hours.

D
Data analysis

This discusses the data analysis methods as used for this study

D.1. Water levels

To read out the water levels every time step, the α_{water} values of every cell along the z-axis are stored for every wave gauge location. This α_{water} value is used to determine the amount of water in a cell and ranges from 0 (only air) to 1 (only water). These data points are then linearly interpolated to find the height where α_{water} = 0.5 to find the height of the surface elevation. These time series are then stored in new files to allow for faster analysis.

D.2. Wave heights

The calculation of wave heights is done in different ways for the Flume model and case study, since regular and irregular waves require other methods.

D.2.1. Flume

Wave heights are determined by the zero up-crossing method. very period between the surface elevation crossing the zero line (the average water level) twice, the minimum value of the surface level is subtracted from the maximum value in that period, giving the wave height. This worked well for almost all cases, except for the experimental measurements for hydrodynamic condition 4. In this case the method provided unrealistic results. As figure Figure D.1 shows, in this case, there are some small

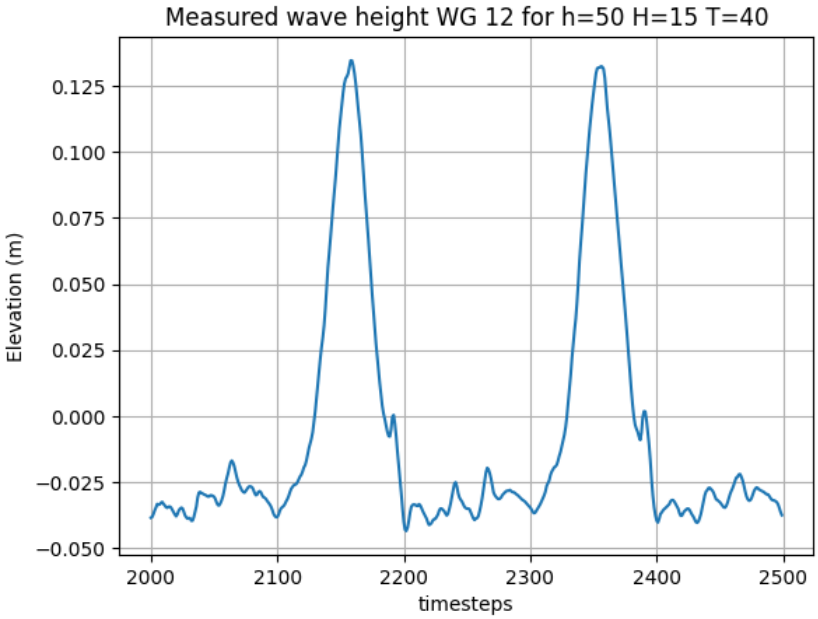

Figure D.1: Small perturbations in the measured wave height around the 0m crossing

perturbations around the zero crossing mark. This would register as an extra wave, thus skewing the

average wave height.
To circumvent this, the minimum and maximum surface elevations are determined once every wave period. The surface elevation is then found by subtracting the maximum from the minimum.

D.2.2. Case study

Different methods of computation of the wave spectrum can drastically impact the outcomes. The Deltares Wave Toolbox was employed, which offers multiple options for wave data analysis. It can be used to calculate the wave spectrum, from which the zero□order moment wave height (H_{m0}) can be derived. This spectrum can be acquired based on a self-assigned frequency step, df. Depending on the df used, wave heights can show significantly different values. Alternatively, the significant wave height can also be determined based on the 1/3 rd highest waves measured, again giving different results.

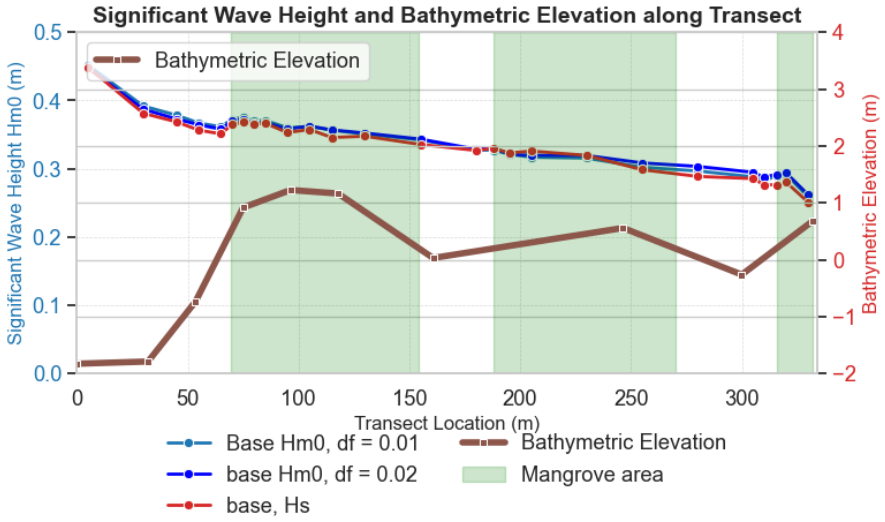

Figure D.2: Different methods of calculating wave heights from the timeseries of the model

Based on the choice of wave height representation and df, in the case of H_{m0}, results can vary slightly. This is not necessarily in the form of a constant factor over all values, but also the progression of the slope can differ slightly. For this study, H_s is chosen as the representative wave height throughout the study as it better describes the highest, most energetic waves, which are of more interest for engineering purposes.

D.3. Calculating CD and Re Values

In the study by Bryant et al. (2022), KC and Re values are determined with 2.13 and Equation (2.12). These formulas are also used in this study. However, there is a difference in the value for L that is used. In the original study, the characteristic length scale is taken as the equivalent diameter d^*, essentially the frontal areas of the roots and trunk added up as a single cylinder. This results in unrealistic KC and Re values, with KC values ranging between 1 and 6. This would mean, as previously stated in Section 2.3.4, that inertial forces are non-negligible.

Using an accurate measure for the characteristic length scale is essential in getting correct results and for comparison to other studies (Lopez-Arias et al., 2024). In the flume case, force is applied over two main length scales, the root diameter and the trunk diameter. Since roots are more prevalent their diameter is chosen as the characteristic length scale; 1.6 cm. This results in more realistic Re and KC values, which now fall outside of the range of inertial influence.

D.4. Removing spin-up

Spin-up times vary significantly for different scenarios for both the experimental as well as the model data. To prevent any spin-up time from interfering with the results, every run is personally inspected

and has spin up time manually removed based on observations of the changes in this wave height over time.

For the case study, the spin-up time is determined based on the analysis of the last wave gauge. Figure D.3 shows some small waves arriving after 70 seconds for the final wave gauge, part of the spin-up time. It shows from 150 onwards.

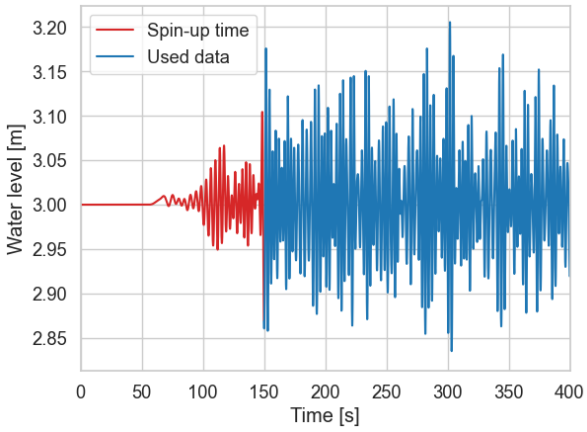

Figure D.3: Water level measurements for the last wave gauge at x = 30m for the base case without mangroves

D.5. Runtime case study

The runs of the flume model all fell well within this limit, the case study, however, did not. Runtimes were shortened from the originally intended 1200 seconds. The total analysed runtime of the model was chosen as the shortest runtime of any of the sensitivity runs (891 s). Since the wave generation uses the same wave phases for all scenarios, incoming waves are the same, allowing for fair comparison. After removing spin-up time (Appendix D.4), this leaves 741 s for analysis, resulting in only a little over 300 waves for analysis.

D.6. Beta values

Beta values are determined based on the decay of the wave height in the flume area. A best fit is found around the analytical formulation from Section 2.2.2 by minimising the root-mean-squared error.

$$H_{in} = \frac{H_{\text{out}}}{1 + \tilde{\beta} x} \tag{D.1}$$

D.7. Case study analysis

For the analysis of the wave heights in the case study, the Deltares wave toolbox is used. This allows wave gauge measurements to be transformed to a spectrum using the spectrum class. From this spectrum, further values such as the significant wave height and peak period can be obtained.

E

OpenFOAM mangrove implementation

This follows the steps of the mangrove implementation in OpenFOAM. First, in the setFIeldsDict, the stl's for the different layers are loaded and used to provide a scalar value to each layer. In this case, layer 1 has a value of 1, layer 2 a value of 2, etc. Then, in the fvOptions, the scalar values are used to create cell zones where scalars have the same value. Lastly, the defined cell zones are used and given the values for the frontal area, density and bulk drag coefficient. The following files were used for the parametrisation of mangroves for the flume case

setFieldsDict

```
/*--------------------------------*- C++ -*----------------------------------*\
| ========= | |
| \\ / F ield | OpenFOAM: The Open Source CFD Toolbox |
| \\ / O peration | Version: v2406 |
| \\ / A nd | Website: www.openfoam.com |
| \\/ M anipulation | |
\*---------------------------------------------------------------------------*/
FoamFile
{
    version 2.0;
    format ascii;
    class dictionary;
    object setFieldsDict;
}
// * * * * * * * * * * * * * * * * * * * * * * * * * * * * * * * * * * * * * //

defaultFieldValues
(
    volScalarFieldValue alpha.water 0
    volScalarFieldValue MangrovesIndex 0
    volVectorFieldValue U (0 0 0)
);

regions
(
    boxToCell
    {
        box (-10 -10 -10) (100 100 0.5);
// this waterlevel
        fieldValues
        (
            volScalarFieldValue alpha.water 1
        );
    }


    surfaceToCell
```

```
    {
        file "./constant/triSurface/Mang1.stl";
        outsidePoints ((32 1 0.15)); // definition of outside
        includeCut true; // cells cut by surface
        includeInside true; // cells not on outside of surf
        includeOutside false; // cells on outside of surf
        nearDistance -1; // cells with centre near surf
                                    // (set to -1 if not used)
        curvature -100; // cells within nearDistance
                                    // and near surf curvature
                                    // (set to -100 if not used)

        fieldValues
        (
            volScalarFieldValue MangrovesIndex 1
        );
    }

    surfaceToCell
    {
        file "./constant/triSurface/Mang2.stl";
        outsidePoints ((32 1 0.15)); // definition of outside
        includeCut true; // cells cut by surface
        includeInside true; // cells not on outside of surf
        includeOutside false; // cells on outside of surf
        nearDistance -1; // cells with centre near surf
                                    // (set to -1 if not used)
        curvature -100; // cells within nearDistance
                                    // and near surf curvature
                                    // (set to -100 if not used)

        fieldValues
        (
            volScalarFieldValue MangrovesIndex 2
        );
    }

    surfaceToCell
    {
        file "./constant/triSurface/Mang3.stl";
        outsidePoints ((32 1 0.15)); // definition of outside
        includeCut true; // cells cut by surface
        includeInside true; // cells not on outside of surf
        includeOutside false; // cells on outside of surf
        nearDistance -1; // cells with centre near surf
                                    // (set to -1 if not used)
        curvature -100; // cells within nearDistance
                                    // and near surf curvature
                                    // (set to -100 if not used)

        fieldValues
        (
            volScalarFieldValue MangrovesIndex 3
        );
    }

    surfaceToCell
    {
        file "./constant/triSurface/Mang4.stl";
        outsidePoints ((32 1 0.15)); // definition of outside
        includeCut true; // cells cut by surface
```

```
        includeInside true; // cells not on outside of surf
        includeOutside false; // cells on outside of surf
        nearDistance -1; // cells with centre near surf
                                    // (set to -1 if not used)
        curvature -100; // cells within nearDistance
                                    // and near surf curvature
                                    // (set to -100 if not used)

        fieldValues
        (
            volScalarFieldValue MangrovesIndex 4
        );
    }
);


// ************************************************************************* //
```

Listing E.1: controlDict

topoSetDict

```
/*--------------------------------*- C++ -*----------------------------------*\
| =========                 |                                                 |
| \\      / F ield          | OpenFOAM: The Open Source CFD Toolbox           |
| \\    / O peration        | Version: v2406                                  |
| \\  / A nd                | Website: www.openfoam.com                       |
| \\/ M anipulation         |                                                 |
\*---------------------------------------------------------------------------*/
FoamFile
{
    version 2.0;
    format ascii;
    class dictionary;
    object topoSetDict;
}
// * * * * * * * * * * * * * * * * * * * * * * * * * * * * * * * * * * * * * //

actions
(
    {
        name c1;
        type cellZoneSet;
        action new;
        source fieldToCell;

        field MangrovesIndex;
        min 0.5;
        max 1.5;
    }

    {
        name c2;
        type cellZoneSet;
        action new;
        source fieldToCell;

        field MangrovesIndex;
        min 1.5;
        max 2.5;
    }
```

```
    {
        name c3;
        type cellZoneSet;
        action new;
        source fieldToCell;

        field MangrovesIndex;
        min 2.5;
        max 3.5;
    }

    {
        name c4;
        type cellZoneSet;
        action new;
        source fieldToCell;

        field MangrovesIndex;
        min 3.5;
        max 4.5;
    }
);


// ************************************************************************* //
```

Listing E.2: topoSetDict

fvOptions

```
/*---------------------------------*- C++ -*----------------------------------*\
| ========= | |
| \\ / F ield | OpenFOAM: The Open Source CFD Toolbox |
| \\ / O peration | Version: v2406 |
| \\ / A nd | Website: www.openfoam.com |
| \\/ M anipulation | |
\*---------------------------------------------------------------------------*/
FoamFile
{
    version 2.0;
    format ascii;
    class dictionary;
    object fvOptions;
}
// * * * * * * * * * * * * * * * * * * * * * * * * * * * * * * * * * * * * * //

Mangroves
{
    type multiphaseMangrovesSource;
    active yes;
// changed this to no
    multiphaseMangrovesSourceCoeffs
    {
        regions
        {
            region1
            {
                cellZone c1;
                a 0.29;
                N 6;
```

```
            Cm 0;
            Cd 1.84;
        }


        region2
        {
            cellZone c2;
            a 0.261;
            N 6;
            Cm 0;
            Cd 1.84;
        }


        region3
        {
            cellZone c3;
            a 0.164;
            N 6;
            Cm 0;
            Cd 1.84;
        }


        region4
        {
            cellZone c4;
            a 0.06;
            N 6;
            Cm 0;
            Cd 1.84;
        }
    }

}
}


TurbulenciaMangroves
{
    type multiphaseMangrovesTurbulenceModel;
    active no;
// Changes to yes again
    multiphaseMangrovesTurbulenceModelCoeffs
    {
        regions
        {
            region1
            {
                cellZone c1;
                a 0.01;
                N 560;
                Ckp 1;
                Cep 3.5;
                Cd 1.52;
            }
        }
    }
}

```

```
92
93 // ************************************************************************* //
```

Listing E.3: fvOptions

F

OpenFOAM numerical schemes

fvSchemes

```
/*--------------------------------*- C++ -*----------------------------------*\
| =========                 |                                                 |
| \\      /  F ield         | OpenFOAM: The Open Source CFD Toolbox           |
| \\    /   O peration     | Version:  2.1.0                                 |
| \\  /    A nd           | Web:      www.OpenFOAM.org                      |
| \\/     M anipulation  |                                                 |
\*---------------------------------------------------------------------------*/
FoamFile
{
    version 2.0;
    format ascii;
    class dictionary;
    location "system";
    object fvSchemes;
}
// * * * * * * * * * * * * * * * * * * * * * * * * * * * * * * * * * * * * * //

ddtSchemes
{
    default Euler;
}

gradSchemes
{
    default Gauss linear;
}

divSchemes
{
    div(rhoPhi,U) Gauss linearUpwind grad(U);
    div(phi,alpha) Gauss vanLeer;
    div(phirb,alpha) Gauss linear;
    div(phi,k) Gauss upwind;
    div(phi,epsilon) Gauss upwind;
    div(phi,nuTilda) Gauss upwind;
    div(((rho*nuEff)*dev2(T(grad(U))))) Gauss linear;
}

laplacianSchemes
{
    default Gauss linear corrected;
}

interpolationSchemes
{
    default linear;
}
```

```
48
49 snGradSchemes
50 {
51     default corrected;
52 }
53
54 wallDist
55 {
56     method meshWave;
57 }
58
59
60 fluxRequired
61 {
62     default no;
63     p_rgh;
64     pcorr;
65     alpha;
66 }
67
68
69 // ************************************************************************* //
```

Listing F.1: fvSchemes

fvSolution

```
1  /*--------------------------------*- C++ -*----------------------------------*\
2  | =========                 |                                                 |
3  | \\      /  F ield         | OpenFOAM: The Open Source CFD Toolbox           |
4  | \\    /   O peration     | Version:  2.1.0                                 |
5  | \\  /    A nd           | Web:      www.OpenFOAM.org                      |
6  | \\/     M anipulation  |                                                 |
7  \*---------------------------------------------------------------------------*/
8  FoamFile
9  {
10     version 2.0;
11     format ascii;
12     class dictionary;
13     location "system";
14     object fvSolution;
15 }
16 // * * * * * * * * * * * * * * * * * * * * * * * * * * * * * * * * * * * * * * * * //
17
18 solvers
19 {
20
21     "alpha.water.*"
22     {
23         nAlphaCorr 1;
24         nAlphaSubCycles 2;
25         alphaOuterCorrectors yes;
26         cAlpha 1;
27
28         MULESCorr no;
29         nLimiterIter 3;
30
31         solver smoothSolver;
32         smoother symGaussSeidel;
33         tolerance 1e-8;
34         relTol 0;
```

```
    }

    pcorr
    {
        solver PCG;
        preconditioner DIC;
        tolerance 1e-6;
        relTol 0;
    }

    pcorrFinal
    {
        solver PCG;
        preconditioner DIC;
        tolerance 1e-6;
        relTol 0;
    }

    p_rgh
    {
        solver PCG;
        preconditioner DIC;
        tolerance 1e-6;
        relTol 0;
    }

    p_rghFinal
    {
        solver PCG;
        preconditioner DIC;
        tolerance 1e-6;
        relTol 0;
    }

    "(U|k|epsilon|omega)"
    {
        solver PBiCG;
        preconditioner DILU;
        tolerance 1e-3;
        relTol 0;
    }

    "(U|k|epsilon|omega)Final"
    {
        solver PBiCG;
        preconditioner DILU;
        tolerance 1e-3;
        relTol 0;
    }
    R
    {
        solver PBiCG;
        preconditioner DILU;
        tolerance 1e-03;
        relTol 0;
    }

    nuTilda
    {
        solver PBiCG;
        preconditioner DILU;
```

```
        tolerance 1e-03;
        relTol 0;
    }
}

PIMPLE
{
    momentumPredictor no;
    nCorrectors 3;
    nNonOrthogonalCcorrectors 0;
    nAlphaCorr 1;
    nAlphaSubCycles 4;
    cAlpha 2;
}


// ************************************************************************* //
```

Listing F.2: fvSolution

G

Wave profile comparissons

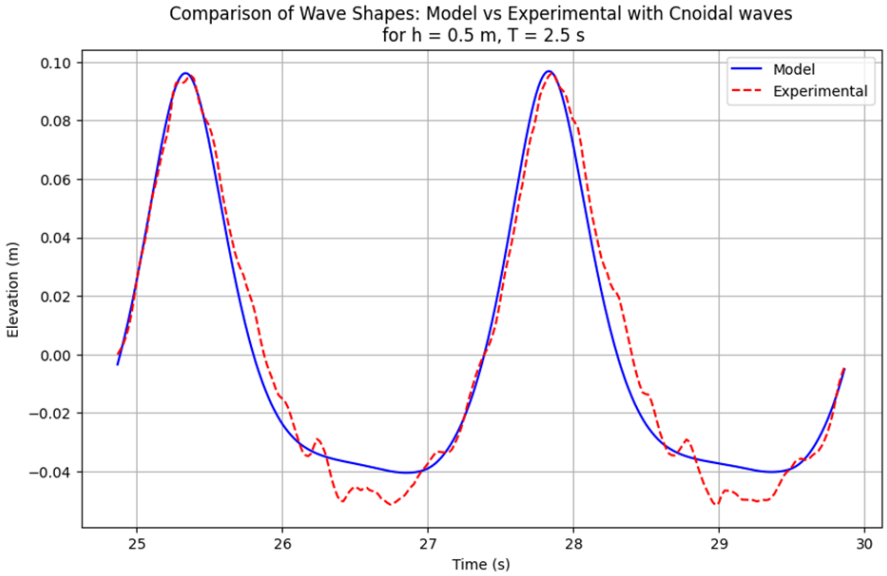

Figure G.1: Comparison of the wave profile for 2 wavelengths between the model measurements and model outcomes for HC2

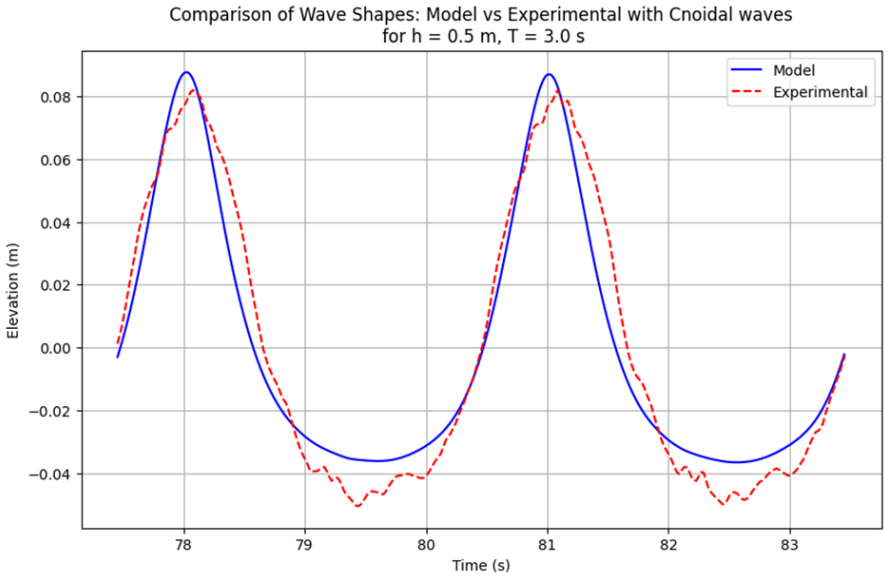

Figure G.2: Comparison of the wave profile for 2 wavelengths between the model measurements and model outcomes for HC3

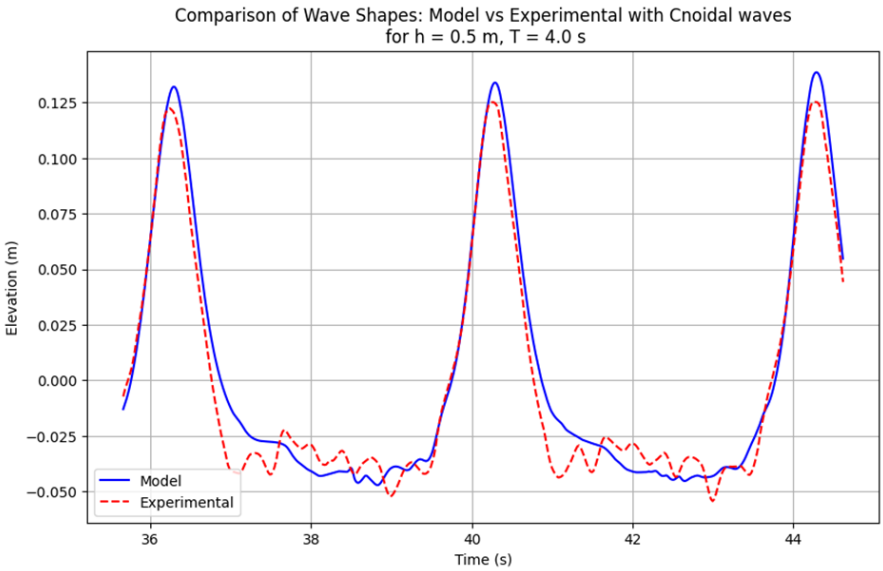

Figure G.3: Comparison of the wave profile for 2 wavelengths between the model measurements and model outcomes for HC4

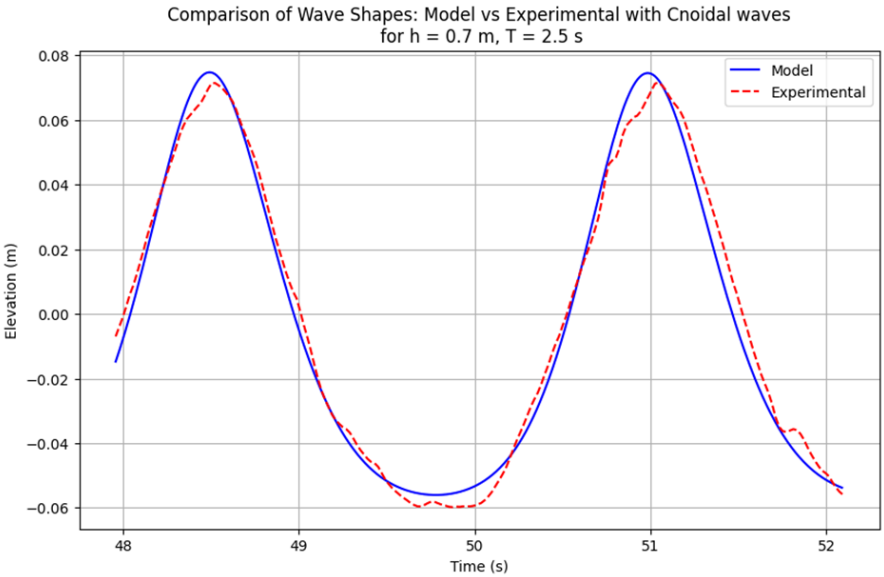

Figure G.4: Comparison of the wave profile for 2 wavelengths between the model measurements and model outcomes for HC5

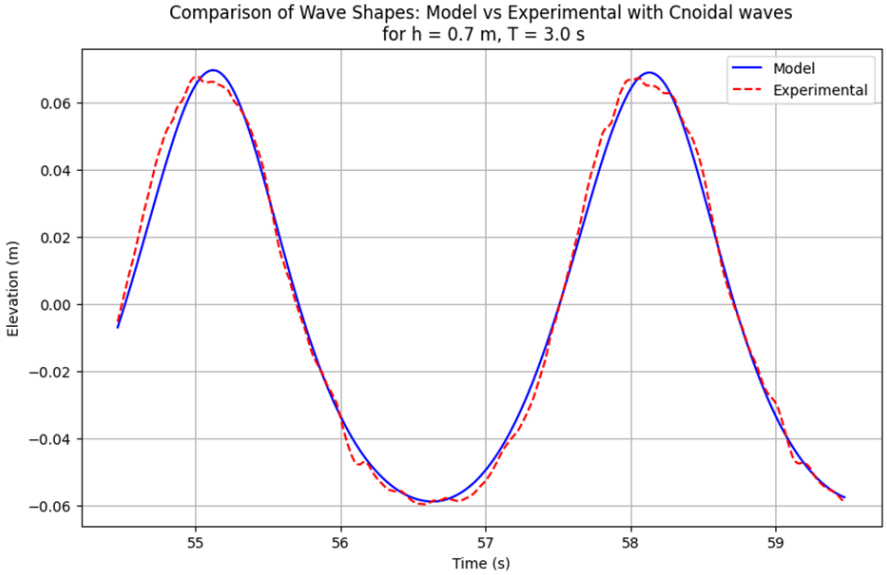

Figure G.5: Comparison of the wave profile for 2 wavelengths between the model measurements and model outcomes for HC6

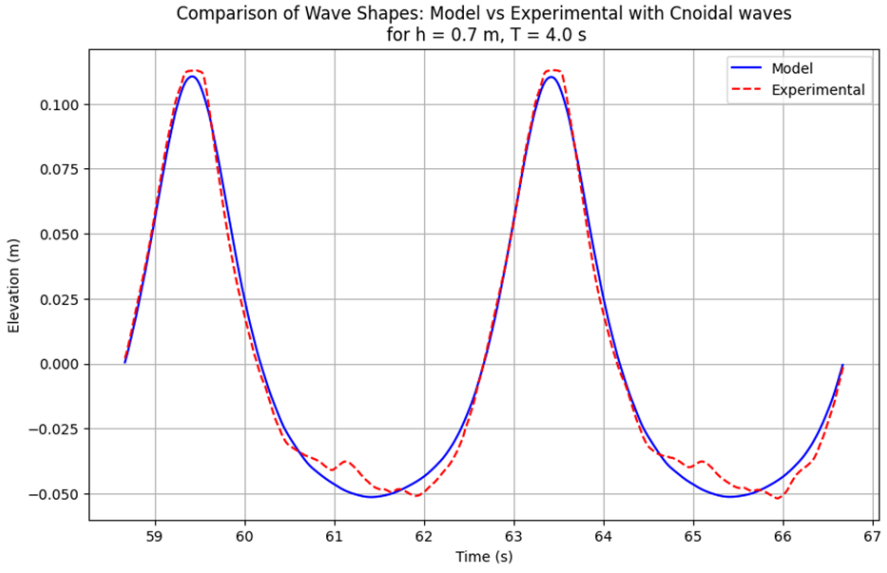

Figure G.6: Comparison of the wave profile for 2 wavelengths between the model measurements and model outcomes for HC7

H

Flume validation

This appendix shows the Wave height evolution for the full flume, comparing the experimental measurements with the model outcomes for all Hydrodynamic conditions.

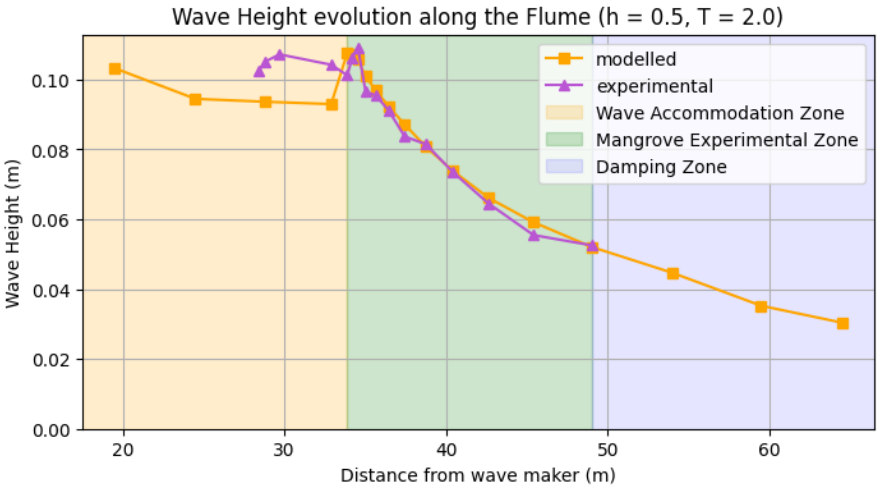

Figure H.1: Wave height evolution for the full flume, comparing the experimental measurements with the model outcomes for HC1

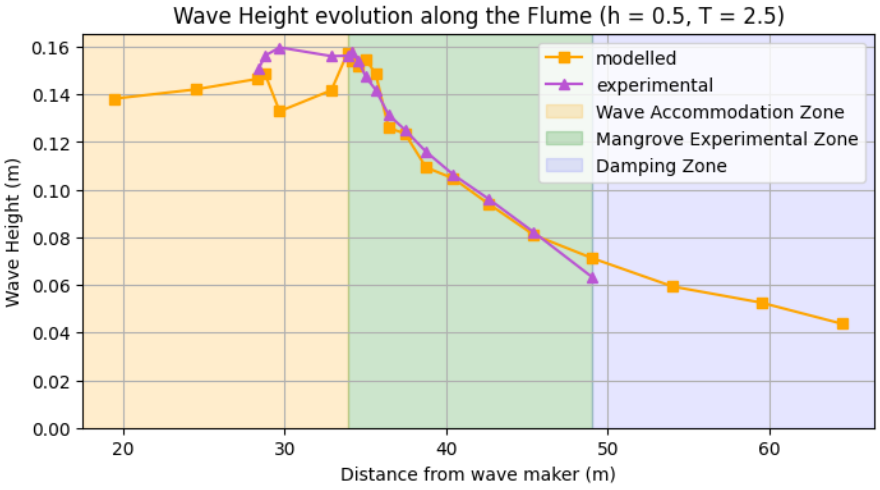

Figure H.2: Wave height evolution for the full flume, comparing the experimental measurements with the model outcomes for HC2

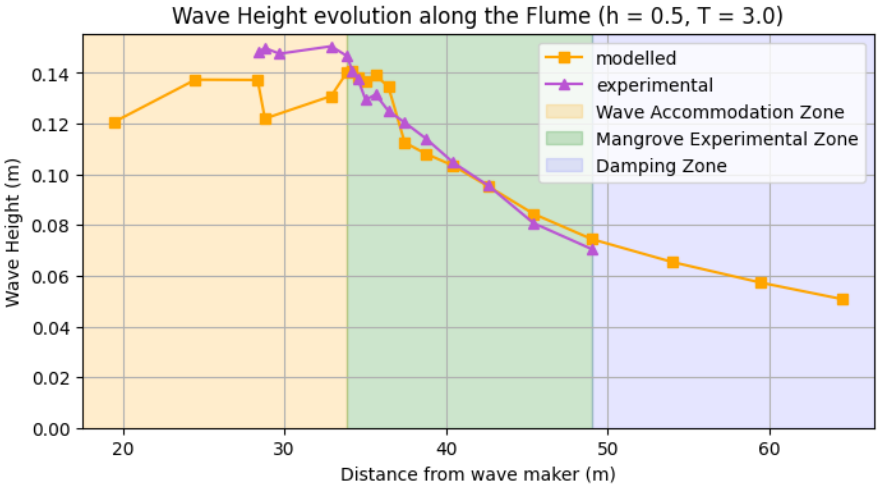

Figure H.3: Wave height evolution for the full flume, comparing the experimental measurements with the model outcomes for HC3

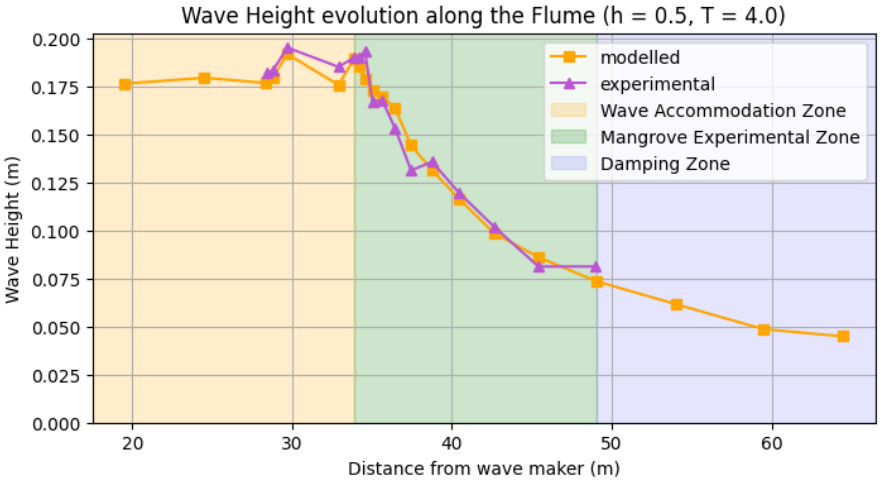

Figure H.4: Wave height evolution for the full flume, comparing the experimental measurements with the model outcomes for HC4

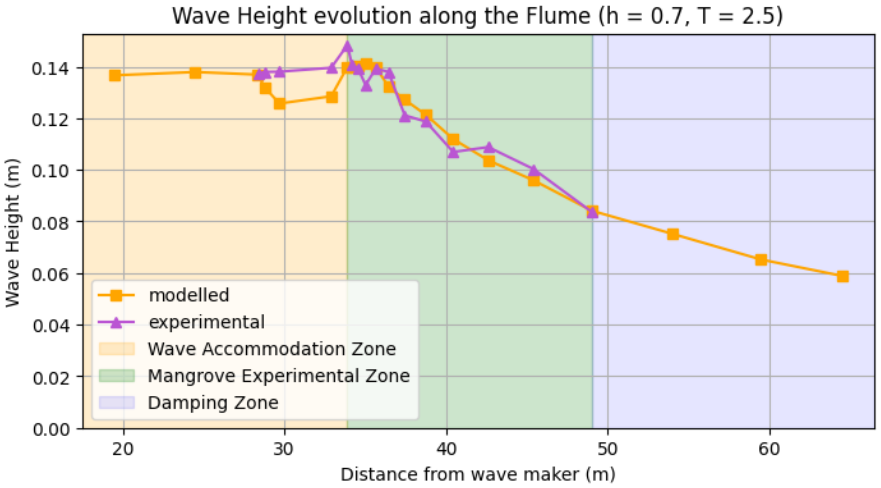

Figure H.5: Wave height evolution for the full flume, comparing the experimental measurements with the model outcomes for HC5

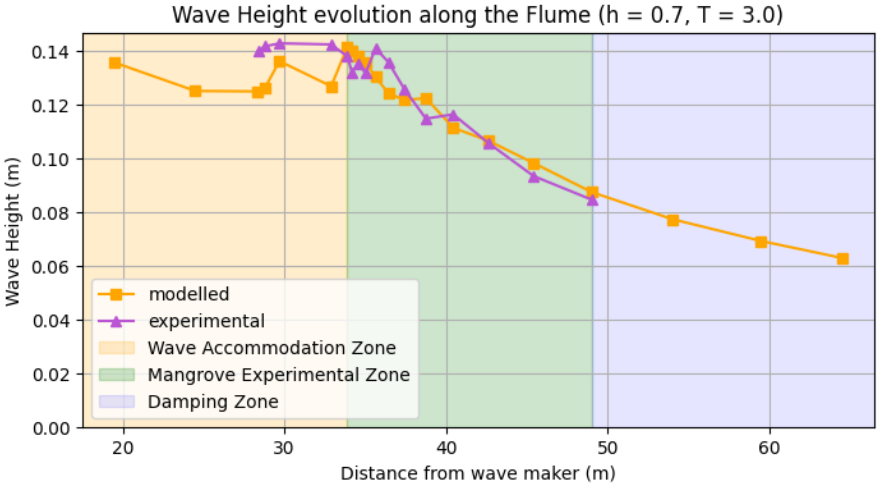

Figure H.6: Wave height evolution for the full flume, comparing the experimental measurements with the model outcomes for HC6

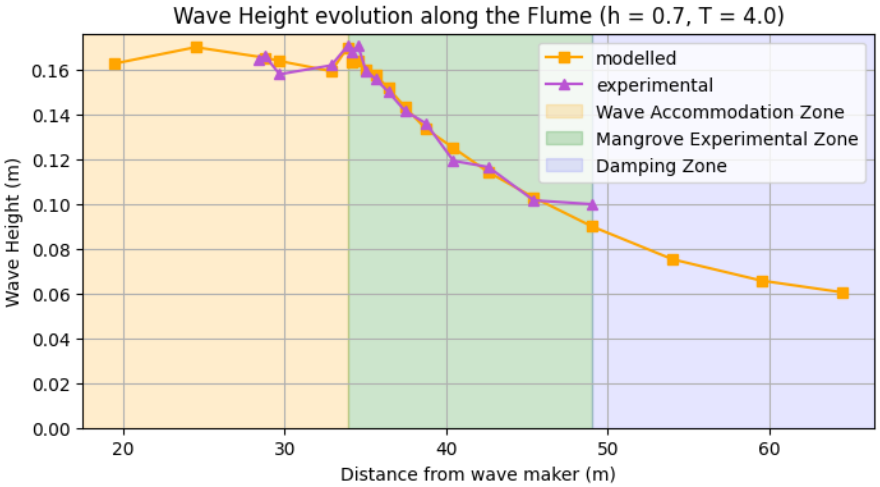

Figure H.7: Wave height evolution for the full flume, comparing the experimental measurements with the model outcomes for HC7

I

Sensitivity analysis

This appendix features all plots used for the sensitivity analysis of the case study model

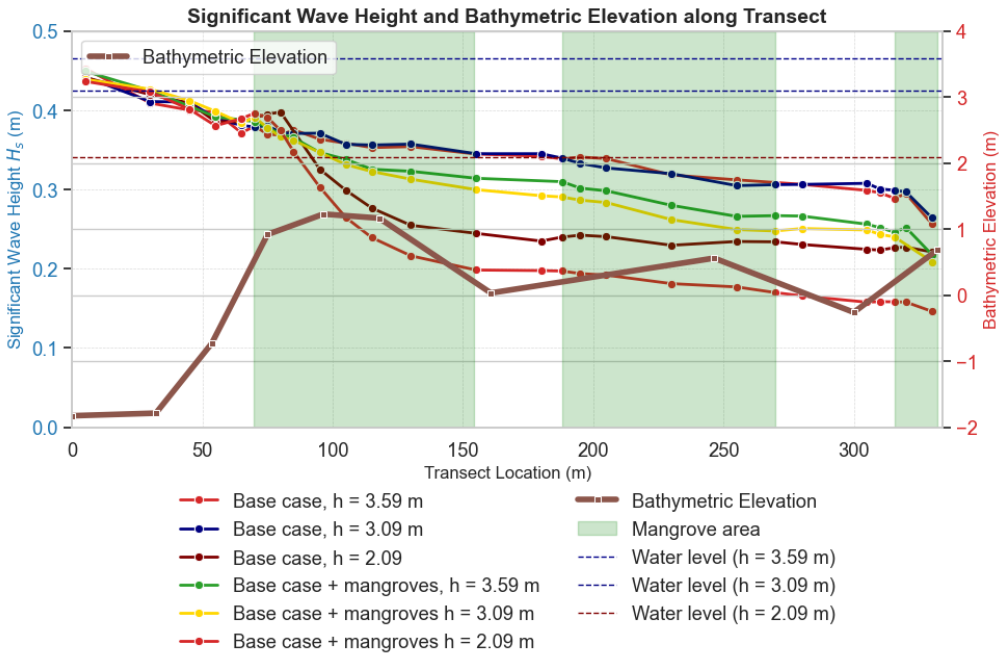

Figure I.1: Significant wave height evolution along the transect with two reduced water levels (h = 3.09 m and h = 2.09), compared with the regular water level (h = 3.59 m). All scenarios are shown with and without mangroves.

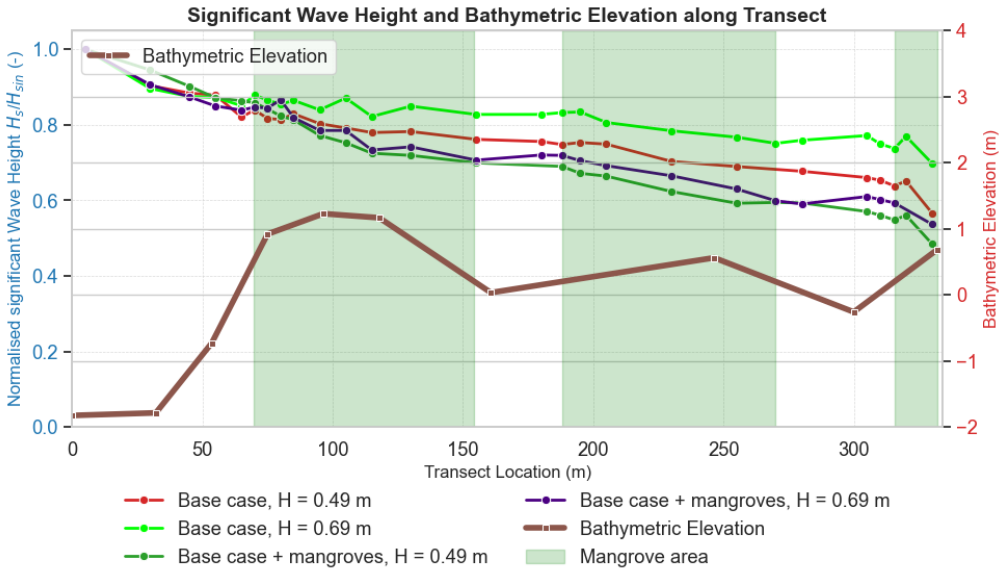

Figure I.2: Significant wave height evolution along the transect with increased wave height (H_s = 0.69 m, T_p = 3.1 s). Shown for both with and without mangroves

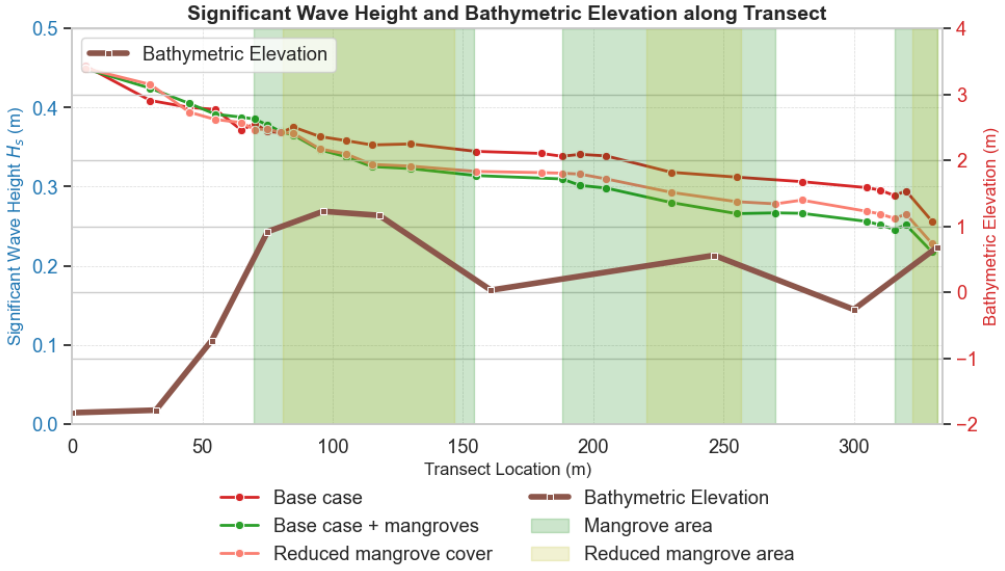

Figure I.3: Significant wave height evolution along the transect showing the difference between the selected mangrove cover (183 m) and a reduced mangrove cover (112 m)

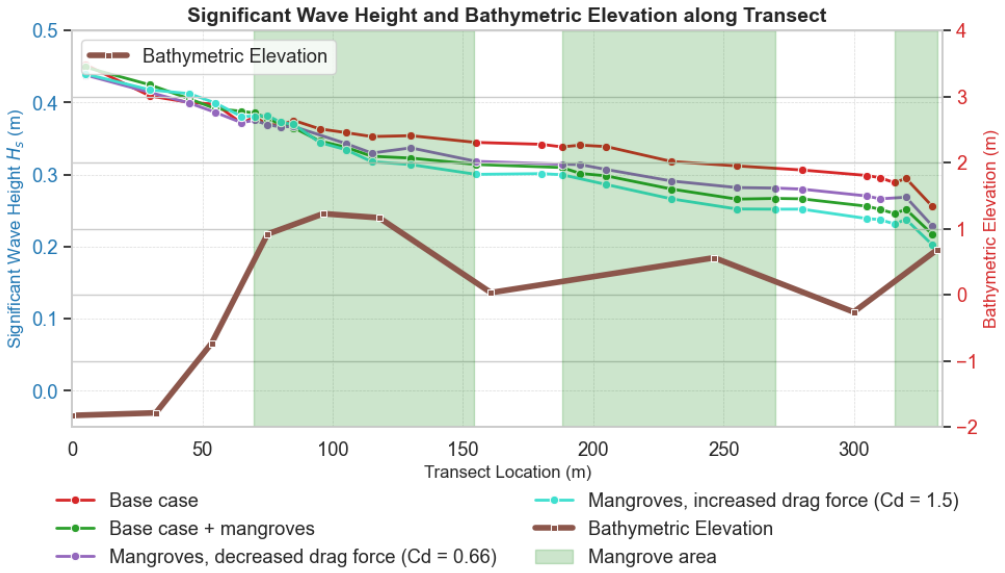

Figure I.4: Wave height evolution along the transect showing the difference in attenuation between varying drag forces. Each run has an increase of 50% in total drag force ($\tilde{C}_d$ = 0.66, 1, 1.5)

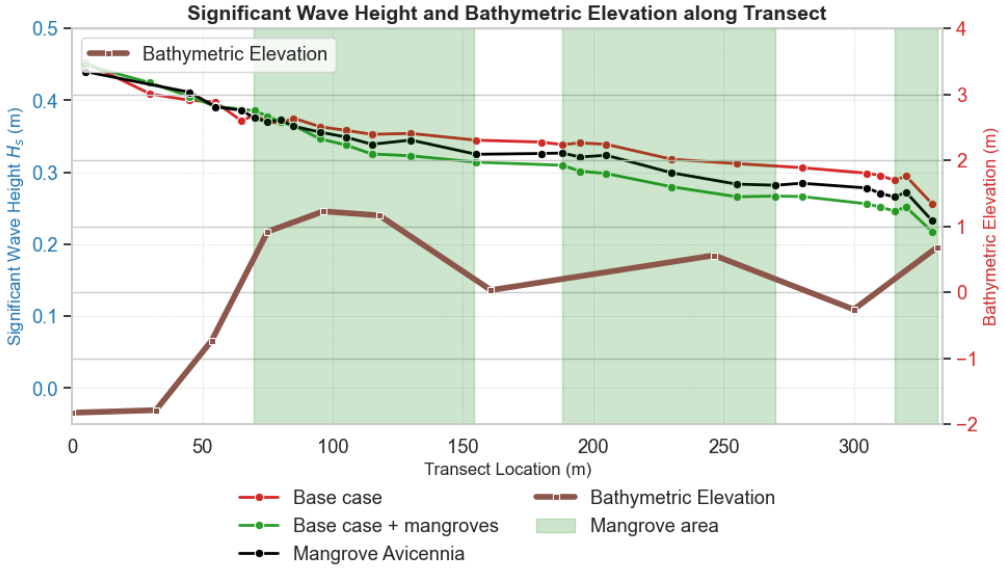

Figure I.5: Wave height evolution along the transect showing the difference in attenuation between the selected mangrove parametrisation (based on the frontal area of Rhizophora species) and that of Avicennia species

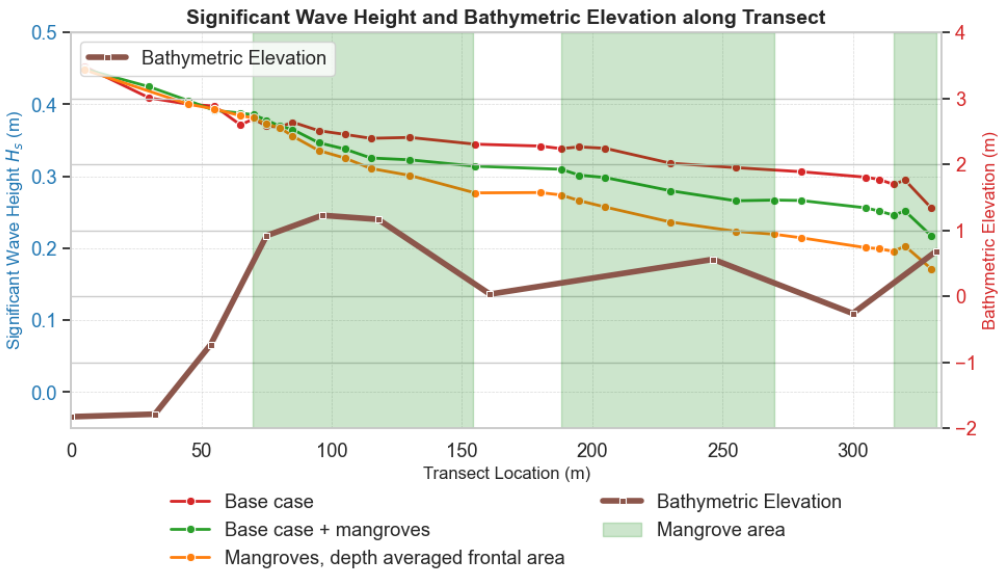

Figure I.6: Wave height evolution along the first mangrove zone, showing the difference between the depth-averaged approach and the layered approach

J

Analytical damping in python

```
1
2  def analytical_attenuation(gauges, cut, water_level, Tp):
3
4
5      dt = 0.01
6      time_new, wl_new = interpolate_gauge_data(gauges, start_time=150, dt=dt)
7
8      hs_list = []
9      Tps_list = []
10     time = cut *100
11     time_cut = time_new[:time]
12     wl_cut = wl_new[:, :time]
13     for ii in range(wl_new.shape[0]): #determine Hs and Tp for every wave gauge
14         z = wl_cut[ii] - gauges['val'][ii, 0] # Assuming the first value is the reference
               height
15         timeseries = dwt.series.Series(time_cut, z)
16         spec2 = timeseries.get_spectrum_raw(dfDesired = 0.01)
17         try:
18             hs = timeseries.get_Hs()[0]
19             Tps = spec2.get_Tps()
20             print(Tps)
21         except ValueError:
22             hs = 0
23             Tps = 0
24         hs_list.append(hs)
25         if Tps > 5:
26             Tps = Tp
27         Tps_list.append(Tps)
28
29     Cd = 1
30     bath_lvl = np.array([0.6, 0.9, 1, 1.08, 1.21, 1.2, 1.18, 0.84, 0.2]) #depths at each wave
           gauge
31     end_x = np.array([70, 75, 80, 85, 95, 105, 115, 130, 155]) #x-values of each wave geuge
32
33     H_rms_old = 0.707*np.array([hs_list[5:14]]) #Convert Hs to Hrms for calculation
34     H_rms = H_rms_old[0] #first wave height
35
36     Tp = Tps_list[5:14]
37     wh_equation = [] #waveheights
38     a = 1
39     wh_equation.append(H_rms[0])
40     for i in range(len(bath_lvl)-1):
41         av_bath = (bath_lvl[i] + bath_lvl[i+1]) / 2 #Average bathymetry height
42         Tp_av = (Tp[i] + Tp[i+1]) / 2 #Average Tp
43         k = 2 * np.pi / (9.81 * Tp_av**2 / (2 * np.pi))**0.5 # Wave number
44         h = water_level - av_bath
45         bv = (0.464*0.1 + 0.21*0.4 + 0.12* 1 + 0.03*0.5 +0.017 * (water_level - 2 - av_bath))/h
46         sinh_kh = np.sinh(k * h)
47         sinh_2kh = np.sinh(2 * k * h)
```

```
        sinh_kah = np.sinh(k * h)
        numerator = sinh_kah**3 + 3 * sinh_kah
        denominator = sinh_2kh + 2 * k * h
        beta = (1 / (3 * np.sqrt(np.pi))) * Cd * bv * wh_equation[i] * a * k * (numerator / (
            denominator * sinh_kh))

        dx = end_x[i+1] - end_x[i]
        wh_decrease = wh_equation[i] / (1 + beta * dx) - wh_equation[i]
        wh_equation.append(wh_equation[i] + wh_decrease - (H_rms[i] - H_rms[i+1]))
    flat_array = np.concatenate([np.atleast_1d(item) for item in wh_equation])


    return flat_array/0.707 # Convert from Hs to Hm0 (Hmo = Hs / 0.707)
```

Listing 1: Comparison of Layered vs Depth-Averaged Frontal Area